SYNTHESIS OF LOW-CHARGED SMECTITES

Zur Erlangung des akademischen Grades einer

DOKTORIN DER NATURWISSENSCHAFTEN

(Dr. rer. nat.)

von der KIT-Fakultät für

Bauingenieur-, Geo- und Umweltwissenschaften

des Karlsruher Instituts für Technologie (KIT)

genehmigte

DISSERTATION

von

M.Sc. Yi-Yu Liu

aus Taiwan

Tag der mündlichen Prüfung: 28.10.2024

Referentin: Prof. Dr. Katja Emmerich

Korreferent: PD Dr. Peter Thissen

Karlsruhe 2024

Abstract

Clay materials, including smectite group minerals like montmorillonite and saponite, exhibit specific mineralogical, chemical, and physical properties, making them in various industrial applications. These minerals possess nanometric layer structures, high specific surface areas, layer charges, and cation exchange capacities, contributing to their versatility. Utilized across industries such as ceramics, food, chemicals, and medicine, clay minerals play crucial roles owing to their unique properties. Recent advancements have also highlighted the potential of nanoscale clay materials in biomedical applications and emerging technologies, particularly in the field of 2D layered materials and their applications in high-performance quantum light devices.

The smectite group belongs to the 2:1 layer silicates, which classified according to the layer charge (ξ = x/n = y+z) per formula unit (p.f.u.) $M^{+}_{x/n}$ $(Si_{4-y}\ Al_{y})$ $[(Al, Fe^{3+})_{2-z}\ (Mg, Fe^{2+})_{z}]$ $O_{10}\ (OH)_{2}$ (Guggenheim et al., 2006). However, a definition gap exists between the uncharged, non-swellable pyrophyllite $\xi = 0$ and the charged group of swellable smectites with $0.2 \leq \xi \leq 0.6$. Moreover, there is no experimental evidence to support the existence of low charge smectites with a layer charge in the range $0 < \xi < 0.2$. Therefore, obtaining low charge dioctahedral and trioctahedral smectites with $\xi < 0.2$ is crucial for exploring their properties and nature. This research aims to combine the synthesis of low charge smectites with ξ = 0.1, 0.125, 0.18 and the simulation of low charge montmorillonite models using density functional theory (DFT) calculations. Through the results of synthesis and theoretical calculations of their swellability and hydration behavior, this study aims to provide a foundation for investigating the potential applications of low charge smectites in various fields.

The synthesis research focus on the low charge trioctahedral and dioctahedral smectites with layer charges setting ξ = 0.18, 0.125, 0.1. The successful synthesis of single-phase trioctahedral smectite with interlayer Mg^{2+} was achieved, while the scanning electron microscope (SEM) images showed a lamellar structure similar to natural saponite and Laponite® RD. The measured cation exchange capacity values exceeded calculated values, indicating contributions from higher edge charge densities, as supported by the analysis of specific edge area. The structural formula calculated from chemical composition analysis revealed a possible range of low charge ξ = 0.17 - 0.21. Several indirect evidences, such as alkylammonium ions with longer chain lengths only forming a monolayer structure in all synthetic samples, confirm that the synthetic samples have a layer charge lower than the measurable limit of the alkylammonium method, supporting the possibility that the synthetic trioctahedral smectite possesses a low layer charge. However, synthesizing low charge montmorillonite proved challenging, yielding samples with impurities such as kaolinite, boehmite, and sellaite. Extending the synthesis duration improved the crystallinity of montmorillonite but did not eliminate impurities and amorphous phase. The SEM images showed a distinctive flake structure similar to the morphology of montmorillonite, with dust-like small particle aggregates, which qualitative energy dispersive spectroscopy (EDS) analyses suggest are unreacted SiO_2 or amorphous phases. Results from ^{27}Al & ^{19}F magic angle spinning solid state nuclear magnetic resonance (MAS NMR) spectroscopy

showed that Al^{3+} locates in both the tetrahedral and octahedral sheet of synthetic montmorillonite, and indicated the substitution of F for hydroxyl groups in the tetrahedral sheet, and also suggesting that the amount of sellaite can be decreased by increasing the synthesis duration. Based on the quantitative phase analysis, when the synthesis duration is extended, the mineral phases of the synthetic samples begin to change from containing multiple impurities to having only montmorillonite and kaolinite, with the percentage of synthetic montmorillonite around 56 - 62%. The analysis of synthetic montmorillonite reveals several challenges in accurately determining or predicting its actual chemical composition, structural formula and layer charge range due to impurities, the presence of an amorphous phase, and variability in chemical composition analysis. Future synthesis efforts for low charge montmorillonite should focus on optimizing experimental parameters using the design of experiments to enhance the percentage and crystallinity of the montmorillonite phase while reducing the amorphous phase. Adjusting synthesis parameters such as temperature, duration, pressure, and hydrogel concentration, as well as exploring different synthesis equipment, could improve synthesis outcomes. Additionally, controlling the fill rate and pressure inside the synthesis container, incorporating different mineralizers with F, and optimizing the order of starting material addition are critical factors for successful synthesis. By systematically optimizing these variables, it is possible to achieve higher quality, low charge montmorillonite with fewer impurities and amorphous phase.

The hydration behavior and swellability of low charge montmorillonite models ($\xi = 0.125$) with trans-vacant and two cis-vacant structure were explored through DFT calculations employing the DFT-D3 method. The basal spacing of the water-free trans-vacant and cis-vacant montmorillonite models closely matched experimental values. During hydration, as the number of H_2O/Na^+ increased, the basal spacing expanded to approximately 12 Å for all three hydrated montmorillonite models. The interaction between Na^+ ions and the tetrahedral sheet O atoms played a significant role in the hydration process. Additionally, the weakening of the interaction between Na^+ ions and the surface was observed through the calculation of enthalpy change between the bonding of Na^+ ion and the nearest oxygen atom on the surface of the tetrahedral sheets was compared, providing further insights into the hydration mechanism. Furthermore, the discussion emphasized the tendency of standard DFT methods, such as PBE and PW91 functionals, to overestimate basal spacing in various research studies due to the absence of explicit treatment of dispersion forces. This overestimation seems to be improved by employing the DFT-D3 method, which lower the basal spacing prediction observed in the simulations. Analysis of p, T-phase diagrams indicated that the hydration state of montmorillonite models remained at 0H to 1H for all models with 1 to 9 H_2O/Na^+ up to an rH of 100%. Last but not least, trans-vacant montmorillonite model with 21 H_2O/Na^+ reached the 1H hydration state at 273 - 293 K and rH of 50 - 100%, suggesting the potential for swelling behavior under ambient conditions. In optimizing future simulations of low charge montmorillonite model, considering additional experimental parameters is crucial for enhancing the accuracy of calculation. This includes increasing the number of H_2O/Na^+ by the equivalent area ($a_0 \cdot b_0$) of the low charge montmorillonite model, optimizing the initial configuration of water molecules in the interlayer, and analyzing the forces and interactions at the interface of Na-saturated montmorillonite and water molecules. Molecular Dynamics (MD) calculations, when compared with DFT calculations of smectite hydration, provide complementary insights into the system's behavior.

Kurzfassung

Tonmaterialien, einschließlich Minerale der Smektitgruppe wie Montmorillonit und Saponit, weisen spezifische mineralogische, chemische und physikalische Eigenschaften auf, die sie in verschiedenen industriellen Anwendungen bedeutend machen. Diese Minerale besitzen nanometrische Schichtstrukturen, hohe spezifische Oberflächen, Schichtladungen und Kationenaustauschkapazitäten, was zu ihrer Vielseitigkeit beiträgt. Sie werden in Industrien wie der Keramik-, Lebensmittel-, Chemie- und Medizinindustrie genutzt und spielen aufgrund ihrer einzigartigen Eigenschaften eine wichtige Rolle. Jüngste Fortschritte haben auch das Potenzial nanoskaliger Tonmaterialien in biomedizinischen Anwendungen und aufstrebenden Technologien hervorgehoben, insbesondere im Bereich der 2D-Schichtmaterialien und deren Anwendungen in Hochleistungs-Quantenlichtgeräten.

Die Smektitgruppe gehört zu den 2:1-Schichtsilikaten, die nach der Schichtladung (ξ = x/n = y+z) pro Formeleinheit (p.f.u.) $M^{+}_{x/n}(Si_{4-y}Al_{y})[(Al,Fe^{3+})_{2-z}(Mg,Fe^{2+})_{z}]O_{10}(OH)_{2}$ (Guggenheim et al., 2006) klassifiziert werden. Es besteht jedoch eine Definitionslücke zwischen dem ungeladenen, nicht quellfähigen Pyrophyllit ($\xi = 0$) und der geladenen Gruppe der quellfähigen Smektite mit $0.2 \leq \xi \leq 0.6$. Darüber hinaus gibt es keine experimentellen Beweise für die Existenz von Smektiten mit niedriger Ladung im Bereich von $0 < \xi < 0.2$. Daher ist die Gewinnung von dioctaedrischen und trioctaedrischen Smektiten mit $\xi < 0.2$ entscheidend, um ihre Eigenschaften und Natur zu erforschen. Diese Forschung zielt darauf ab, die Synthese von Smektiten mit niedriger Ladung bei ξ = 0.1, 0.125, 0.18 mit der Simulation von Montmorillonit-Modellen mit niedriger Ladung mittels Density Functional Theory (DFT)-Berechnungen zu kombinieren. Durch die Ergebnisse der Synthese und theoretischen Berechnungen ihrer Quellfähigkeit und Hydratationsverhalten soll diese Studie eine Grundlage für die Untersuchung der potenziellen Anwendungen von Smektiten mit niedriger Ladung in verschiedenen Bereichen bieten.

Die Syntheseforschung konzentriert sich auf niedrig geladene trioctaedrische und dioctaedrische Smektite mit Schichtladungen von ξ = 0,18, 0,125 und 0,1. Die erfolgreiche Synthese von einphasigem trioctaedrischem Smektit mit interstitiellen Mg2+-Ionen wurde erreicht, während SEM-Bilder eine lamellare Struktur ähnlich wie bei natürlichem Saponit und Laponite® RD zeigten. Die gemessenen Kationenaustauschkapazitätswerte (CEC) übertrafen die berechneten Werte, was auf Beiträge von höheren Randladungsdichten hinweist, die durch die Analyse der spezifischen Randfläche unterstützt wurden. Die aus der chemischen Zusammensetzungsanalyse berechnete Strukturformel zeigte einen möglichen Bereich niedriger Ladung von ξ = 0.17 - 0.21. Mehrere indirekte Hinweise, wie die Bildung einer Monoschichtstruktur durch Alkylammoniumionen mit längeren Kettenlängen in allen synthetischen Proben, bestätigen, dass die synthetischen Proben eine Schichtladung unterhalb der messbaren Grenze der Alkylammoniummethode aufweisen, was die Möglichkeit unterstützt, dass der synthetische trioctaedrische Smektit eine niedrige Schichtladung besitzt. Die Synthese von montmorillonit mit niedriger Ladung erwies sich jedoch als herausfordernd und ergab Proben mit Verunreinigungen wie Kaolinit, Böhmit und Sellaite. Eine Verlängerung der Synthesedauer verbesserte die Kristallinität von Montmorillonit, beseitigte jedoch nicht die

Verunreinigungen und amorphen Phasen. Die SEM-Bilder zeigten eine charakteristische Flockenstruktur, die der Morphologie von Montmorillonit ähnlich ist, mit staubartigen kleinen Partikelaggregaten, die in qualitativen EDS-Analysen als nicht umgesetztes SiO_2 oder amorphe Phasen identifiziert wurden. Ergebnisse der ^{27}Al und ^{19}F MAS-NMR-Spektroskopie zeigten, dass Al^{3+} sowohl in den tetraedrischen als auch in den oktaedrischen Schichten des synthetischen Montmorillonits lokalisiert ist, und deuteten außerdem auf den Austausch von F gegen Hydroxylgruppen in den tetraedrischen Schichten hin, wobei die Menge an Sellaite durch Verlängerung der Synthesedauer verringert werden kann. Basierend auf der quantitativen Phasenanalyse beginnen sich bei verlängerter Synthesedauer die Mineralphasen der synthetischen Proben von mehrfachen Verunreinigungen zu reinem Montmorillonit und Kaolinit zu verändern, wobei der Anteil an synthetischem Montmorillonit bei etwa 56 - 62% liegt. Die Analyse des synthetischen Montmorillonits zeigt mehrere Herausforderungen bei der genauen Bestimmung oder Vorhersage seiner tatsächlichen chemischen Zusammensetzung, Strukturformel und Schichtladungsbereich aufgrund von Verunreinigungen, dem Vorhandensein amorpher Phasen und Variabilität in der chemischen Zusammensetzungsanalyse. Künftige Syntheseversuche für Montmorillonit mit niedriger Ladung sollten sich darauf konzentrieren, experimentelle Parameter mithilfe der Versuchsplanung zu optimieren, um den Anteil und die Kristallinität der Montmorillonit-Phase zu erhöhen und gleichzeitig die amorphen Phasen zu reduzieren. Die Anpassung von Syntheseparametern wie Temperatur, Dauer, Druck und Hydrogelkonzentration sowie die Untersuchung unterschiedlicher Syntheseausrüstungen könnten die Syntheseergebnisse verbessern. Darüber hinaus sind die Steuerung der Füllrate und des Drucks im Synthesebehälter, die Einbeziehung verschiedener Fluoridionen und die Optimierung der Reihenfolge der Zugabe von Ausgangsmaterialien entscheidende Faktoren für eine erfolgreiche Synthese. Durch die systematische Optimierung dieser Variablen ist es möglich, Montmorillonit mit niedriger Ladung und weniger Verunreinigungen sowie amorphen Phasen in höherer Qualität zu erreichen.

Das Hydratationsverhalten und die Quellfähigkeit von Montmorillonit-Modellen mit niedriger Ladung ($\xi = 0.125$) und trans- sowie zwei cis-vakanten Strukturen wurden mittels DFT-Berechnungen unter Verwendung der DFT-D3-Methode untersucht. Der Basalabstand der wasserfreien trans-vakanten und cis-vakanten Montmorillonit-Modelle stimmte eng mit experimentellen Werten überein. Während der Hydratation, mit zunehmender Anzahl von H2O/Na+, erweiterte sich der Basalabstand auf etwa 12 Å für alle drei hydratisierten Montmorillonit-Modelle. Die Wechselwirkung zwischen Na^+ Ionen und den Sauerstoffatomen der tetraedrischen Schicht spielte eine bedeutende Rolle im Hydratationsprozess. Zudem wurde die Schwächung der Wechselwirkung zwischen Na+-Ionen und der Oberfläche durch die Berechnung der Enthalpieänderung zwischen der Bindung des Na+-Ions und dem nächsten Sauerstoffatom an der Oberfläche der tetraedrischen Schichten verglichen, was weitere Einblicke in den Hydratationsmechanismus lieferte. Darüber hinaus wurde in der Diskussion die Tendenz der Standard-DFT-Methoden, wie PBE- und PW91-Funktionale, betont, den Basalabstand in verschiedenen Forschungsstudien aufgrund des Fehlens einer expliziten Behandlung der Dispersionskräfte zu überschätzen. Diese Überschätzung scheint durch die Verwendung der DFT-D3-Methode verbessert zu werden, was die in den Simulationen beobachtete niedrigere Basalabstandsvorhersage erklärt. Die Analyse von p ,T-Phasendiagrammen zeigte, dass der Hydratationszustand der Montmorillonit-Modelle bei 0H bis 1H für alle Modelle mit 1 bis 9 H_2O/Na^+ bis zu einer relativen Luftfeuchtigkeit (rH) von 100% blieb. Schließlich erreichte das trans-vakante Montmorillonit-Modell mit 21 H_2O/Na^+ den 1H-Hydratationszustand bei 273 - 293 K und rH von 50 - 100%, was auf ein Quellverhalten unter Umgebungsbedingungen hinweist. Bei der Optimierung zukünftiger Simulationen des Hydratationszustands von Montmorillonit-Modellen mit niedriger Ladung ist es entscheidend, zusätzliche experimentelle Parameter zu berücksichtigen, um die Genauigkeit der Berechnungen zu verbessern. Dies umfasst die Erhöhung der Anzahl von H_2O/Na^+ in Abhängigkeit vom äquivalenten Bereich (a_0b_0) des Montmorillonit-Modells mit niedriger Ladung, die Optimierung der Anfangskonfiguration der Wassermoleküle im Zwischenschichtbereich und die Analyse der Kräfte und Wechselwirkungen an der Schnittstelle zwischen Na-gesättigtem Montmorillonit und Wassermolekülen. Molekulardynamik (MD)-Berechnungen liefern im Vergleich zu DFT-Berechnungen der Smektit-Hydratation ergänzende Einblicke in das Verhalten des Systems.

Table of Contents

List of Abbreviations

DFT	Density Function Theory
MD	Molecular Dynamics
MC	Monte Carlo
rH	Relative Humidity

1 Introduction

1.1 Introduction

Clay minerals are naturally occurring materials that exhibit diverse mineralogical, chemical, and physical properties. Among the various clay materials, smectite group minerals, such as montmorillonite and saponite, are of particular significance due to their unique properties. These minerals possess a nanometric layer structure, high specific surface area, layer charge, and cation exchange capacity. Owing to their remarkable properties, clay minerals are extensively used in their natural form across numerous industrial applications, including the ceramic, food, chemical, and medical industries. (Eisenhour & Brown, 2009; Jasmund & Lagaly, 2013). Nanoscale clay materials have garnered not only consistent interest across diverse biomedical applications, but also while recent advancements in technology have sparked discussions about the latest progressions in 2D layered materials, specifically in their contributions to high-performance quantum light devices and emitters. The extensive utilization of clay minerals underscores their significance as versatile materials with immense potential spanning multiple fields, signifying their role as promising candidates for a wide array of applications. (Gaharwar et al., 2019; Turunen et al., 2022)

Smectites possess several unique structural and morphological features included exchangeable cation in the interlayer, small particle size and a large specific surface area, making them a versatile material with extensive usage in geotechnical and industrial applications. For instance, smectites are integral in the composition of soils for agricultural purposes and can be applied in construction work. The key properties of smectites, such as cation exchange and swelling, are strongly influenced by their layer charge and lateral dimensions. Thus, the manipulation of the layer charge and lateral dimension of smectites is critical in determining their functionality and performance in various applications. Understanding the effect of layer charge and lateral dimension on the properties of smectites is essential in harnessing their potential in diverse fields. (Maes & Cremers, 1977, 1978; Shainberg et al., 1987; Slade et al., 1991; Laird, 1999, 2006; Christidis et al., 2006; Delavernhe et al. 2015). Low layer charge smectites are of particular interest as they provide a larger surface area for the incorporation of large cations, mainly organic molecules. This characteristic presents new opportunities for the development of hybrid materials. (Dultz et al., 2012; Jlassi et al., 2018). Therefore, a comprehensive understanding of the properties of low charged dioctahedral smectites is crucial for their potential applications in various fields, including materials science, geotechnical engineering, and catalysis.

2:1 layer silicates are classified according to the layer charge ($\xi = x/n = y+z$) per formula unit (p.f.u.) $M^{+}_{x/n}$ $(Si_{4-y}\ Al_{y})$ $[(Al, Fe^{3+})_{2-z}\ (Mg, Fe^{2+})_{z}]\ O_{10}\ (OH)_{2}$ (Guggenheim et al., 2006). Thereby a definition gap exists between the uncharged non-swellable pyrophyllite ($\xi = 0$) and the charged group of swellable clay minerals (smectites) with $0.2 \leq \xi \leq 0.6$ and no reliable experimental evidence exists for ξ in the range of $0 < \xi < 0.2$. Hence, the synthesis of dioctahedral and trioctahedral smectites with $\xi < 0.2$ is the prerequisite for the improvement of layer charge measurement. The target of synthesis will be the lower charged smectites, which have the value of layer charge $\xi = 0.1$, 0.125 and 0.18. Several synthetic and natural smectite samples (Laponite® RD, Volclay, Calcigel) were also selected for the investigation of layer charge and morphology.

A detailed description of synthesis, computational simulation, and experimental analysis methods is given in Chapter 2. The introduction of hydrothermal synthesis, and the computational simulation method using density function theory (DFT) including the design of low charge smectite model were presented. Particle size distribution and specific surface area investigation were measured and calculated by atomic force microscopy (AFM). Morphological and surface investigations were carried out using scanning electron microscopy (SEM). Qualitative and quantitative phase analysis was done using X-ray diffraction analysis (XRD) with Rietveld program Profex. A number of chemical analytical methods (X-ray fluorescence analysis (XRF), inductively coupled plasma - optical emission spectroscopy (ICP-OES), Solid-State Nuclear Magnetic Resonance Spectroscopy (NMR), determination of cation exchange capacity (CEC) and layer charge (ξ)) were applied to investigate the chemical composition, the interlayer composition and the exchange behavior. The comprehensive characterization of synthetic samples is presented, including a detailed description of their morphological, mineralogical, and chemical properties.

Chapter 3 focuses on closing the definition gap of low layer charged smectite, primarily through the synthesis of low charge synthetic trioctahedral and dioctahedral smectite by hydrothermal synthesis. However, the challenge appears when the synthetic smectite exhibits a layer charge value ($\xi < 0.2$) just below the measurable limit of the alkylammonium method (Lagaly, 1981, 1989, 1994). In such instances, the structural formula and chemical composition of the synthetic smectite become crucial, requiring assessment through full chemical composition of synthetic samples. The calculation of structural formula can predict the range of layer charge based on stoichiometry, establishing a foundation for future iterations of low charge smectite synthesis. This approach trying to extend the boundaries of layer charge measurement to a previously unwritten range, pushing the limits of understanding and analysis in this field.

The migration of water in the smectite interlayer will cause its swelling and shrinking behavior. Hydration and swelling behavior are both the significant properties of smectites. Therefore, in Chapter 4, the computational simulation on the hydration and swelling behavior of low-charge montmorillonite models has been studied. A theoretical study on the hydration of smectites (Emmerich et al. 2018) based on the DFT calculation indicates the existence of stable dioctahedral 2:1 layer silicates with $\xi < 0.2$ and substitutions either in the tetrahedral or octahedral sheet that are swellable, which is a groundbreaking finding for many applications of smectites. To support the synthesis result of low charged smectite and predict its hydration behavior, first-principles calculations by means of DFT were performed for the montmorillonite model with layer charge $\xi = 0.125$ to provide the simulation result of total energy and ground-state stable structure, with focus on the water molecules position, hydration state, influence of different interlayer spacing.

The objective of this study is to find evidence supporting the existence of low charge montmorillonites with layer charge $\xi < 0.2$. By combining theoretical analyses and synthetic results, this study aims to provide a solid basis for investigating the potential applications of low charged montmorillonite in various technological fields.

1.2 Smectite Group

Smectites (such as montmorillonite, saponite) are swellable clay minerals. The Clay Minerals Society (CMS) Nomenclature Committee defines smectite as a group of 2:1 layer silicates (Table 1.1) with $0.2 \leq \xi \leq 0.6$ negative layer charge. (Güven, 1988; Guggenheim et al., 2006). The definition gap of layer charge between pyrophyllite/talc and smectites is obvious but not explained by the committee or any previous literatures.

Table 1.1 Classification of 2:1 layer silicates.

Structure	Layer charge	Group	Minerals
2:1 layer silicates	$\xi \approx 0$	Pyrophyllite	Pyrophyllite
		Talc	Talc
	$0.2 \leq \xi \leq 0.6$	Dioctahedral smectite	Montmorillonite, Beidellite
		Trioctahedral smectite	Saponite, Stevensite
	$0.6 \leq \xi \leq 0.9$	Dioctahedral vermiculite	Dioctahedral vermiculite
		Trioctahedral vermiculite	Trioctahedral vermiculite
	$0.6 \leq \xi \leq 1$	Dioctahedral illite*	Dioctahedral illite
		Trioctahedral illite	Trioctahedral illite
	$\xi \approx 1$	Dioctahedral mica	Muscovite
		Trioctahedral mica	Phlogopite, Annite

*) Illites are now defined as interlayer deficient micas (Bergaya & Lagaly, 2013) but in literature the term illite is still more common.

A significant property of smectite group is their ability to undergo isomorphic substitutions in both the octahedral and tetrahedral sheets, which creates a negative layer charge. This charge is compensated by exchangeable cations that enter the interlayer space between two TOT layers. The layer charge per formula unit, represented by ξ, is a positive number that indicates the net negative charge per layer. For dioctahedral pyrophyllite and trioctahedral talc, which have no substitutions in the structure, the layer is electrically neutral, resulting in ξ values of 0. In contrast, micas have a layer charge close to 1. In this chapter, the focus is on the smectite group. Smectites are the most common 2:1 layer silicates and have negative layer charge ξ values ranging from 0.2 - 0.6, which resulting in the presence of hydrated cations in the interlayer. Structural formula calculations based on the chemical composition are reported based on the half unit cell (UC) and assume tetrahedral occupation by four cations with a completely occupied octahedral sheet, resulting in 22 negative charges per formula unit. (Emmerich et al., 2013).

1.2.1 Crystal Structure

The crystal structure of the smectite group belongs to the monoclinic system, with a 2:1 layer silicate structure composed of two silicon-oxygen tetrahedral sheets with an aluminum (or magnesium) oxygen octahedral sheet in between. The silicon-oxygen tetrahedrons are connected at a common vertex to form a silicon-oxygen tetrahedron sheet, which is located on the same plane and builds a hexagonal structure. The aluminum (or magnesium) oxygen octahedral sheet is composed of central cations (Al^{3+}, Mg^{2+}), with four oxygen atoms and two hydroxyl groups, which are provided by two opposing silicon-oxygen tetrahedral and adjacent octahedral sheets. The interlayer exchangeable cations (Na^+, K^+, Mg^{2+}, Ca^{2+}) are balanced by the interlayer negative charges due to the replacement of octahedral Al^{3+} by Mg^{2+} or the replacement of Si^{4+} at the tetrahedron by Al^{3+} in the crystal structure (Figure 1.1).

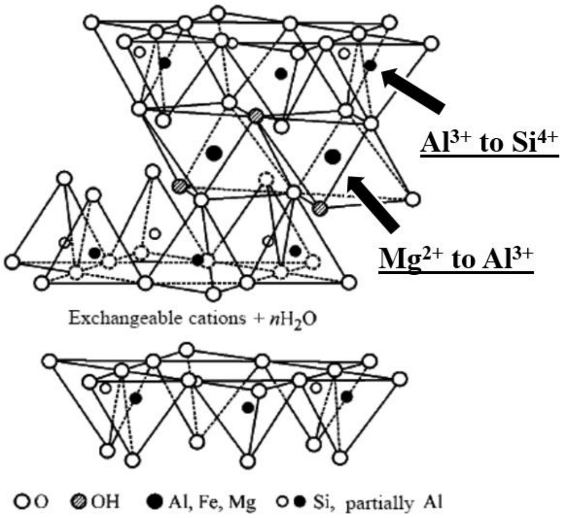

Figure 1.1 Basic structure of smectite. (according to Jasmund & Lagaly, 1992).

The chemical and physical characteristics of smectites are significantly affected by the substitution positions and the valence of cations within the sheet. Within the smectite structure, further classification is based on cation occupation within the octahedral sheet. For instances where trivalent cations (Al^{3+}, Fe^{3+}) occupy 2/3 of the octahedral positions, leaving 1/3 vacant, the resulting structure is termed dioctahedral (as seen in montmorillonite and beidellite). Conversely, when all octahedral positions are filled by divalent cations (Mg^{2+}, Zn^{2+}), it's referred to as a trioctahedral structure (as seen in saponite and sauconite) (Figure 1.2).

These diverse structural configurations significantly influence the properties exhibited by the smectite group, playing an important role in determining their behavior and characteristics. The general formula for dioctahedral and trioctahedral smectite are:

Dioctahedral species: $M^{n+}_{x/n}\ (Si_{4-y}\ Al_y)\ [(Al,\ Fe^{3+})_{2-z}\ (Mg,\ Fe^{2+})_z]\ O_{10}\ (OH)_2$

Trioctahedral species: $M^{n+}_{x/n}\ [\ Si_{4-y}\ (Al,\ Fe^{3+})_y\ ]\ [\ (Mg,\ Fe^{2+})_{3-z}\ ,\ (R^+)_z\ \square]\ O_{10}\ (OH)_2$

with layer charge $\xi = x/n = y+z$ (p.f.u.). R^{3+}, R^{2+} and R^{+} represent the common mono-, di- and trivalent octahedral cations and M^{n+} symbolize the interlayer cation, and □ stands for non-occupied (vacant) positions (Table 1.2).

Table 1.2 Most common smectite end-members (according to Emmerich, 2013).

Name	Formula unit
Dioctahedral species	
Montmorillonite	$M^{n+}{}_{x/n}\,(Si_4)\,[(Al^{3+})_{2-z}\,(Mg^{2+},R^{2+})_z]\,O_{10}(OH)_2$
Beidelite	$M^{n+}{}_{x/n}\,[(Si_{4-y})\,(Al^{3+})_y]\,[(Al^{3+},R^{3+})_2]\,O_{10}(OH)_2$
Nontronite	$M^{n+}{}_{x/n}\,[(Si_{4-y})\,(Al^{3+})_y]\,[(Fe^{3+},Al^{3+})_{2-z}\,(Fe^{2+},Mg^{2+})_z]\,O_{10}(OH)_2$
Trioctahedral species	
Hectorite	$M^{n+}{}_{x/n}\,(Si_4)\,[(Mg^{2+})_{3-z}\,(Li^{+})_z]\,O_{10}(OH)_2$
Saponite	$M^{n+}{}_{x/n}\,[(Si_{4-y})\,(Al^{3+})_y]\,[(Mg^{2+})_3]\,O_{10}(OH)_2$
Sauconite	$M^{n+}{}_{x/n}\,[(Si_{4-y})\,(Al^{3+})_y]\,[(Mg^{2+},Zn^{2+})_3]\,O_{10}(OH)_2$

Another important aspect of the structural and crystal chemical heterogeneity in dioctahedral smectite involves the distribution of octahedral cations between trans- and cis-sites. The tetrahedral sheets are always bonded to octahedral sheets through oxygen atoms. The octahedral sheet has unshared oxygen atoms forming hydroxyl groups. Typically, the octahedral sheet comprises two symmetrically cis-octahedrons divided by hydroxyl group and one trans-octahedron, which can be described as two cis-sites and one trans-site. One out of three octahedron is not occupied by cations, forming a vacant site. The disposition between vacant site at the octahedral sheet and hydroxyl groups determine two different structures, when the hydroxyl groups are on the same side (cis-vacant, cv) or on opposite sides (trans-vacant, tv) of the vacant site (Figure 1.2).

The presence of 2:1 dioctahedral layer silicates with one of the two symmetrically cis-octahedra vacant was initially reported by Méring and Oberlin in Wyoming montmorillonite (Méring & Oberlin, 1971). Extensive studies by Tsipursky and Drits revealed diverse occupancies of cis- and trans-octahedral sites in various dioctahedral smectites, encompassing cis-vacant (common in most montmorillonites) and trans-vacant samples (found in nontronites, beidellites, and certain montmorillonites), as well as samples exhibiting interstratified cv and tv layers. The primary determinant influencing cation distribution across trans- and cis-sites was the extent of Al^{3+} for Si^{4+} substitution (Tsipursky & Drits, 1984). The following research on the classification of smectite adds two additional structural features such as the charge location resulting from substitutions in both the octahedral and tetrahedral sheets, and Fe content within the structure to systematically classify smectite (Emmerich et al., 2009; Wolters et al., 2009). An extensive investigation by Kaufhold et al. into the correlations between the ratio of trans vacant to cis vacant structures, the fraction of charge in the tetrahedral sheet, and the Fe content. Consequently, it can be inferred that the observed increases in both the tv/cv ratio and the tetrahedral charge fraction are attributable to the increasing Fe content (Kaufhold et al., 2017).

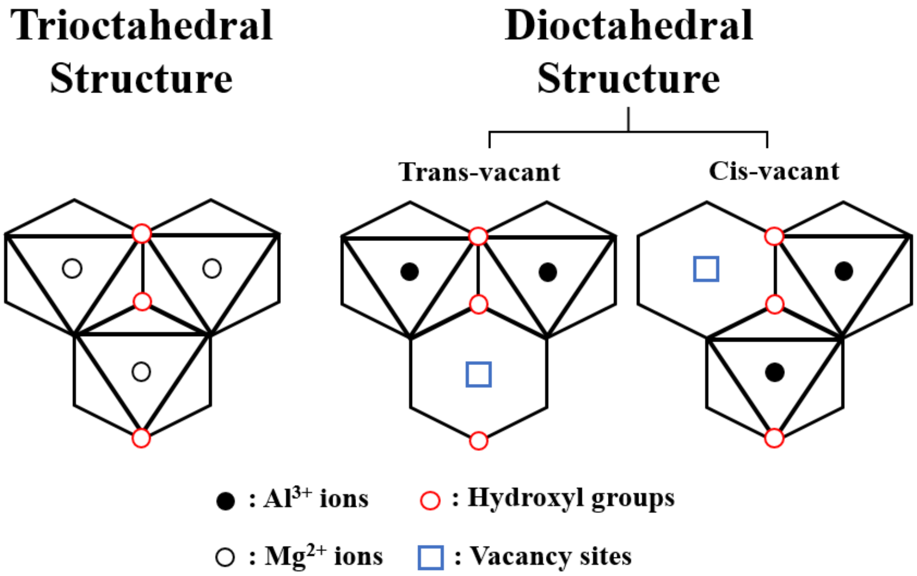

Figure 1.2 Hexagonal structure of the octahedral sheet of 2:1 layer silicate with trioctahedral & dioctahedral structure; distribution of octahedral cations in dioctahedral structure with cis- & trans-vacant structure. (Emmerich & Kahr, 2001).

1.2.2 Layer Charge & Cation Exchange Capacity

Within the smectite materials, the presence of negative layer charge and edge charge results in the accommodation of cations within the interlayer and at the edges, enabling their exchange with other cations. The most common interlayer exchangeable cations in smectite including Na^+ and Ca^{2+}. The quantification of cation exchange capacity (CEC) serves as a crucial analysis process of smectite research. The cation exchange equivalent describes the total amount of exchangeable cations adsorbed by a smectite of a certain pH, expressed as the number of cations adsorbed per kilogram of montmorillonite (cmol(+)/kg). This metric summarizes smectite's inherent ability to adsorb and exchange cations, indicating its potential reactivity and versatility in different environments.

Smectites possess two types of cation exchange capacities (CEC), one associated with interlayer sites and the other with edge sites (Figure 1.3). The interlayer CEC is related to the layer charge and exchange of cations in the interlayer space. On the other hand, the edge CEC is strongly influenced by pH, as the number of cations adsorbed at the edges is pH-dependent and the morphology (aspect ratio) of the 2:1 layers. The edge CEC can contribute up to 20% of the total CEC of smectites. Therefore, the overall CEC of smectites is significantly affected by the pH-dependent edge CEC (Lagaly, 1981). During the CEC measurement, the pH of zero charge at the edges ($pH_{PZC,\ edge}$) was studied, and for delaminated smectite, the range is around pH = 6 - 7 (Tombacz & Szekeres, 2004; Delhorme et al., 2010). When pH > $pH_{PZC,edge}$, it indicates that the edge CEC can contribute to and increase the total CEC of smectites. Therefore, the overall CEC of smectites is significantly affected by the pH-dependent edge CEC (Lagaly, 1981; Delavernhe et al., 2015, 2018).

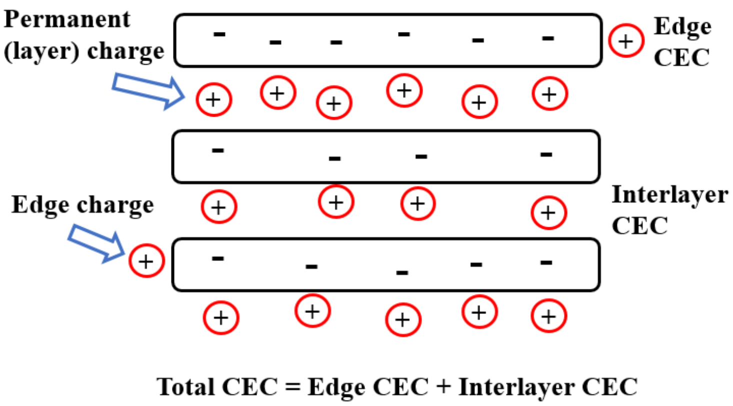

Figure 1.3 The distribution of permanent (layer) and edge charges in the structure and the calculation of cation exchange capacity of smectite.

The layer charge of the smectite is determined by the permanent charges in its structure, which can be located in either the octahedral or tetrahedral sheet. The tetrahedral charge is more localized compared to the delocalized charge in the octahedral sheet resulting from isomorphic substitution of Si^{4+} by Al^{3+} in the tetrahedral sheet or Al^{3+} by Mg^{2+} in the octahedral sheet, which contributes to the negative layer charge. The basal surface always has a negative charge due to substitutions in the sheets. Conversely, the charge of the edges is pH-dependent. At low pH, the edges are saturated with protons, giving them a positive charge. As pH increases, the protons are released, resulting in a decrease in the amount of positive charge until the edges become completely negatively charged at high, basic pH value.

In most cases, layer charge density is heterogeneous and the interlayer cation density varies from interlayer space to interlayer space. (i.e. individual smectite layers may differ in charge, with the total layer charge for a sample being an average of these different charges). To determine the layer charge density of smectite, alkylammonium method was applied by exchanging 14 different alkylammonium chains with smectite samples (Lagaly, 1981, 1989, 1994).

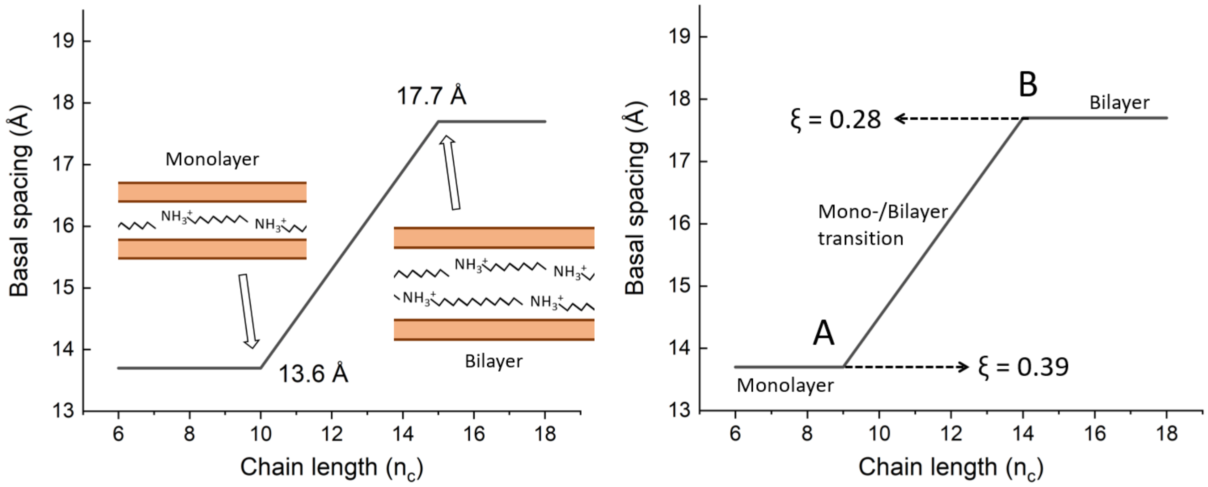

Figure 1.4 Left: The transition of Monolayer/bilayer structure of smectites after intercalated the alkylammonium ion; Right: The layer charge distribution from point A (highest interlayer cation density) to point B (lowest interlayer cation density) (Lagaly, 1981).

1.2.3 Hydration Property & Swellability

The hydration property of smectite is attributed to the movement of water molecules into or out of the interlayer spaces. Therefore, this results in a significant swelling in volume, it could increase about 12% larger than the original structure from the transition of mono-hydrated to bi-hydrated state. Smectite's crystalline swelling is characterized by a stepwise expansion of the layer-to-layer distance, as water activity increases. The main forces affecting the hydration of the interlayer cation are the hydration energy of the interlayer cation, polarization of water molecules by interlayer cations, variation of electrostatic surface potentials because of differences in layer charge location. Size and the morphology of the smectite affects the kinetic of hydration.

The stepwise increase in the layer-to-layer distance lead to the change of the basal spacing (d001), which is the sum of interlayer and 2:1 layer thickness, within the smectite structure due to rising water activity is a widely recognized phenomenon. This incremental expansion is ascribed to the inclusion of 1 to 3 layer of interlayer water molecules (Figure 1.5), leading to the formation of mono-hydrated (1W, d001 = 11.8 - 12.9 Å), bi-hydrated (2W, d001 = 14.5 -15.8 Å), and tri-hydrated (3W, d001 = 18.0 - 19.5 Å) states, alongside the dehydrated state (0W, d001 = 9.6 - 10.7 Å). It's noteworthy that these hydration states frequently coexist within smectites, persisting even under meticulously controlled conditions (Ferrage et al., 2016).

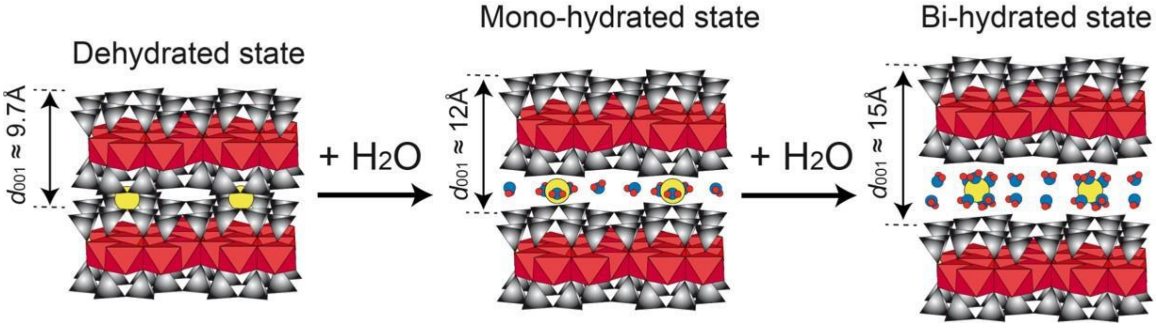

Figure 1.5 Schematic representation of crystalline swelling model and ranges of layer-to-layer distances (d001) (Ferrage, 2016).

The crystalline swelling in smectite involves the balance between attractive and repulsive forces, although Laird suggests that modeling is more effectively approached by considering potential energies (Laird, 1996). The attraction potential energy predominantly arises from electrostatic forces, specifically the Coulombic attraction between negatively charged surface sites resulting from isomorphous substitution and the positive charge of interlayer cations. Additionally, van der Waals interactions between adjacent layers may contribute to the overall potential energy of attraction. Conversely, the potential energy of repulsion stems from the partial hydration potential energy of interlayer cations, and to a lesser extent, the partial hydration potential energy of negatively charged surface sites. Introduction of water molecules into the smectite interlayer leads to the ordering of water molecules in proximity to charged ions, forming a shell around the ion through ion-dipole bonds of predominantly electrostatic nature. Therefore, the potential energy of repulsion from the cation is associated with the disparity between the hydration state of the cation in the interlayer and its potential hydration state in the equilibrating solution or atmosphere. Any alteration in the potential hydration state of an interlayer cation induces a corresponding change in the potential energy of repulsion (Laird, 2006).

1.3 Synthesis of Smectite

In the history of smectite material synthesis, during the early 1960s, the UK witnessed a milestone in smectite material synthesis with the creation of Laponite® products, marking one of the pioneering instances of industrially produced nanodimensional materials. These synthetic nanoclays, resembling hectorite and exhibiting remarkable and distinct properties, have since maintained sustained commercial success for the original UK-based company that patented and introduced them to the market (Neumann, 1966). Although hydrothermal synthesis of various trioctahedral and dioctahedral smectite has been extensively investigated afterwards, most of the literature has offered limited discussion or successful results on the synthesis and characterization of low-layer charge smectite. To address this gap in knowledge, it is essential to focus on the synthesis of dioctahedral and trioctahedral smectites with a layer charge $\xi < 0.2$. This approach is necessary to explore the unique properties related to low-layer charge smectite and is a crucial prerequisite for the development of improved layer charge measurement methods. Synthesis of smectite under different sets of conditions (high temperature and pressure, moderate or extreme hydrothermal environments, and the presence of fluoride) has been discussed for a long period, and some successful studies have provided sufficient synthetic methods for obtaining synthetic smectite. Pure phase and homogeneous materials can be synthesized through controllable synthesis system (Kloprogge et al., 1999; Zhang et al., 2010).

In recent years, numerous synthetic procedures have been developed for the preparation of smectite with controlled chemical composition and adjustable physico-chemical properties. The majority of these methods have been developed to mimic the natural processes that are involved in the formation of clay minerals, which usually take place over extended periods of time through hydrothermal processes. These synthetic procedures have been optimized to produce clay minerals in a shorter time frame compared to natural processes by adjusting various parameters such as temperature, pressure, and the composition of the synthesis hydrogel. Several crucial parameters, such as crystallization time and the presence of fluorine within the hydrogel, exert substantial influence on product purity and crystallinity. Optimal synthesis conditions typically involve a specific timeframe to attain pure smectite depend on different type of synthetic smectite; deviations towards shorter or longer reaction times result in impurities or decrease the smectite purity. The absence of F cations within the hydrogel impedes the crystallization of phyllosilicates, yielding amorphous silica instead. Therefore, the introduction of small amounts of fluorine is indispensable for the crystallization of synthetic montmorillonite (Table 1.3).

Based on the aforementioned studies, hydrothermal synthesis has been identified as the most viable method for producing pure smectite (Table 1.4). The synthesis of high-purity smectite necessitates careful consideration of various factors, including the combination of starting materials, reaction time, and temperature. Despite these efforts, the challenge lies in the inevitable formation of amorphous phases and impurities during the synthesis process. This complicates the accurate determination of purity and the percentage of the amorphous phase in the final product, posing difficulties in precisely assessing the quality of the synthesized smectite. For instance, a certain amount of reaction time is required to generate a relatively pure smectite phase. While increasing the temperature can reduce reaction time and enhance sample crystallinity, it may also lead to the formation of impurity phases and increase the risk of damaging the Teflon container in the autoclave.

Table 1.3 General experimental parameters and experience for smectite synthesis.

Experimental parameters	**Details of materials and factors**	**Experimental experience**
Starting material of hydrogel	**Si source:** SiO_2, Na_2SiO_3, TEOS (Tetraethyl orthosilicate) **Metal source:** Li-, Na-, Mg-, Zn-, Al- chlorides, nitrates, acetates, carbonates **Mineralizer:** HF, NaF, NH_4F	**Best Si source:** Trioctahedral saponite: Na_2SiO_3 Dioctahedral montmorillonite: SiO_2 (Aerosil 130) **Best mineralizer:** HF (40%)
Synthesis temperature	**Extreme:** > 500 °C **Moderate:** 100 - 350 °C **Low:** 3 - 90 °C	**Best range:** Trioctahedral saponite: 200 °C Dioctahedral montmorillonite: ≥ 220 °C
Synthesis pressure	**Extreme:** > 20 MPa **Moderate:** P_{H_2O} **Low:** Ambient pressure	**Autogenous pressure:** ≤ 3 MPa
Initial pH of hydrogel	5 – 10	**Best Initial pH range:** Trioctahedral saponite: ≥ 7 Dioctahedral montmorillonite: 5 - 7
Reaction time	4 h - 288 Days	**Best reaction time:** ≥ 72 h

Figure 1.6 Hydrothermal Autoclave Reactor (Techinstro, India).

1.3.1 Synthesis of Trioctahedral Smectite

The synthesis of trioctahedral smectite in this work focused on trioctahedral saponite. In general, the synthesis of saponite is promising under a wide range of hydrothermal conditions compare to the synthesis of dioctahedral montmorillonite. First at the early 1960s, Neumann achieved a milestone with the creation of Laponite® products, marking one of the pioneering instances of industrially produced nanoclay materials. These synthetic hectorite and exhibiting remarkable and distinct properties (Neumann, 1962). Hickson used Silica gel, $Al(OH)_3$, $Mg(OH)_2$, NH_4OH and NH_4F at 300 - 350 ℃ for 4 h, pH 9 - 10 to obtain synthetic saponite (Hickson, 1974, 1975). Decarreau added appropriate amount of Na_2SiO_3 and different metal salts (Mg, Al, Fe, Co, Ni, Zn) in acid solution to produce a small amount of saponite and improve its crystallinity (Decarreau, 1980, 1985). Vogels et al. used Si-Al gel and urea and nitrates (Zn, Mg, Ni, Co) to react at 90 ℃ for 5 - 20 h to synthesize saponite and it also mentioned that the number of divalent ions in the octahedron will affect the surface properties of saponite, such as orderly stacking, specific surface area, and pore volume (Vogels et al., 1995). Since the nucleation growth rate of synthetic products containing Mg is much slower than that of Zn and Co, and their stacking is more disordered, the 001 peak tends to be broadened. Base on the research of Kloprogge et al., the surface and structural properties of saponite can be changed by the dilution of synthetic gels (Kloprogge et al., 1993) and Bisio et al controlled the ratio of H_2O/Si to synthesize saponite after holding the temperature at 240 ℃ for 72 h. XRD results show that when $H_2O/Si = 20$, 001 peak of final product has a strong diffraction. (Bisio et al., 2008) Some research has attempted to synthesize saponite containing different divalent cations in the interlayer to obtain products for advanced applications (Trujillano et al., 2015). Recently well-crystalized synthetic trioctahedral samples can be obtained at moderate conditions with a wide temperature range between 90 and 220 ℃ and different treatment of starting material. (Meyer et al., 2020).

In general, the formation of trioctahedral smectite (saponite) is possible under a wider range of hydrothermal conditions. Moderate conditions with temperatures between 100 and 575 ℃ with autogenous pressures are most promising in terms of growth rate, yield, and purity. In the synthesis of trioctahedral smectite, a hydrogel can be prepared by mixing all starting materials in deionized water and then matured at room temperature for around 2 h under a neutral pH between 5 and 7. The hydrogel is subsequently subjected to hydrothermal treatment in a Teflon-lined stainless-steel autoclave (Figure 1.6) at 200 ℃ for 72 h, with autogenous water pressure which depends on the amount of filling volume in the Teflon container (≤ 3 MPa). The resulting products are separated by centrifugation, thoroughly washed with distilled water, and subsequently dried at 60 ℃ for 24 h. The dried samples are ground into a fine powder and stored under controlled humidity conditions.

1.3.2 Synthesis of Dioctahedral Smectite

For further applications of synthetic dioctahedral smectite, high phase purity is crucial. The difficulties in synthesizing dioctahedral smectite are due to the poor reactivity of SiO_2 (HF is needed as mineralizer) and to control the substitutions rate in octahedral sheets. Harder used

SiO_2, $Al(OH)_3$ and $Mg(OH)_2$ to synthesize montmorillonite by chemical coprecipitation method at a low temperature of 3 - 60 ℃. (Harder, 1972, 1977) Yamada et al applied hydrothermal synthesis to obtain montmorillonite-beidellite at 250 - 500 ℃ and 100 MPa. The XRD analysis showed that a smectite-beidellite mixed layer structure was produced at 400 ˚C and a single phase of montmorillonite can be synthesized at a temperature of 375 ˚C. (Yamada et al. 1991, 1993) The most significant reference of successful synthesis is according to the molecular formula of montmorillonite, $Na^+_{x+y}(Si_4)[(Al^{3+})_{2-y}(Mg^{2+})_y]O_{10}(OH)_2$ is heated to 220 ˚C for 72 h in the system of Na_2O-MgO-Al_2O_3-SiO_2 and an appropriate amount of F is added as Mineralizer to synthesize montmorillonite (Reinholdt et al., 2001, 2005). Lantenoids et al also synthesized the dioctahedral series of montmorillonite by hydrothermal method, discussing the synthesis of montmorillonite under different pressure and interlayer charge of $0.6 \geq \xi \geq 0.25$. When temperature is around 320 ℃, and the pressure parameters are 120 MPa, and 200 MPa respectively, a single-phase montmorillonite can be obtained. (Lantenoids et al. 2008) In addition, another research was to modify the specific surface area and crystal form of montmorillonite samples by changing the combination of different parameters (Mg-Al ratio, heating temperature, heating time, and pressure) (Golubeva, 2016). Based on the above studies, most successful synthesis results indicate that higher synthesis temperature and pressure (when TEOS as Si source and initial $pH > 7$ of hydrogel) and the participation of mineralizer (SiO_2 as Si source) with a more precise ratio to the starting material are required in the reaction.

The synthesis process and chemical composition of dioctahedral smectite are more limited in comparison to trioctahedral smectite. Base on the experimental experience and lectures, synthesis of dioctahedral smectite was achieved by utilizing an acidic fluoride medium, as small amounts of fluoride ($F/SiO_2 = 0.05$) were necessary for the formation of pure montmorillonite. The selection of chemicals utilized in the process was specific, and the proportion of water, hydrofluoric acid (mineralizer), and silicon oxide remained constant in each synthesis. The addition of reactants followed a specific order (DI water → HF → Na → Mg → Al → Si). During the hydrothermal process, all other experimental conditions remained the same with the synthesis of trioctahedral smectite.

Table 1.4 References of starting materials and experimental parameters of previous dioctahedral and trioctahedral smectite synthesis.

Authors	**Starting Materials**	**Conditions**				**Products**
		T (°C)	**Time**	**pH**	**Pressure**	
Meyer et al. (2020)	Na_4SiO_4, $Mg(NO_3)_2$, $Al(NO_3)_3$	90-200	120 h	7, 10	P_{H2O}	Saponite
Golubeva (2018)	SiO_2, $NaCOOCH_3$, $Mg(COOCH_3)_2$, HF	220	24-120 h	4-4.5	P_{H2O}	Montmorillonite
Golubeva (2016)	Tetraethyl orthosilicate (TEOS) $Mg(NO_3)_2$, $Al(NO_3)_3$, HNO_3, NH_4OH, ethyl alcohol	200-350	5-288 h	>7	20-70 MPa	Montmorillonite, Saponite
Le Forestier et al. (2010)	TEOS, $Mg(NO_3)_2$, $Al(NO_3)_3$, Na_2CO_3, NH_4OH, ethanol	350	288 days	>7	120 MPa	Montmorillonite
Lantenois et al. (2008)	TEOS, $Mg(NO_3)_2$, $Al(NO_3)_3$, HNO_3, NH_4OH, Na_2CO_3, ethanol	320	30 days	>7	≥120 MPa	Montmorillonite, Amorphous phase
Bisio et al. (2008)	SiO_2, $Al[OCH(CH_3)_2]_3$, $Mg(CH_3COO)_2$, NaOH	240	72 h	8-9	P_{H2O}	Saponite
Golubeva et al. (2005)	Silica gel, MgO, $Mg(OH)_2$, NaOH	250-350	0.5-7 h	>7	70 MPa	Montmorillonite
Reinholdt et al. (2001, 2005)	SiO_2, AlO(OH), $Mg(CH_3COO)_2$, $Na(CH_3COOH)$, HF	220	72 h	5-5.5	P_{H2O}	Montmorillonite
Vogels et al. (1995)	Na_2SiO_3, SiO_2, $GaCl_3$, NaOH, $Na_2B_4O_7$, nitrates (Zn, Mg, Ni, Co)	90	20 h	>7	0.1 MPa	Saponite
Kloprogge et al. (1993)	SiO_2, $Al[OCH(CH_3)_2]_3$, $Mg(CH_3COO)_2$, NH_4OH	125-300	72 h	>7	P_{H2O}	Saponite

Yamada & Nakazawa (1992)	SiO_2, Al_2O_3, MgO, Na_2CO_3	250-500	2-129 days	>7	100 MPa	Montmorillonite, Beidellite
Yamada & Nakazawa (1991, 1993)	SiO_2, Al_2O_3, MgO, Na_2CO_3	1600	10-50 min	>7	5.5 GPa	Montmorillonite, Coesite, Jadeite, Kyanite
Decarreau (1980, 1985)	Na_2SiO_3, chlorides (Mg, A1, Fe, Co, Ni, Zn)	＜100	X	>7	1 atm	Saponite, Hectorite, Stevensite
Harder (1972, 1977)	SiO_2, $Al(OH)_3$, $Mg(OH)_2$	3-60	X	>7	P_{H2O}	Montmorillonite, Amorphous phases
Hickson (1974, 1975)	Silica gel, $Al(OH)_3$, $Mg(OH)_2$, NH_4OH, NH_4F	300-350	4 h	9-10	P_{H2O}	Saponite

1.4 Quantum Mechanics (QM) & Molecular Dynamics (MD) Calculation

Advancements in molecular modeling techniques have enabled a comprehensive exploration of the interlayer structure of clay and the impact of hydration on its configuration. Molecular modeling's value becomes evident in comprehending chemical reactions deeply. The dynamics of hydration/dehydration and the crystallographic swelling tendencies of montmorillonite have been extensively explored in numerous computational studies utilizing molecular dynamics (MD) and empirical force field methodologies. In 1991, Skipper et al. conducted pioneering work by simulating the interlayer water structure of Na and Mg saturated montmorillonite using Monte Carlo (MC) and MD methods. Subsequently, in 1995, they introduced a comprehensive MC simulation method for a clay mineral-cation-water system, laying a foundation for future molecular simulation studies of smectite model (Skipper et al., 1991, 1995). Building upon this, Marry et al. employed MC and MD simulation methods to investigate Na and Cs saturated montmorillonite, comparing their structural and kinetic characteristics with experimental data. Their results showed close agreement between the layer spacing, diffusion coefficient of water molecules, and interlayer cations in a single layer hydrate calculated via molecular simulation and experimental measurements (Marry et al., 2002).

At the same period of time, quantum mechanics (QM) methodologies have been also instrumental in scrutinizing interactions within smectite systems. Chatterjee et al. carried out density functional theory (DFT) simulation to study smectite−cation−water interaction in montmorillonite and beidellite. (Chatterjee et al., 1999). After that, more and more QM simulations have been devoted to the study of montmorillonite model. Most of the investigations have specifically employed QM with ab initio thermodynamic calculations using DFT to assess a restricted range of smectite structures (Chatterjee et al., 2004; Berghout et al., 2010; Emmerich et al., 2015; Fonseca et al., 2017). QM serves as a proper tool to investigate smaller and restricted systems compared to MD (Seppälä et al., 2016). For decades, thorough investigations into montmorillonite swelling using molecular modeling have persisted. The differences among structures have been recognized as pivotal factors capable of exerting significant influence on the observed swelling properties. The choice between two calculations allows for the exploration of diverse research subjects and smectite systems. Both methodologies yield valuable insights, including the determination of basal spacing, and enable comparisons across a range of system scales, from slightly larger to smaller-scale systems. Additional results, such as the size of super cells and the number of water molecules, obtained from both calculations, can be compared with experimental data.

MD and QM calculations serve different purposes in computational chemistry, and their precision depends on the characteristics of the system. Regarding the scope and scale, MD is well-suited for studying large-scale systems and dynamic processes, offering insights into the macroscopic behavior of materials over time by simulating the movements of atoms or molecules. In contrast, QM focuses on the electronic structure and properties, proving effective for small-scale systems and providing detailed information about electronic interactions, bond formation, and energy levels. To compare these two calculations, MD simulations can capture complex interactions and dynamic behaviors but relying on force fields to describe interatomic interactions. These force fields may have limitations, and accuracy can vary based on chosen parameters. QM calculations, when applicable, offer higher precision in describing electronic properties, bond lengths, and energies. However, their computational cost increases with system size. In summary, the choice between MD and QM depends on the research goals and the nature of the system being studied. MD is more suitable for understanding dynamic processes and large-scale behavior, while QM is preferred when accurate electronic details are essential. Often, a combination of both calculations is employed to leverage the strengths of both. (Schlick, 2010; Lee, 2016; Jensen, 2017; Sholl & Steckel, 2022).

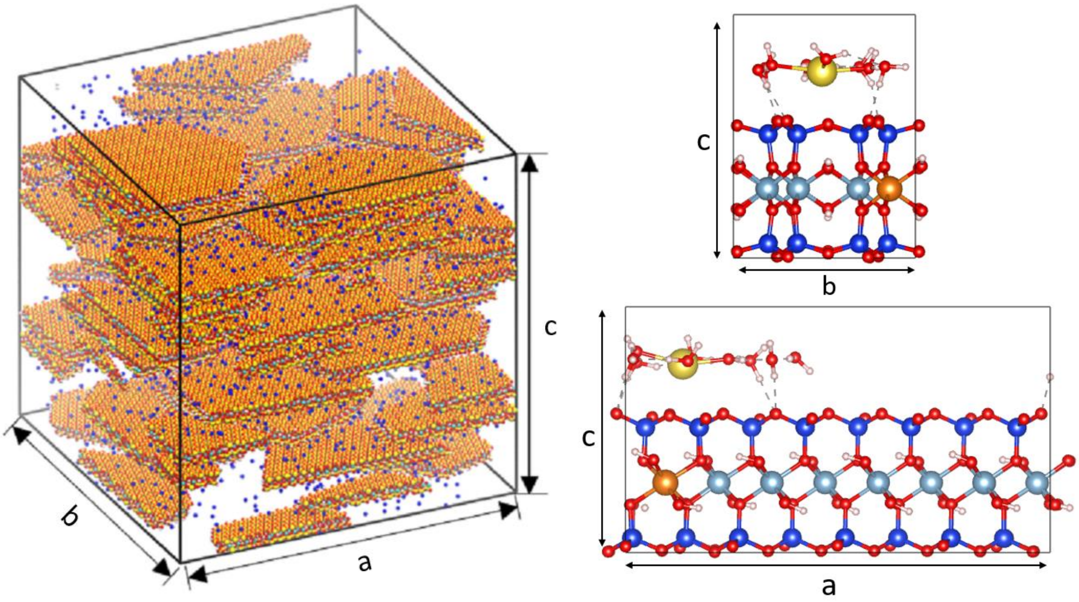

Figure 1.7 Left: Snapshots of the MD simulated system assemblage of 27 Na saturated montmorillonite particles. (Zheng et al., 2023); Right: Snapshots of the DFT simulated Na saturated montmorillonite supercell with 4 unit cells.

Back to the simulation of montmorillonite model, in MD simulations, using a simulation supercell large enough helps to describe the specific chemical interactions in the system, allowing comparisons with different types of smectites. MD calculations are flexible to adjust the parameters for simulating montmorillonite models compared to QM calculations, offering various environmental settings. These include controlling ambient humidity, determining the position and mobility of water molecules (For example, with the force field CLAYFF, water molecules can move freely in and out of the clay particle), setting the system temperature, and allowing the layer structure to relax freely during the calculation. The versatility of MD simulations allows researchers to explore different conditions, enabling a more comprehensive understanding of the dynamic behavior and response of montmorillonite systems to different environmental factors, the simulated data not only reveals basal spacing but also predicts self-diffusion coefficients and density distributions of interlayer water and cations. MD calculations can also reproduce the formation of water layers in the interlayer of montmorillonites to mimic natural samples successfully. On the other hand, for small-scale and specific smectite structures, particularly when considering the contribution of potential energy from van der Waals interactions within the interlayers, QM calculations are the preferred approach and can provide higher accuracy. This is promising when investigating the effects of substitution locations, different layer charges, and interlayer cations. The DFT simulations can provide a detailed and accurate understanding of the electronic structure, bond formation, and energetics at the atomic level. This level of precision is important for revealing the complexity of smectite structures where small variations in parameters can significantly impact the behavior. By utilizing calculations, researchers can have a deeper understanding of the molecular-level interactions and structural features that control the properties of the smectite under various conditions. (Cygan et al., 2009; Greathouse & Cygan, 2013; Rotenberg et al., 2014; Seppälä et al., 2016; Min et al., 2022).

Natural smectites are always characterized by layer charge distribution; that is, natural samples comprise 2:1 layers of different layer charges. A layer charge lower than 0.2 was included because of the still-existing definition gap that separates pyrophyllite ($\xi = 0$) from dioctahedral smectites ($0.2 \leq \xi \leq 0.6$). Therefore, the stable hydration state and swellability of low charged smectite remain unknown. In our study, QM simulations are applied to study the swelling behavior of trans-vacant and cis-vacant low layer charged montmorillonite model ($\xi = 0.125$ per FU) in different water content. Calculations were performed with supercells (SCs) comprising 4 unit cells (UCs). The stoichiometric formulae can be written by $Na_1[(Si_{32})(Al_{15}Mg_1)O_{80}(OH)_{16}]$ with one interlayer Na and Mg to Al substitutions in octahedral sheets.

1.4.1 Quantum Mechanics (DFT Simulation)

Numerous experimental endeavors and simulations employing diverse clay models have investigated various clay properties. The observed swelling behavior of clay minerals indicates a stepwise process, characterized by the sequential formation of one, two, and three water layers within the interlayer space. (Boek & Sprik, 2003; Tambach et al., 2006; Zheng et al., 2011). The quantity of water present in the interlayer space is contingent upon various factors, encompassing the nature of cations and their corresponding hydration energies, the layer charge, chemical potential, and relative humidity. Quantifying the extent of swelling involves measuring both the basal spacing and water content, thereby establishing their dependence on factors such as relative humidity, temperature, external pressure, and salt concentration. These parameters delineate the dynamic interplay governing the expansion of the interlayer space in response to environmental changes. (Bergaya & Lagaly, 2013; Tajeddine et al., 2015).

Despite the DFT calculation has a long history in the field of material science, here we are focusing on the clay material. For Na saturated montmorillonite model, several research using different DFT functional studied the dehydrated model to simulate the swelling properties with different factors, which including different exchangeable cations, cation arrangement, trans- or cis-vacant structure and different structure arrangement with various k-points number. (Sainz-Diaz et al., 2005; Hernandez-Laguna et al., 2006; Tunega et al., 2007) Start from 2010, many studies of hydrated montmorillonite model were described. The effect of the hydration degree (with 0, 4, 6 H_2O/Na^+) and different interlayer cations (Na^+, Mg^{2+}, Ca^{2+}, Sr^{2+}, Ba^{2+}) on the structure expansion of the interlayer space was analyzed (Berghout et al., 2010). Another work showed the simulation result of hydration/adsorption behavior of alkali cations (Li^+, Na^+, K^+) in the swelling process of montmorillonite, based on PBE functional, considering three types of isomorphic substitutions in the smectite layer: tetrahedral (beidellite-type structure), octahedral (montmorillonite-type structure) and both (Mignon et al., 2010). Apart from alkali cations saturated montmorillonite, the investigation of NH_4^+ intercalation holds particular significance within the fields of petroleum engineering, soil science, and environmental research. The adsorption and hydration of NH_4^+ in the interlayer space of montmorillonites were investigated using periodic density functional theory calculations with the PBE functional with dispersion correction. During the hydration, all the incoming water molecules bind with the surface via hydrogen bond regardless of their interaction with NH_4^+, showing that the surface activity affect the hydration of NH_4^+ in the interlayer the most (Shi et al., 2013).

DFT simulations are commonly employed to investigate factors such as different layer charge, swelling behavior and the basal spacing during the hydration state in montmorillonite structures. Numerous calculations, focusing on models with the same layer charge and varying water molecules in the interlayer, have been conducted. Despite minor deviations in basal spacing values, the results exhibit variation across different DFT functions. Starting from the early research, Na saturated montmorillonite models with 1 unit cell per supercell and layer charge $\xi = 0.5$ have been studied in dehydration state and with different water molecules in the interlayer. The dehydration models have the simulated basal spacing range from 9.6 - 10.1 Å, which is match the result of the natural dehydrated montmorillonite (Chatterjee et al, 2004; Sainz-Diaz et al., 2005; Hernandez-Laguna et al., 2006; Voora et al., 2011; Shi et al., 2013, Emmerich et al., 2015; Li et al., 2016; Fonseca et al., 2017; Prasad et al., 2023). However, the hydrated models appear to have basal spacing variation when different DFT function were implemented, for example, the basal spacing of models with 4 H_2O/Na^+ in the interlayer range from 12 - 12.6 Å by PBE and PW91 functionals are in good agreement (Fonseca et al., 2017), only the simulated result with 4 H_2O/Na^+ by BYLP functional is 11.5 Å and lower than the above range (Chatterjee et al, 2004). Another research keeps adding the number of water molecules up to 7 H_2O/Na^+, the basal spacing can reach to 14 Å or higher, which is in the transition stage of 1W to 2W state (Emmerich et al., 2015). The different layer charge of the montmorillonite model can also be comparison. Na saturated montmorillonite models with layer charge $\xi = 0.33$ have been studied, two research were applied PW91 functional but one of them was calculated without the dispersion corrections (the semiempirical van der Waals correction was not included) showed that when 4 H_2O/Na^+ in the simulated model, the overestimation of basal spacing happened (Seppälä et al., 2016). Another model's incorporation with 4 H_2O/Na^+ in the interlayer with a one-layer arrangement results in the expansion of the d001 parameter from 10.13 Å (dehydrated) to 12.81 Å, which is more reasonable compare to the experimental data. These findings highlight the challenges of conventional DFT computations in adequately capturing van der Waals interactions, leading to limitations in predicting equilibrium structures and bulk properties for certain systems. (Pirillo et al., 2015). In order to have more information for the study of lower charge model. The Na saturated montmorillonite model with 2 unit cells per supercell and layer charge $\xi \leq 0.25$ was first calculated from the research of Berghout et al by PW92 functional, it showed that when 4 and 6 H_2O/Na^+ were added into the structure, the basal spacing are 12.43 and 12.53 Å which are close to the available experimental results (Berghout et al., 2010). Even when they used two different DFT functionals, other research from Emmerich et al presented similar results by PW91 functional (Emmerich et al., 2018).

Although on previous research, the swelling of montmorillonite caused by multiple factors have been extensively studied, but information of the effect of single factor and the credibility of the calculated basal spacing value are lacking and need further verification. The research from Seppälä studies the factors of layer charges ($\xi = 0.2 - 0.6$) and different interlayer cation Na^+, K^+, Ca^{2+}. This research systematically compares the result of DFT calculation with MD calculation to examine the comparability of simulation studies and experimental data (Seppälä et al., 2016). To broaden the study range of layer charge in the simulation, the important research from Emmerich et al showed that Na saturated montmorillonite model with 4 unit cell per supercell and layer charge of 0.125 are swellable, which reduces the definition gap between uncharged and charged 2:1 layer silicates. This result provides the motivation for the further research to close the definition gap of the smectite (Emmerich et al., 2018).

Several standard DFT functionals were described and used in previous research, but it’s difficult to describe long-range dispersion interactions correctly, and usually overestimate the lattice parameters along the stacking direction. An investigation demonstrated that the lattice parameters calculated using dispersion corrections by DFT-D2 and vdW-TS methods are in excellent agreement with the experiment compare to PBE functional (Voora et al., 2011). Later research of Fonseca et al. focused on hydration/dehydration process discussed hydrogen bonding and van der Waals interactions are expected to be one of an important contribution to the cohesion of materials with layered structure. DFT-D2 and vdW-DF methods have been proposed for correcting DFT for dispersion. Despite a good agreement between calculated and experimental values of basal spacing can be considered for all examined DFT such as PBE and PW92 functionals, but with the DFT-D2 method has showed data slightly more accurate. The research used the dehydration temperature of PBE result compared with those obtained with DFT-D2 method and the result from DFT-D2 is in better agreement from TGA/DTG experiment results (Fonseca et al., 2017). Therefore, the use of the PBE functional integrating a more advance DFT-D3 correction (Grimme et al., 2010, 2011) can be a potential and more reliable method to describe the structures and the hydration of the Na saturated low layer charged montmorillonite model.

Table 1.5 References of calculated basal spacing (d001) and number (H_2O/Na^+) or layer (dehydrated 0W, mono-hydrated 1W, bi-hydrated 2W and tri-hydrated state 3W) of water molecules of Na saturated montmorillonite by DFT simulation (all references using trans-vacant model except Sainz-Diaz et al. (2005) using both trans-vacant & cis-vacant models).

Authors	**ξ/FU**	**UC per SC**	**No. of Na^+**	**No. of Water**	**H_2O/Na^+**	**d001 (Å)**	**DFT Functional**
Prasad et al. (2023)	0.5	1	1	0 2 4 6 8	0 2 4 6 8	9.7 11 - 12 12 12.5 14 - 15	DFT-D2 (Structural Optimization) & PBE
Emmerich et al. (2018)	0.125 0.25	4 2	1	0 - 9 (ξ = 0.125) 0 - 11 (ξ = 0.25)	0 - 9 0 - 11	10.38 - 13.39 10.36 - 13.56	PW91
Fonseca et al. (2017)	0.5	1	1	0, 4 (1W), 12 (2W)	0, 4, 12	10, 12.58, 15.94 9.51, 12.33, 15.51 9.80, 12.62, 15.91 9.79, 12.39, 16.16	PBE DFT-D2 vdW-TS PBEsol
Li et al. (2016)	0.5	2	2	0	0	9.93	PBE & DFT-D2
Seppäla et al. (2016)	0.33	3	2	0 1 - 10	0 - 5	10.78 13.0 - 17.5	PBE (Structural Optimization) & PW91
Pirillo et al. (2015)	0.33	1.5	1	0 4	0 4	10.13 12.81	PW91 (with dispersion corrections)
Emmerich et al. (2015)	0.25 0.5	2	1 2	0 - 14	0 - 14 0 - 7	10 - 14.8 10 - 14	PW91

Shi et al. (2013)	0.5	1	1	0	0	9.62	PBE-GGA
Voora et al. (2011)	0.5	2	2	0	0	9.83 9.32 9.47	PBE DFT-D2 vdW-TS
Berghout et al. (2010)	0.25	2	1	0 4 6 (1W) 6 (2W)	0 4 6	10.24 12.43 12.53 14.93	PW92
Hernandez-Laguna et al. (2006)	0.5	1	1	0	0	9.64 - 10.23	PBE-GGA
Sainz-Diaz et al. (2005)	0.5	1	1	0	0	9.77 - 9.87	PBE-GGA
Chatterjee et al. (2004)	0.5	1	1	0 4	0 4	10.17 11.51	BLYP

1.4.2 Molecular Dynamic

MD simulations model the motion of atoms and molecules over time, widely applied to study materials like clay minerals such as montmorillonite. Using different force fields to depict interactions between atoms, these simulations encompass parameters for bond stretching, angle bending, and van der Waals forces, capturing the atomic-level behavior. Interactions within montmorillonite involve forces between atoms in layers and interactions between layers. In hydrated montmorillonite simulations, water molecules are incorporated. Conducted under varying temperature and pressure conditions, MD simulations mimic real-world scenarios, crucial for understanding montmorillonite's behavior in diverse environments. Analyzing structural properties, the simulations extract information about layer spacing, density profiles, and water molecule dynamics within the interlayer space. These simulations also investigate swelling behavior, revealing insights into interlayer spacing changes due to water presence. MD simulations, run for extended periods, enable the study of montmorillonite's long-term behavior, offering insights into equilibration processes and system stability.

Several techniques have been developed for the experimental analysis of clay systems, with X-ray diffraction (XRD) (Ferrage et al., 2005, 2007), thermal analysis (Emmerich et al., 2017), and Fourier transform infrared spectrum (FTIR) (Kaufhold et al., 2012) standing out as the most significant tools in smectite research. However, these experimental methods face challenges in providing a detailed, molecular-scale interpretation of the data or in studying the interaction of interlayer cations and H2O molecules within the clay layers. To address this limitation, molecular dynamics (MD) simulations (Zhang et al., 2016; Peng et al., 2021) and Monte Carlo (MC) simulations (Boek et al., 1995; Skipper et al., 1995a, 1995b; Chávez-Páez et al., 2001) have emerged as effective means to explore the structure, dynamics, and energetics of hydrated species in or on clay minerals. MD simulations, in particular, offer insights into the atomic-level details of clay systems, complementing and interpreting experimental measurements. These computational approaches provide a molecular perspective that aids in understanding the behavior of water molecules and interlayer cations within clay structures.

Density distributions of interlayer water and cations, swelling behavior, and effect of layer charge on the hydration of clay models were widely investigated by MD simulation. The research from Tao et al performs MD simulations to investigate the role of the monovalent and divalent cations K, Na, Ca on the stability and swelling of montmorillonite, and it found that Ca saturated montmorillonite exhibits less swelling than Na and K saturated montmorillonites for a given water content (Tao et al., 2010). Teich-McGoldrick et al found that the two-layer hydrates occur at the much lower water contents for montmorillonite model with octahedral layer charge due to the weak ion-surface interaction compare to the beidellite model. The magnitude of the layer charge has also an important effect on the hydration states in montmorillonite (Teich-McGoldrick et al., 2015). Yang et al.'s study used MD to simulate the swelling and interlayer hydration mechanism of Na saturated montmorillonite under various water loads, alongside examining the impact of ion hydration on the molecular level of the double electric layer, especially considering water molecule interactions. The simulation results provide information on ion distributions and the hydrated coordination structures in the interlayer. Furthermore, as the water load increases, the hydration states of Na saturated montmorillonite can reach up to the 5W hydration state, which corresponds to approximately 24.8 Å (Yang et al., 2017). The research of Ho et al using MD simulation to investigate the transition states between a dry interlayer, one-layer hydrate (1W), and two-layer hydrate (2W). It showed that layer to layer hydrogen bonding significantly contribute to the energy barrier of the 0W to 1W transition and the 1W to 2W transition was characterized by the change in interlayer water structure (Ho et al., 2019). Qiu et al. investigated the crystal chemistry properties of Na saturated montmorillonite model and revealed that the diffusion of water molecules and interlayer Na are strongly influenced by the layer charge density and isomorphic substitution ratio respectively (Qiu et al., 2020). Chen et al provided a detailed examination of the transition states during the hydration of smectite. The initiation of crystalline swelling occurs with the detachment of cations from the clay surface, leading to the formation of a water molecule shell around these cations within the interlayer space. The complete hydration of cations induces the clay to undergo swelling, transitioning from the 1W to the 2W hydration state. Significantly, the dynamics of clay swelling are influenced by factors such as layer charge, smectite structure, and interlayer cations (Chen et al., 2022).

A critical observation from the above description highlights the indication of a stable 1W state in the interlayer for low-layer charge montmorillonite models with $\xi = 0.125$ and 0.0625. Chen et al. conducted comprehensive research investigating the influence of clay charge, ranging from 0.0625 to 0.375, utilizing varying numbers of Na ions in their MD simulations. In their simulation setup, the bottom layer of the structure remained fixed, while the top layer was permitted to attain equilibrium and move freely vertically, resulting in the natural swelling of the clay. In contrast to the idealized conditions of DFT calculations (simulation system at 0K, manual addition of water molecules in the structure, and adjustment of layer thickness), these MD simulations were executed at room temperature with elevated environmental water content. This departure from ideal conditions provides valuable insights into predicting the behavior of low-layer charge montmorillonite in a more natural environment. Despite methodological disparities, the outcomes from these simulations align with earlier DFT simulation findings by Emmerich et al. in 2018, contributing to an expanded understanding and prediction of the swelling behavior of low layer charge montmorillonite under diverse conditions (Chen et al., 2022).

Table 1.6 References of calculated basal spacing (d001) and number (H_2O/Na^+) or layer (dehydrated state 0W, mono-hydrated 1W, bi-hydrated 2W and tri-hydrated 3W) of water molecules of trans-vacant Na saturated montmorillonite by MD or Monte Carlo simulation (* indicates the supercell is placing in a simulation box full of water molecules).

Authors	ξ/FU	UC per SC	No. of Na^+	No. of Water	H_2O/Na^+	d001 (Å)	Program/Forcefield
Chen et al. (2022)	0.0625 0.125 0.1875 0.25 0.3125 0.375	16	2 4 6 8 10 12	1W 2W	*	12.75(1W) 12.75(1W) 12.72(1W), 15.48(2W) 12.69(1W), 15.29(2W) 12.65(1W), 15.16(2W) 12.57(1W), 15.03(2W)	LAMMPS/ CLAYFF (MD)
Peng et al. (2020)	0.375	32	24	0 (0W) 64 - 160 (1W) 240 - 320 (2W) 448 (3W)	0 2.6 - 6.6 10 - 13.3 18.6	9.4 12.3 15.4 18.3	NPT & NVT/CLAYFF (MD)
Qiu et al. (2020)	0.375 0.5 0.5625 0.6875	8	6 8 9 11	64	10.6 8 7.1 5.8	12.21 - 12.34 12.12 - 12.30 12.11 - 12.22 12.16 - 12.24	Forcite module of Material Studio 7.0/CLAYFF (MD)
Ho et al. (2019)	0.375	36	27	0W 0W - 1W 1W 1W - 2W 2W	*	9.85 10.95 12.55 13.25 15.13	LAMMPS/CLAYFF (MD)
Yang et al. (2017)	0.33	72	48	360 (1W) 720 (2W) 1080 (3W) 1440 (4W) 1800 (5W)	7.5 15 22.5 30 37.5	12.5 15.6 18.7 21.7 24.8	GROMACS/CLAFF (MD)

Seppäla et al. (2016)	0.25	2	1	0 - 32	0 - 32	11 - 19.5	LAMMPS/CLAYFF (MD)
	0.33	3	2	0 - 48	0 - 24		
	0.5	1	1	0 - 16	0 - 16		
Teich-McGoldrick et al. (2015)	0.375	40	30	0 - 560	0 - 18.6	9.5 - 18	LAMMPS (MD), GCMC (Monte Carlo)
				1W		12.17	
				2W		14.91	
Tao et al. (2010)	0.375	16	12	0 - 224	0 - 18.6	9.5 - 16.5	LAMMPS/CLAYFF (MD)
Cygan et al. (2004)	0.375	4	3	0 - 59	0 - 19.6	9.5 - 19	CLAYFF (MD)
Mary et al. (2002)	0.375	8	6	36 (1W)	6	12.3	Monte Carlo
				72 (2W)	12	15.3	
Chávez-Páez et al. (2001)	0.375	8	6	0	0 - 16	9.73, 9.99 - 10.39	MCY, TIP4P (Monte Carlo)
				8		10.50, 10.94 - 11.11	
				16		11.07, 11.86 - 11.95	
				24		11.86, 12.07 - 12.13	
				32		12.17, 12.47 - 12.50	
				40		12.42, 12.56 - 12.57	
				48		12.59, 13.09 - 13.17	
				56		14.38, 14.45 - 14.56	
				64		14.65, 14.87 - 14.88	
				72		15.80, 15.06 - 15.13	
				80		16.47, 15.43 - 15.56	
				88		17.50, 16.14 - 16.17	
				96		18.19, 16.87 - 17.11	

Boek et al. (1995) /Boek & Covenvy (1995)	0.375	8	6	0 4 8 12 16 24 32 40 48 72 96	0 - 16	10.17 10.45 10.52 11.21 11.64 12.20 12.32 12.64 13.13 15.30 17.07	Monte Carlo
Skipper et al. (1995)	0.375	8	6	0W 1W	*	9.96, 9.88 12.1, 11.7	MCY, TIP4P (Monte Carlo)
Skipper et al. (1995)	0.25 0.375	8	4 6	0, 32	0, 8 0, 5.33	9.19, 12.51 9.21, 11,94	Monte Carlo
Skipper et al. (1991)	0.5	8	8	0 64	0 8	9.8 14.2	Monte Carlo

References

Bergaya, F., & Lagaly, G. (2013). *Handbook of clay science*. Newnes.

Berghout, A., Tunega, D., & Zaoui, A. (2010). Density functional theory (DFT) study of the hydration steps of Na+/Mg2+/Ca2+/Sr2+/Ba2+-exchanged montmorillonites. *Clays and Clay Minerals*, *58*(2), 174–187.

Bisio, C., Gatti, G., Boccaleri, E., Marchese, L., Superti, G. B., Pastore, H. O., & Thommes, M. (2008). Understanding physico–chemical properties of saponite synthetic clays. *Microporous and Mesoporous Materials*, *107*(1–2), 90–101.

Boek, E. S., Coveney, P. V., & Skipper, N. T. (1995). Molecular modeling of clay hydration: A study of hysteresis loops in the swelling curves of sodium montmorillonites. *Langmuir*, *11*(12), 4629–4631.

Boek, E. S., & Sprik, M. (2003). Ab initio molecular dynamics study of the hydration of a sodium smectite clay. *The Journal of Physical Chemistry B*, *107*(14), 3251–3256.

Chatterjee, A., Iwasaki, T., Ebina, T., & Miyamoto, A. (1999). A DFT study on clay–cation–water interaction in montmorillonite and beidellite. *Computational Materials Science*, *14*(1–4), 119–124.

Chatterjee, A., Ebina, T., Onodera, Y., & Mizukami, F. (2004). Effect of exchangeable cation on the swelling property of 2: 1 dioctahedral smectite—A periodic first principle study. *The Journal of Chemical Physics*, *120*(7), 3414–3424.

Chávez-Páez, M., Van Workum, K., De Pablo, L., & de Pablo, J. J. (2001). Monte Carlo simulations of Wyoming sodium montmorillonite hydrates. *The Journal of Chemical Physics*, *114*(3), 1405–1413.

Chen, W. L., Grabowski, R. C., & Goel, S. (2022). Clay swelling: Role of cations in stabilizing/destabilizing mechanisms. *ACS Omega*, *7*(4), 3185–3191.

Christidis, G. E., Blum, A. E., & Eberl, D. D. (2006). Influence of layer charge and charge distribution of smectites on the flow behaviour and swelling of bentonites. *Applied Clay Science*, *34*(1–4), 125–138.

Cygan, R. T., Greathouse, J. A., Heinz, H., & Kalinichev, A. G. (2009). Molecular models and simulations of layered materials. *Journal of Materials Chemistry*, *19*(17), 2470–2481.

Decarreau, A. (1980). Cristallogenese expérimentale des smectites magnésiennes: Hectorite, stevensite. *Bulletin de Minéralogie*, *103*(6), 579–590.

Decarreau, A. (1985). Partitioning of divalent transition elements between octahedral sheets of trioctahedral smectites and water. *Geochimica et Cosmochimica Acta*, *49*(7), 1537–1544.

Delavernhe, L., Steudel, A., Darbha, G. K., Schäfer, T., Schuhmann, R., Wöll, C., Geckeis, H., & Emmerich, K. (2015). Influence of mineralogical and morphological properties on the cation exchange behavior of dioctahedral smectites. *Colloids and Surfaces A: Physicochemical and Engineering Aspects*, *481*, 591–599.

Delavernhe, L., Pilavtepe, M., & Emmerich, K. (2018). Cation exchange capacity of natural and synthetic hectorite. *Applied Clay Science*, *151*, 175–180.

Delhorme, M., Labbez, C., Caillet, C., & Thomas, F. (2010). Acid− base properties of 2: 1 clays. I. Modeling the role of electrostatics. *Langmuir*, *26*(12), 9240–9249.

Drits, V. A., Sakharov, B. A., Salyn, A. L., & Lindgreen, H. (2005). Determination of the content and distribution of fixed ammonium in illite-smectite using a modified X-ray diffraction technique: Application to oil source rocks of western Greenland. *American Mineralogist, 90*(1), 71–84.

Dultz, S., An, J.-H., & Riebe, B. (2012). Organic cation exchanged montmorillonite and vermiculite as adsorbents for Cr (VI): Effect of layer charge on adsorption properties. *Applied Clay Science, 67*, 125–133.

Eisenhour, D. D., & Brown, R. K. (2009). Bentonite and its impact on modern life. *Elements, 5*(2), 83–88.

Emmerich, K., Wolters, F., Kahr, G., & Lagaly, G. (2009). Clay profiling: The classification of montmorillonites. *Clays and Clay Minerals, 57*(1), 104–114.

Emmerich, K. (2013). Full Characterization of Smectites. In *Developments in Clay Science* (Vol. 5, pp. 381–404). Elsevier.

Emmerich, K., Koeniger, F., Kaden, H., & Thissen, P. (2015). Microscopic structure and properties of discrete water layer in Na-exchanged montmorillonite. *Journal of Colloid and Interface Science, 448*, 24–31.

Emmerich, K., Steudel, A., & Merz, D. (2017). Dehydroxylation of dioctahedral smectites in water vapor atmosphere. *Applied Clay Science*, *137*, 1–5.

Emmerich, K., Giraudo, N., Schuhmann, R., Schnetzer, F., Kaden, H., & Thissen, P. (2018). On the prediction of water contents in Na-saturated dioctahedral smectites. *The Journal of Physical Chemistry C, 122*(13), 7484–7493.

Ferrage, E., Lanson, B., Sakharov, B. A., & Drits, V. A. (2005). Investigation of smectite hydration properties by modeling experimental X-ray diffraction patterns: Part I. Montmorillonite hydration properties. *American Mineralogist, 90*(8–9), 1358–1374.

Ferrage, E. (2016). Investigation of the interlayer organization of water and ions in smectite from the combined use of diffraction experiments and molecular simulations. A review of methodology, applications, and perspectives. *Clays and Clay Minerals*, *64*(4), 348–373.

Fonseca, C. G., Vaiss, V. S., Wypych, F., Diniz, R., & Leitao, A. A. (2017). Structural and thermodynamic investigation of the hydration-dehydration process of Na+-Montmorillonite using DFT calculations. *Applied Clay Science*, *143*, 212–219.

Gaharwar, A. K., Cross, L. M., Peak, C. W., Gold, K., Carrow, J. K., Brokesh, A., & Singh, K. A. (2019). 2D nanoclay for biomedical applications: Regenerative medicine, therapeutic delivery, and additive manufacturing. *Advanced Materials*, *31*(23), 1900332.

Golubeva, O. Y. (2016). Effect of synthesis conditions on hydrothermal crystallization, textural characteristics and morphology of aluminum-magnesium montmorillonite. *Microporous and Mesoporous Materials*, *224*, 271–276.

Greathouse, J. A., & Cygan, R. T. (2013). Molecular simulation of clay minerals. In *Developments in Clay Science* (Vol. 5, pp. 405–423). Elsevier.

Guggenheim, S., Adams, J. M., Bain, D. C., Bergaya, F., Brigatti, M. F., Drits, V. A., Formoso, M. L., Galán, E., Kogure, T., & Stanjek, H. (2006). Summary of recommendations of nomenclature committees relevant to clay mineralogy: Report of the Association Internationale pour l'Etude des Argiles (AIPEA) Nomenclature Committee for 2006. *Clays and Clay Minerals*, *54*(6), 761–772.

Guggenheim, S., Adams, J. M., Bergaya, F., Brigatti, M. F., Drits, V. A., Formoso, M. L., Galán, E., Kogure, T., Stanjek, H., & Stucki, J. W. (2009). Nomenclature for stacking in phyllosilicates: Report of the Association Internationale pour l'Etude des Argiles (AIPEA) Nomenclature Committee for 2008. *Clay Minerals*, *44*(1), 157–159.

Guven, N. (1988). Smectites. *Hydrous Phyllosilicates (Exclusive Mica)*, 497–559.

Harder, H. (1972). The role of magnesium in the formation of smectite minerals. *Chemical Geology*, *10*(1), 31–39.

Harder, H. (1977). Clay mineral formation under lateritic weathering conditions. *Clay Minerals*, *12*(4), 281–288.

Hernández-Laguna, A., Escamilla-Roa, E., Timon, V., Dove, M. T., & Sainz-Díaz, C. I. (2006). DFT study of the cation arrangements in the octahedral and tetrahedral sheets of dioctahedral 2: 1 phyllosilicates. *Physics and Chemistry of Minerals*, *33*, 655–666.

Hickson, D. (1974). *Layered clay minerals, catalysts, and processes for using*. U.S. Patent No 3,844,979, 1974.

Hickson, D. (1975). *Layered clay minerals, catalysts, and processes for using*. U.S. Patent No 3,892,655, 1975.

Ho, T. A., Criscenti, L. J., & Greathouse, J. A. (2019). Revealing transition states during the hydration of clay minerals. *The Journal of Physical Chemistry Letters*, *10*(13), 3704–3709.

Jasmund, K., & Lagaly, G. (2013). *Tonminerale und Tone: Struktur, Eigenschaften, Anwendungen und Einsatz in Industrie und Umwelt*. Springer-Verlag.

Jensen, F. (2017). *Introduction to computational chemistry*. John wiley & sons.

Jlassi, K., Abidi, R., Benna, M., Chehimi, M. M., Kasak, P., & Krupa, I. (2018). Bentonite-decorated calix [4] arene: A new, promising hybrid material for heavy-metal removal. *Applied Clay Science*, *161*, 15–22.

Kaufhold, S., Hein, M., Dohrmann, R., & Ufer, K. (2012). Quantification of the mineralogical composition of clays using FTIR spectroscopy. *Vibrational Spectroscopy*, *59*, 29–39.

Kaufhold, S., KremLeva, A., Krüger, S., Rösch, N., Emmerich, K., & Dohrmann, R. (2017). Crystal-chemical composition of dicoctahedral smectites: An energy-based assessment of empirical relations. *ACS Earth and Space Chemistry*, *1*(10), 629–636.

Kloprogge, J. T., Breukelaar, J., Jansen, J. B. H., & Geus, J. W. (1993). Development of ammonium-saponites from gels with variable ammonium concentration and water content at low temperatures. *Clays and Clay Minerals*, *41*(1), 103–110.

Kloprogge, J. T., Komarneni, S., & Amonette, J. E. (1999). Synthesis of smectite clay minerals: A critical review. *Clays and Clay Minerals*, *47*, 529–554.

Lagaly, G. (1981). Characterization of clays by organic compounds. *Clay Minerals*, *16*(1), 1–21.

Lagaly, G. (1989). Principles of flow of kaolin and bentonite dispersions. *Applied Clay Science*, *4*(2), 105–123.

Lagaly, G. (1994). Bentonites: Adsorbents of toxic substances. *Surfactants and Colloids in the Environment*, 61–72.

Laird, D. A. (1996). Model for crystalline swelling of 2: 1 phyllosilicates. *Clays and Clay Minerals*, *44*, 553–559.

Laird, D. A. (1999). Layer change influences on the hydration of expandable 2:1 phyllosilicates. *Clays and Clay Minerals*, *47*(5), 630–636.

Laird, D. A. (2006). Influence of layer charge on swelling of smectites. *Applied Clay Science*, *34*(1–4), 74–87.

Lantenois, S., Champallier, R., Bény, J.-M., & Muller, F. (2008). Hydrothermal synthesis and characterization of dioctahedral smectites: A montmorillonites series. *Applied Clay Science*, *38*(3–4), 165–178.

Lavikainen, L. (2016). *The structure and surfaces of 2: 1 phyllosilicate clay minerals*. Itä-Suomen yliopisto.

Lee, J. G. (2016). *Computational materials science: An introduction*. CRC press.

Maes, A., & Cremers, A. (1977). Charge density effects in ion exchange. Part 1.—Heterovalent exchange equilibria. *Journal of the Chemical Society, Faraday Transactions 1: Physical Chemistry in Condensed Phases, 73*, 1807–1814.

Maes, A., & Cremers, A. (1978). Charge density effects in ion exchange. Part 2.—Homovalent exchange equilibria. *Journal of the Chemical Society, Faraday Transactions 1: Physical Chemistry in Condensed Phases, 74*, 1234–1241.

Marry, V., Turq, P., Cartailler, T., & Levesque, D. (2002). Microscopic simulation of structure and dynamics of water and counterions in a monohydrated montmorillonite. *The Journal of Chemical Physics, 117*(7), 3454–3463.

Meyer, S., Bennici, S., Vaulot, C., Rigolet, S., & Dzene, L. (2020). Influence of the Precursor and the Temperature of Synthesis on the Structure of Saponite. *Clays and Clay Minerals, 68*(6), 544–552.

Mering, J., & Oberlin, A. (1971). The Smectites. In J. A. Gard (Ed.), *The Electron-Optical Investigation of Clays* (Vol. 3, p. 0). Mineralogical Society of Great Britain and Ireland.

Mignon, P., Ugliengo, P., Sodupe, M., & Hernandez, E. R. (2010). Ab initio molecular dynamics study of the hydration of Li+, Na+ and K+ in a montmorillonite model. Influence of isomorphic substitution. *Physical Chemistry Chemical Physics*, *12*(3), 688–697.

Min, F., Wang, L., Chen, J., Liu, C., Ren, B., Zhang, L., & Zhu, Y. (2022). Molecular simulation in surface hydration of clay minerals: A review of theory and applications. *Miner. Miner. Mater.*, *1*, 3.

Neumann, B. S. (1966). UK Patent GB1213122. *Clays. Filing Date*, *12*.

Peng, C., Wang, G., Zhang, C., Qin, L., Zhu, X., & Luo, S. (2021). Molecular dynamics simulation of NH4+-smectite interlayer hydration: Influence of layer charge density and location. *Journal of Molecular Liquids, 336*, 116232.

Reinholdt, M., Miehé-Brendlé, J., Delmotte, L., Tuilier, M.-H., le Dred, R., Cortès, R., & Flank, A.-M. (2001). Fluorine route synthesis of montmorillonites containing Mg or Zn and characterization by XRD, thermal analysis, MAS NMR, and EXAFS spectroscopy. *European Journal of Inorganic Chemistry*, *2001*(11), 2831–2841.

Reinholdt, M., Miehe-Brendle, J., Delmotte, L., Le Dred, R., & Tuilier, M.-H. (2005). Synthesis and characterization of montmorillonite-type phyllosilicates in a fluoride medium. *Clay Minerals, 40*(2), 177–190.

Rotenberg, B., Marry, V., Salanne, M., Jardat, M., & Turq, P. (2014). Multiscale modelling of transport in clays from the molecular to the sample scale. *Comptes Rendus Geoscience, 346*(11–12), 298–306.

Sainz-Díaz, C. I., Escamilla-Roa, E., & Hernández-Laguna, A. (2005). Quantum mechanical calculations of trans-vacant and cis-vacant polymorphism in dioctahedral 2: 1 phyllosilicates. *American Mineralogist, 90*(11–12), 1827–1834.

Sato, T., Watanabe, T., & Otsuka, R. (1992). Effects of layer charge, charge location, and energy change on expansion properties of dioctahedral smectites. *Clays and Clay Minerals, 40*, 103–113.

Seppälä, A., Puhakka, E., & Olin, M. (2016). Effect of layer charge on the crystalline swelling of Na+, K+ and Ca2+ montmorillonites: DFT and molecular dynamics studies. *Clay Minerals, 51*(2), 197–211.

Shainberg, I., Alperovitch, N. I., & Keren, R. (1987). Charge density and Na-K-Ca exchange on smectites. *Clays and Clay Minerals, 35*(1), 68–73.

Shi, J., Liu, H., Meng, Y., Lou, Z., Zeng, Q., & Yang, M. (2013). First-principles study of ammonium ions and their hydration in montmorillonites. *Journal of Molecular Modeling, 19*, 1875–1881.

Schlick, T. (2010). *Molecular modeling and simulation: An interdisciplinary guide* (Vol. 2). Springer.

Sholl, D. S., & Steckel, J. A. (2022). *Density functional theory: A practical introduction*. John Wiley & Sons.

Skipper, N. T., Refson, K., & McConnell, J. D. C. (1991). Computer simulation of interlayer water in 2: 1 clays. *The Journal of Chemical Physics, 94*(11), 7434–7445.

Skipper, N. T., Chang, F.-R. C., & Sposito, G. (1995). Monte Carlo simulation of interlayer molecular structure in swelling clay minerals. 1. Methodology. *Clays and Clay Minerals, 43*, 285–293.

Skipper, N. T., Sposito, G., & Chang, F.-R. C. (1995). Monte Carlo simulation of interlayer molecular structure in swelling clay minerals. 2. Monolayer hydrates. *Clays and Clay Minerals, 43*, 294–303.

Slade, P. G., Quirk, J. P., & Norrish, K. (1991). Crystalline swelling of smectite samples in concentrated NaCl solutions in relation to layer charge. *Clays and Clay Minerals, 39*(3), 234–238.

Tambach, T. J., Bolhuis, P. G., Hensen, E. J., & Smit, B. (2006). Hysteresis in clay swelling induced by hydrogen bonding: Accurate prediction of swelling states. *Langmuir, 22*(3), 1223–1234.

Tao, L., Xiao-Feng, T., Yu, Z., & Tao, G. (2010). Swelling of K+, Na+ and Ca2+-montmorillonites and hydration of interlayer cations: A molecular dynamics simulation. *Chinese Physics B, 19*(10), 109101.

Tajeddine, L., Gailhanou, H., Blanc, P., Lassin, A., Gaboreau, S., & Vieillard, P. (2015). Hydration–dehydration behavior and thermodynamics of MX-80 montmorillonite studied using thermal analysis. *Thermochimica Acta*, *604*, 83–93.

Teich-McGoldrick, S. L., Greathouse, J. A., Jove-Colon, C. F., & Cygan, R. T. (2015). Swelling properties of montmorillonite and beidellite clay minerals from molecular simulation: Comparison of temperature, interlayer cation, and charge location effects. *The Journal of Physical Chemistry C*, *119*(36), 20880–20891.

Tombacz, E., & Szekeres, M. (2004). Colloidal behavior of aqueous montmorillonite suspensions: The specific role of pH in the presence of indifferent electrolytes. *Applied Clay Science*, *27*(1–2), 75–94.

Trujillano, R., Rico, E., Vicente, M. A., Rives, V., Sobrados, I., & Sanz, J. (2015). Saponites containing divalent transition metal cations in octahedral positions—Exploration of synthesis possibilities using microwave radiation and NMR characterization. *Applied Clay Science*, *115*, 24–29.

Tsipursky, S. I., & Drits, V. A. (1984). The distribution of octahedral cations in the 2: 1 layers of dioctahedral smectites studied by oblique-texture electron diffraction. *Clay Minerals*, *19*(2), 177–193.

Tunega, D., Goodman, B. A., Haberhauer, G., Reichenauer, T. G., Gerzabek, M. H., & Lischka, H. (2007). Ab initio calculations of relative stabilities of different structural arrangements in dioctahedral phyllosilicates. *Clays and Clay Minerals*, *55*(2), 220–232.

Turunen, M., Brotons-Gisbert, M., Dai, Y., Wang, Y., Scerri, E., Bonato, C., Jöns, K. D., Sun, Z., & Gerardot, B. D. (2022). Quantum photonics with layered 2D materials. *Nature Reviews Physics*, *4*(4), 219–236.

Vogels, R., Kerkhoffs, M., & Geus, J. W. (1995). Non-hydrothermal synthesis, characterisation and catalytic properties of saponite clays. In *Studies in Surface Science and Catalysis* (Vol. 91, pp. 1153–1161). Elsevier.

Voora, V. K., Al-Saidi, W. A., & Jordan, K. D. (2011). Density functional theory study of pyrophyllite and M-montmorillonites (M= Li, Na, K, Mg, and Ca): Role of dispersion interactions. *The Journal of Physical Chemistry A*, *115*(34), 9695–9703.

Wolters, F., Lagaly, G., Kahr, G., Nueeshch, R., & Emmerich, K. (2009). A comprehensive characterization of dioctahedral smectites. *Clays and Clay Minerals*, *57*(1), 115–133.

Yamada, H., Nakazawa, H., Yoshioka, K., & Fujita, T. (1991). Smectites in the montmorillonite-beidellite series. *Clay Minerals*, *26*(3), 359–369.

Yamada, H., & Nakazawa, H. (1993). Isothermal treatments of regularly interstratified montmorillonite-beidellite at hydrothermal conditions. *Clays and Clay Minerals*, *41*, 726–730.

Zhang, D., Zhou, C.-H., Lin, C.-X., Tong, D.-S., & Yu, W.-H. (2010). Synthesis of clay minerals. *Applied Clay Science*, *50*(1), 1–11.

Zhang, X., Yi, H., Zhao, Y., Min, F., & Song, S. (2016). Study on the differences of Na-and Ca-montmorillonites in crystalline swelling regime through molecular dynamics simulation. *Advanced Powder Technology*, *27*(2), 779–785.

Zheng, Y., Zaoui, A., & Shahrour, I. (2011). A theoretical study of swelling and shrinking of hydrated Wyoming montmorillonite. *Applied Clay Science*, *51*(1–2), 177–181.

2 Methods

Table 2.1 Techniques to characterize clay minerals

Experimental & Computational Methods		Sample Preparation	Information
Synthesis of Smectite	Hydrothermal Synthesis	Mixed starting hydrogel	Synthetic smectite
Smectite Model Simulation	Density Function Theory (DFT) Simulation	Model structure optimization	Potential energy, hydration state and Interlayer spacing
Mineralogy	X-Ray Diffraction Analysis (XRD)	Powder & texture sample	Qualitative and quantitative phase analysis
Morphology	Environmental Scanning Electron Microscopy (ESEM)/ Scanning Electron Microscope (SEM)	Powder (gold or platinum coating)	Morphology
	Atomic Force Microscopy (AFM)	Powder (spin coating)	Morphology, Thickness, Specific surface area
Chemical Composition	X-Ray Fluorescence Analysis (XRF)	Powder (molding pellet)	Chemical composition
	Inductively Coupled Plasma – Optical Emission Spectroscopy (ICP-OES)	Supernatant solutions	Soluble and / or exchanged cations
	Solid-State Nuclear Magnetic Resonance Spectroscopy (NMR)	Powder	Structural substitution or location of Al and F
Exchange Behavior & Interlayer Composition	Determination of Cation Exchange Capacity (CEC)	Cu- triethylenetetramine method	Cation exchange capacity
	Determination of Layer Charge (ξ)	Alkylammonium method	Layer charge

2.1 Synthesis of Smectite

2.1.1 Hydrothermal Synthesis

Hydrothermal synthesis, a widely adopted technique across scientific fields, replicates mineral formation in a specific high-temperature and high-pressure settings. The historical development of hydrothermal synthesis traces to the document of geologist Karl Emil von Schafhäutl in 1845, who successfully cultivated microscopic quartz crystals within a high-pressure pot (Schafhäutl, 1845). In the mid-19th century when De Sénarmont, introduced the concept in 1851. Initially employed in the field of geoscience, hydrothermal synthesis gained prominence as a method for creating silicate minerals (De Sénarmont,1851). By the turn of the 20th century, various minerals had been successfully synthesized using this technique.

Autoclaves serve as the primary vessels for crystallization, characterized by their robust construction, typically thick-walled cylinders with hermetic seals, capable of enduring high temperatures and pressures over extended durations. The material composing the autoclave must be chemically inert to the solvent utilized. Typically, stainless steel is employed for hydrothermal experiments, necessitating the use of protective container within the autoclave to prevent corrosion in its inner chamber. These containers, which can match the autoclave's shape and be installed internally (contact inserts), or occupy only a portion of the autoclave's interior as "floating" inserts, are crafted from materials such as ferrous carbonless iron, platinum, titanium, glass (or quartz), or PTFE (Teflon), contingent on the temperature and solution employed.

The synthesis procedure in Chapter 3 encompasses heating a mixture of starting hydrogel within a sealed environment maintained above 100 ℃. The pressure within this process primarily arises from the autogenous vapor pressure generated by heating the hydrogel within the container in the steel autoclave. This method aids in the crystallization of the hydrogel under supersaturated conditions. Generally, hydrothermal synthesis relies on aqueous solutions containing metal salts, oxides, or hydroxides as primary starting materials. The gel phases incorporate diverse sources of the constituent elements, often in the presence of mineralizing agents with fluoride. Despite its requirement for specialized equipment, this process is remarkably versatile, enabling the production of substantial quantities of smectite exhibiting diverse textural properties, morphologies, and particle sizes. Hydrothermal synthesis stands as a pivotal technique in material science, showcasing its effectiveness in crafting a range of advanced materials characterized by distinct and valuable properties.

Equipment

Steel autoclave Tech-TI0200 (Techinstro, India) with Teflon container (200 mL, Liner-PTFE0200, Techinstro, India), scale, weighing paper, centrifuge tube (50 mL), centrifuge (Heraeus Thermo Multifuge 3S-R, Germany), heating oven, fume hood suitable for handling hydrochloric acid, fluoride test paper (Macherey-Nagel, Germany).

Chemicals

Synthesis of Saponite:

Sodium silicate (p.a., Sigma-Aldrich, Germany), sodium hydroxide (1M, Carl Roth GmbH, Germany), magnesium acetate tetrahydrate (p.a., Sigma-Aldrich, Germany), aluminum acetate (99%, Alfra Aesar, Germany), hydrochloric Acid (1M, Sigma-Aldrich, Germany)

Synthesis of Montmorillonite:

Silicon dioxide (Aerosil 130, 99.8%, Evonik Industries, Germany), sodium acetate anhydrous (p.a., Sigma-Aldrich, Germany), magnesium acetate tetrahydrate (p.a., Sigma-Aldrich, Germany), aluminium oxide hydroxide (98%, Pural SB-1, Sasol, Germany), hydrofluoric acid (40%, Sigma-Aldrich, Germany)

2.1.2 Homoionic Exchange (Sr)

The preparation of homoionic Sr-exchanged samples followed the methodology outlined in Steudel and Emmerich' research. (Steudel & Emmerich, 2013). In summary, the process involved dispersing 11 g of air-dried material, with an approximate 10% water content (equivalent to 10 g of dry solid material, constituting a solid content of 4% by mass), in 250 mL of chloride salt solution contained within polyethylene (PE) bottles from Nalgene (VWR). The water content of air-dried samples was determined by oven-drying a sample aliquot at 200 ℃ for 24 h. The chloride solution concentrations were adjusted to provide cation amounts equivalent to 20 times the Cation Exchange Capacity (CEC) for each synthetic smectite. The salts utilized were of reagent grade, specifically pro analysis (p.a.).

$$\mathrm{m_{Salt}[g]} = \left(\frac{\mathrm{CEC[cmol(+)/kg]} \cdot \mathrm{m_{dried}[g]}}{100[\mathrm{g}] \cdot 1000 \cdot \mathrm{z}} \cdot \mathrm{x}\right) \cdot \mathrm{M_{Salt}}\left[\frac{\mathrm{g}}{\mathrm{mol}}\right]$$

with $\mathrm{m_{Salt}}$ = mass of salt in 250 mL solution; CEC = cation exchange capacity of the synthetic smectite; $\mathrm{m_{dried}}$ = mass of dry solid sample (T = 200 ℃); z = valence of the cation; x = x-fold of CEC; $\mathrm{M_{Salt}}$ = molecular mass of salt.

The samples underwent three consecutive exchange cycles with a chloride solution, each dispersion agitated for 24 h on a shaker. Subsequently, centrifugation at 4500 rpm for 10 min separated the clear supernatant, which was replaced with either fresh chloride solution for further reactions or deionized water to remove excess ions post-exchange treatment. After rinsing with deionized water, dialysis was carried out to eliminate chloride and surplus cations until conductivity dropped below 5 µS/cm. Following chloride removal, the exchanged samples were dried at 60 ℃, gently ground in an agate mill, and stored in a desiccator over a saturated solution of magnesium nitrate to attain equilibrium at a relative humidity of 53%.

Equipment

Shaking table, scale, weighing paper, centrifuge tube (50 mL), centrifuge (Heraeus Thermo Multifuge 3S-R, Germany), heating oven.

Chemicals

Strontium chloride (p.a., Sigma-Aldrich, Germany), synthetic smectite, Volclay, Calcigel, Secursol UHP, deionized water.

2.2 Density Function Theory Calculation

2.2.1 Structural Models

In montmorillonite structure, the building unit comprises a 2:1 layer with an octahedral sheet nestled between two tetrahedral sheets. Modeling Na saturated montmorillonite involves Na serving as the interlayer exchangeable cation, while the layer charge originates from the substitution of octahedral Al by Mg. All structures adopted cis vacant and trans vacant octahedral sheets with a C2 and C2/m symmetry respectively and were characterized by lattice parameters $a_0 = 5.18$ Å and $b_0 = 8.98$ Å . The relaxation of c0 was permitted for both anhydrous and hydrated structures, maintaining angles at 90° for simplicity. Additionally, within the cis-vacant structure, two variations were observed: CV1 and CV2, distinguished by the differing positions occupied by Mg in the octahedral sheet, with Mg positioned in the cis position for CV1 and in the trans position for CV2 (Tsipursky & Drits, 1984). Studying diverse stable states of the smectite model and their hydration progression involves seeking an optimal shape and volume for the unit cell. The primary alteration in cell volume during hydration primarily correlates with changes in the c vector. Numerous investigations into smectite mineral swelling have primarily focused on maintaining fixed a and b cell parameters while varying solely the c vector or basal spacing (d001), representing the perpendicular distance between layers as the z component of the c vector.

Natural smectites exhibit diverse layer charge distributions, where samples consist of 2:1 layers with varying layer charges. Quantum mechanics (QM) computations focusing on Na-saturated montmorillonites encompass a layer charge of 0.125 per formula unit (p.f.u.). The inclusion of a layer charge lower than 0.2 p.f.u. aims to bridge the existing definition gap between pyrophyllite ($\xi = 0$) and dioctahedral smectites ($0.2 \leq \xi \leq 0.6$). Calculations were conducted using supercells (SCs) comprising 4 unit cells (UCs) with substitution in the octahedral sheets.

2.2.2 Computational Simulation

In this study, total energy calculations and ground-state structure analyses were conducted utilizing Density Functional Theory (DFT) implemented in the Vienna ab initio simulation program (Kresse & Furthmüller, 1996). The electron-ion interaction was handled via the projector augmented wave method (Kresse & Joubert, 1999), while valence electron wave functions were expanded into plane waves up to a kinetic energy cutoff of 360 eV, which ensured converged structural parameters for bulk calculations. Brillouin zone sampling was achieved using a 1 × 1 × 1 Monkhorst–Pack k points mesh (Monkhorst & Pack, 1976). The generalized gradient approximation of Perdew–Burke–Ernzerhof (PBE) form was applied for the electronic exchange-correlation functional (Perdew et al., 1996). The DFT-D3 functional was selected for its reliability in describing structural and energetic aspects, particularly concerning hydrogen-bonded water molecules and van der Waals force interactions (Grimme et al., 2010, 2011).

The optimization of atomic coordinates and unit cell size/shape for bulk materials employed a conjugate gradient technique utilizing the total energy, Hellmann-Feynman forces on atoms, and stresses on the unit cell. Beyond the previously discussed parameters like k-point density and E_{cut}, convergence in clay minerals' calculations was contingent upon both the mineral layer's thickness and the water film's thickness between the layers. To ensure convergence, a range of calculations with various layer thicknesses was executed for each atomic configuration. The thermodynamic minimum was then established by solving the Birch−Murnaghan equation of state, offering insights into the system's stable equilibrium configuration. More detailed descriptions and formulas of DFT calculation are provided in Chapter 4.

2.3 Analytical Method

2.3.1 X-Ray Diffraction Analysis (XRD)

The mineralogical composition of both natural and synthesized clays was characterized by X-ray diffraction (XRD). This technique relies on the interaction of X-rays with the periodic arrangement of atoms in a crystal lattice. The resulting diffraction pattern follows Bragg's law (Bragg & Bragg, 1913): n = diffraction order; λ = wavelength of incident radiation (Å); d = lattice spacing; θ = diffraction angle (°)

$$n \cdot \lambda = 2 \cdot d \cdot \sin(\theta)$$

Measurements were conducted using a Bruker D8 Advance A25 diffractometer (Bruker Corporation, USA) equipped with a LYNXEYE XE detector. The instrument was operated with CuKα radiation (λ = 1.54 Å) generated at 40 kV and 35 mA. Two sample types were investigated: randomly oriented powders and textured specimens prepared under ambient humidity. For powder samples, scans covered the range 5 - 70° 2θ with a step size of 0.02° and a counting time of 3 s per step, while textured samples were analyzed between 2 - 35° 2θ using the same step size but a reduced counting time of 2 s per step. To minimize preferred orientation and enhance data quality, automatic air scatter mode, a divergence slit of 2.5°, and a rotating stage set at 15 rpm were employed.

Natural smectites exhibited a relatively large basal spacing, with d001 reflections typically observed between 12 - 14 Å. The distinction between dioctahedral and trioctahedral smectites was made using the d060 reflection, which appears in the range of 1.48 - 1.50 Å for dioctahedral and 1.52 - 1.53 Å for trioctahedral clays (Brindley & Brown, 1984; Moore & Reynolds, 1997). Phase identification was carried out with the Diffrac Plus Evaluation software (Bruker Corporation, USA) following the procedure of Brindley and Brown (1980). Quantitative phase analysis was subsequently performed using Profex (version 5.2.9; Doebelin & Kleeberg, 2015) based on the Rietveld refinement method. This mathematical approach iteratively adjusts crystallographic parameters, peak profile functions, and background contributions to minimize the difference between the experimental and calculated patterns until an optimal fit is achieved (Kleeberg & Bergmann, 2002).

Powder samples

Equipment

Sample holder, glass slide (2.5 cm x 10 cm), sand paper.

Description

The clay sample was gently added to the sample holder and lightly settled to fill the space. Excess material was removed by carefully pressing the powder with a glass slide, producing a smooth, level surface. To achieve a random particle orientation, the surface was lightly abraded with sand paper. Throughout the preparation, care was taken to avoid applying excessive pressure or creating any intentional texture on the powder. For quantifying the amorphous content within the powder samples, Zinc oxide (>99.6%, Merck, Germany) served as an internal standard and was weighed and mixed with powder samples at a weight percentage of 10%

Textured samples

Equipment

Glass slide (2.5 cm x 2.5 cm), ultrasonic processor (UP 200s, Dr. Hielscher GmbH), desiccator, heating oven.

Chemicals

Ethylene glycol (Sigma-Aldrich, Germany), deionized water.

Description

A small amount of clay sample (≈ 100 mg) was added to 5 mL of deionized water and subjected to ultrasonic treatment for 30 s, resulting in a uniform suspension. The suspension was then carefully deposited onto a glass slide using a plastic pipette and left to air-dry at room temperature. Characterization was performed on the sample in its air-dried form, as well as after heating up to 550 ℃ for 24 h to induce dehydration. For the ethylene glycol treatment, the dried sample was stored in a desiccator containing ethylene glycol at 60 ℃ for 3 d, and XRD measurements were performed immediately after removal from storage.

2.3.2 X-Ray Fluorescence Analysis (XRF)

The chemical composition of the synthetic clays was determined by X-ray fluorescence (XRF) spectroscopy, which represents a key parameter for estimating layer charge. Results from quantitative XRD analysis, derived from the stoichiometric proportions of identified phases, were compared with the measured XRF data to validate compositional consistency. This comparison enabled the calculation of structural formulas for the clay minerals and contributed to a deeper understanding of their chemical variability and related properties.

XRF operates by recording the characteristic secondary radiation emitted after excitation with primary X-rays. Each element produces fluorescence at specific wavelengths, reflecting its atomic number, and the relative intensities of these emissions allow quantitative determination of elemental abundances. The measurable concentration range varies across elements, spanning from 0.0001 to 100%. For this study, analyses were conducted using an Axios spectrometer (Malvern Panalytical, Netherlands) equipped with a 2.4 kW rhodium X-ray tube. Powdered samples were fused with lithium tetraborate at a 1:14 ratio prior to measurement. Loss on ignition was assessed separately by heating subsamples at 1000 ℃ for 2 h.

2.3.3 Scanning Electron Microscopy (SEM)

Scanning and environmental electron microscopy (SEM/ESEM) were applied to study the morphology and surface features of natural and synthetic clay smectites. In these methods, a focused electron beam interacts with the sample surface, generating two-dimensional images from secondary and backscattered electrons, photons, and characteristic X-rays. With an attached energy-dispersive X-ray spectroscopy (EDX) detector, elemental composition of selected sample areas was also examined in a semi-quantitative manner.

For analysis, about 2 - 3 mg/cm^2 of powdered material was mounted on sample holders. To avoid charging, a conductive coating was applied: platinum (≈ 5 nm) for trioctahedral smectite and gold (≈ 7 nm) for dioctahedral smectite. Morphology of natural and synthetic trioctahedral smectites was examined with a Philips XL 30 environmental SEM (Thermo Fisher Scientific Inc., USA) operated in low-vacuum mode at 15 - 20 kV using a secondary electron detector. Synthetic dioctahedral smectites were analyzed with a Zeiss Auriga 60 field-emission SEM (Carl Zeiss AG, Germany) at 5 - 10 kV using an In-lens detector. Elemental composition of selected regions was checked with an EDAX EDX system to complement the morphological data.

2.3.4 Atomic Force Microscopy (AFM)

Atomic force microscopy (AFM), utilizing a Bruker dimension 3100 instrument equipped with a Nanoscope IV controller (Bruker Corporation, USA), was employed to assess the morphological characteristics of fundamental particles. This technique operates in contact mode under ambient conditions, where a nanoscale needle is engaged against the sample surface by a cantilever spring, and the resulting bending of the spring is measured optically. AFM images were analyzed and processed using the Scanning Probe Image Processing software (SPIP) developed by Image Metrology.

Particle size characterization

AFM was used for determination of the size of particles (according to the procedure from Delavernhe et al., 2015). Dispersions of 50 mg/L in ethanol (99.9%, Sigma-Aldrich, Germany) after 15 m of ultrasonic treatment (37 kHz) were deposited by spin coating onto a fresh and clean silicon wafer to ensure a good dispersion onto the surface. The images of smectite samples were analyzed using the Scanning Probe software to measure the thickness (h), basal area (A), and perimeter (P) of each particle. The weighted mean values were calculated to consider the particle size distribution with the recorded parameter of the particle i (x_i) as follows:

$$\bar{x} = \sum x_i \times m_i / m_t$$

The mass of the particle i (m_i) and the sum of the masses of all analyzed particles (m_t) can be calculated by the specific density (ρ_s), thickness and basal area of the particles.

$$m_i = \rho_s \times h_i \times A_i$$

$$m_t = \rho_s \sum h_i \times A_i$$

When single particles have the same thickness, the formula was written with the basal area of the particle i (A_i) and the sum of the basal areas of all analyzed particles (A_t) as below:

$$\bar{x} = \sum x_i \times A_i/A_t$$

To calculate the specific edge surface area ($a_{\mathrm{s,edge}}$ in $\mathrm{m^2/g}$) and the specific basal surface area ($a_{\mathrm{s,basal}}$ in $\mathrm{m^2/g}$) of single particles were calculated based on the area ratio of perimeter/basal ($R_{\mathrm{P/A}}$ in $\mathrm{nm^{-1}}$), thickness (h = 0.96 nm) and specific density (ρ_s = 2700 $\mathrm{kg/m^3}$).

$$a_{\mathrm{s,edge}} = R_{\mathrm{P/A}}/\rho_s \times 10^6$$

$$a_{\mathrm{s,basal}} = 2/(\rho_s \times h) \times 10^6$$

2.3.5 Solid-State Nuclear Magnetic Resonance Spectroscopy (NMR)

The ^{27}Al MAS NMR and ^{19}F MAS NMR spectra were recorded with a Bruker Avance II 400 MHz spectrometer (Bruker Corporation, USA) operating at B_0 = 9.4 Tesla (^{27}Al Larmor frequency of 104.23 MHz), equipped with a Bruker 2.5 mm double channels probe. All ^{27}Al experiments were carried out at room temperature with a π/12 radio frequency pulse length of 0.5 µs, a recycle delay of 1 s, at a spinning frequency of 30 kHz. The chemical shifts were referred to external $[\mathrm{Al(H_2O)_6}]^{3+}$ in $\mathrm{AlCl_3}$ aqueous solution. The decompositions of the spectra were performed using the DMFit software (Massiot et al., 2002). For ^{19}F MAS NMR, typical acquisition parameters included 4 µs corresponding to a flip angle of π/2 pulse and 30 s recycle delay. The chemical shifts were referred to $\mathrm{CFCl_3}$ standard reference.

2.3.6 Layer Charge Measurement

The mean value and density of the layer charge in smectite can determine its various properties, which can influence different applications. Nowadays there are several methods for determining the layer charge of smectites. Alkylammonium method (Lagaly, 1981), in which alkylammonium ions with different alkyl chain lengths (n_c = 4 - 18) are used to exchange the smectite interlayer cations and intercalate, so the interlayer spacing will expand with increasing chain length of the alkylammonium ion. The shift of the d001 due to the expanding of the basal spacing can be observed by XRD analysis.

For The distribution of the layer charge in smectites is mostly heterogeneous from layer to layer. Due to the different cation densities in the different interlayers, the relationship between increasing interlayer space and the transition from a monolayer to a bilayer can therefore be used to calculate and estimate the mean layer charge and the charge distribution of the interlayer. The alkylammonium method provides a reliable method for characterizing the charge density distribution of smectites. Alkylammonium ions with shorter alkyl chains form a monolayer (13.6 Å) and longer chains arrange themselves into a bilayer (17.7 Å) in the interlayer of smectites. With increasing numbers of alkyl chains, pseudotrimolecular layers (21.7 Å) and even paraffin-like layers can be observed in some higher charged clay minerals such as vermiculites. The arrangement of alkylammonium ions in the interlayer depends on its chain length and the layer charge, which can also be represented by the interlayer cation density or the packing density of the alkylammonium ions. Base on the formulas of the equivalent area available for a monolayer structure in the interlayer space: $A_e = a_0 b_0 \ / \ 2\xi$ ($a_0 b_0$ of dioctahedral and trioctahedral smectite: 46.5, 49.2 Å^2) and the area for the monolayer/bilayer transition of the alkylammonium ion: $A_c = 5.7 \times n_c + 14$. The transition from a monolayer to a bilayer occurs when the area occupied by the flat-lying alkylammonium ion (A_c) exceeds the equivalent area (A_e) available, and the layer charge can be calculated from the ratio $a_0 b_0 \ / \ 2A_c = \xi$. Following the above calculation, the measurement limit of this method also can be estimatied using the alkylammonium ion with the longest chain length (n_c = 18).

The complete AAM characterization process for each clay sample requires more than 14 alkylammonium ions with different chain lengths. Although reliable results can be obtained with this method, it is still time consuming for a large number of clay samples. Olis proposed a rapid estimation model based on the AAM method. Simple linear regression models are used to describe the relationship between the mean layer charges and the d-spacing, using only two different alkylammonium ions (n_c = 12, 18) to exchange the interlayer cation (Olis et al., 1990).

Equipment

Chemical glass bottle, glass slide, desiccator, centrifuge tube (10 mL), centrifuge (Heraeus Thermo Multifuge 3S-R, Germany), drying oven, X-ray D8 Advance A25 diffractometer (Bruker Corporation, USA).

Chemicals

Synthetic smectites, alkylamine (chain lengths n_c = 4 - 18, for synthesis, Sigma-Aldrich or Fulka Germany), formic acid (85%, Sigma-Aldrich, Germany), ethanol (99.5%, Sigma-Aldrich, Germany), phosphorus pentoxide (p.a., Sigma-Aldrich, Germany).

Alkylammonium Solution Preparation & Procedure

The production of the alkylammonium solution follows the standard procedure of Lagaly (Lagaly, 1994). Alkylammonium formates with different chain lengths are produced from alkylamines. The reason why alkylammonium formate solutions are chosen is because of their good solubility when longer chain alkylamine dissolves with formic acid ($n_c \geq 14$).

For example, 0.1 M octadecylammonium solution is prepared by 2.70 g octadecylamine dissolved in 10 mL ethanol. The solution of long-chain alkylamine (n_c > 12) must be prepared in 50 - 60 °C warm water bed. To product the formates, 0.5 g formic acid (≈ 0.01 mol) is added to the solutions and left in the fume hood for 2 h, then filled up to a final volume of 100 mL with deionized water. The pH value of the final solution should remain in the range of 5 - 6.5

and can be adjusted with formic acid. After each experiment, the remaining alkylammonium solutions should be stored in the oven 60 ℃ and the bottle should remain unsealed.

To ensure the result of the cation exchange process, the lowest amount of alkylammonium ion salts is three times the CEC (in the normal CEC range ≈ 100 cmol(+)/kg). 100 mg of the low charged clay sample (≈ 50 cmol(+)/kg) were reacted with 3 mL of 0.1 M alkylammonium solution in centrifuge tubes. The same amount of 3 mL was also required for solutions of different concentrations. The mixed sample must be stored in an oven of 60 ℃ and the reaction time is 2 - 3 days. After the reaction, the solid is separated by centrifugation (10 min, 4500 rpm), and washed with ethanol, again dispersed in fresh alkylammonium solution, and stored under the same conditions. The clay samples are washed free from the excess alkylammonium formates with pure ethanol (16 times for a complete washing cycle). After the final centrifugation, the structured samples are prepared by dispersing the clay with the internal standard in 3 mL ethanol and then slowly dripping the dispersion solution onto the glass slide. The desiccator with phosphorus pentoxide is used to dry the textured samples at room temperature and relatively low humidity before the XRD analysis. The parameters of XRD will be 2 - 12° 2θ with a step size of 0.04° 2θ/8s.

2.3.7 Cation Exchange Capacity Measurement

The cation exchange capacity (CEC) determination for synthetic samples followed the copper triethylenetetramine method (Meier & Kahr, 1999). Initially, 0.01 M copper triethylenetetramine (Cu-trien) solution was prepared by mixing the 100 mL 0.1 M copper sulfate pentahydrate solution and 1.465 g of 97% triethylenetetramine purum, then filled up to a final volume of 2 L with millipore water. 50 mg of synthetic and natural samples (Volclay, Calcigel, and Laponite are standard with known CEC values of 85, 63, 79 cmol(+)/kg, respectively) were combined with 10 mL of deionized water and 5 mL of 0.01 M Cu-trien solution within a 15 mL centrifuge tube. For samples with CEC values less than 50 cmol(+)/kg, an increased material amount of 100 - 200 mg was required. To calculate concentration of Cu-trien in clay samples, a calibration curve was established by mixing 10 mL of deionized water with various Cu-trien solution volumes (ranging from 0.5 to 5 mL), and these were measured accordingly. Following agitation and subsequent shaking on a table for 3 h to ensure homogeneity, the sample underwent centrifugation at 4500 rpm for 10 min using a Heraeus Thermo Multifuge 3S-R. Measurement of supernatant absorbance at 580 nm wavelength was conducted using a UV-Vis spectrophotometer employing disposable 1 cm path length polystyrene microcuvettes. The CEC (in cmol(+)/kg) was determined by quantifying color fade in the supernatant resulting from the exchange of interlayer cations via the Cu-trien solution.

For ICP-OES measurements, 5 mL of the solution from CEC experiment were diluted in the 1:1 ratio by 5 mL deionized water and acidified with 0.25 mL 1 M HNO_3. Then the concentration of cations (in mg/L) which were exchanged (e.g., Na^+, K^+, Ca^{2+}, Mg^{2+}) were determined by ICP-OES. A recalculate and verification of the measured CEC can be done according to the total amount of exchanged cations.

Equipment

Scale, weighing glasses, desiccator, centrifuge tube (50 mL), shaking table, polystyrene micro-cuvettes (1 cm path length, Lab Logistics Groups GmbH), centrifuge (Heraeus Thermo Multifuge 3S-R, Germany), UV-Vis Spectrometer Genesys 10 (Thermo Fischer Scientific Inc., USA)

Chemicals

Copper sulfate pentahydrate (0.1M, Sigma-Aldrich, Germany), triethylenetetramine purum (97%, Carl Roth GmbH, Germany), millipore water.

2.3.8 Inductively Coupled Plasma - Optical Emission Spectroscopy (ICP-OES)

ICP-OES was employed to determine the concentrations of exchanged cations in the supernatant solution. In this technique, the solution is first vaporized to form an aerosol and introduced into an argon plasma, where temperatures reach up to 7000 K. At such high temperatures, the elements become ionized and excited, emitting characteristic light at specific wavelengths, which can then be accurately measured for quantitative analysis.

The experiment utilized an ICP-OES Optima 8300DV instrument (PerkinElmer, USA). Solution samples obtained from CEC experiments underwent acidification by 1M HNO_3 solution to keep the elemental compounds of interest in solution and dilution by deionized water to fit within specific measuring range, depending on the concentration of elements in the solution. Analysis of the main exchanged cations such as Na^+, K^+, Ca^{2+}, Mg^{2+} provided insights into the interlayer cation types and their relative ratios. Assessing the total exchanged cations verified the measured cation exchange capacity.

Table 2.2 Characteristic wavelengths of main analyzed cations.

Cation	**Na^+**	**K^+**	**Mg^{2+}**	**Ca^{2+}**	**Al^{3+}**	**Si^{4+}**
Wavelength (nm)	589.52	766.49	279.55	396.84	396.15	251.61

References

Alduchov, O. A., & Eskridge, R. E. (1996). Improved Magnus form approximation of saturation vapor pressure. *Journal of Applied Meteorology and Climatology*, *35*(4), 601–609.

Bragg, W. H., & Bragg, W. L. (1913). The reflection of X-rays by crystals. *Proceedings of the Royal Society of London. Series A, Containing Papers of a Mathematical and Physical Character, 88*(605), 428–438

Brindley, G.W. & Brown, G. (1984). Crystal structures of clay minerals and their X-Ray identifikation. *Mineralogical Society Monograph No. 5,* 41 Queen's Gate, London SW7 5HR.

Brown, G., & Brindley, G. W. (1980). X-ray Diffraction Procedures for Clay Mineral Identification. In G. W. Brindley & G. Brown (Eds.), *Crystal Structures of Clay Minerals and their X-Ray Identification* (Vol. 5, p. 0). Mineralogical Society of Great Britain and Ireland.

Brunauer, S., Emmett, P. H., & Teller, E. (1938). Adsorption of gases in multimolecular layers. *Journal of the American Chemical Society, 60*(2), 309–319.

De Sénarmont, H. (1851). Experience sur la formation des mineraux par voie humide dans lea gites metalliferes coneretionnes. *Annales de Chimie et Physique, Troisième Séries,* 129–175.

Delavernhe, L., Steudel, A., Darbha, G. K., Schäfer, T., Schuhmann, R., Wöll, C., Geckeis, H., & Emmerich, K. (2015). Influence of mineralogical and morphological properties on the cation exchange behavior of dioctahedral smectites. *Colloids and Surfaces A: Physicochemical and Engineering Aspects*, *481*, 591–599.

Doebelin, N., & Kleeberg, R. (2015). Profex: a graphical user interface for the Rietveld refinement program BGMN. *Journal of applied crystallography, 48(5),* 1573-1580.

Grimme, S. (2011). Density functional theory with London dispersion corrections. *Wiley Interdisciplinary Reviews: Computational Molecular Science, 1*(2), 211–228.

Grimme, S., Antony, J., Ehrlich, S., & Krieg, H. (2010). A consistent and accurate ab initio parametrization of density functional dispersion correction (DFT-D) for the 94 elements H-Pu. *The Journal of Chemical Physics*, *132*(15).

Grimme, S., Ehrlich, S., & Goerigk, L. (2011). Effect of the damping function in dispersion corrected density functional theory. *Journal of Computational Chemistry*, *32*(7), 1456–1465.

Kleeberg, R., Bergmann, J., SenGupta, S. P., & Chatterjee, P. (2002). Quantitative phase analysis using the Rietveld method and a fundamental parameter approach. *Proceedings of the II International School on Powder Diffraction*, 63–76.

Kresse, G., & Furthmüller, J. (1996). Efficiency of ab-initio total energy calculations for metals and semiconductors using a plane-wave basis set. *Computational Materials Science*, *6*(1), 15–50.

Kresse, G., & Joubert, D. (1999). From ultrasoft pseudopotentials to the projector augmented-wave method. *Physical Review b, 59*(3), 1758.

Lagaly, G. (1981). Characterization of clays by organic compounds. *Clay Minerals, 16*(1), 1–21.

Lagaly, G. (1994). Bentonites: Adsorbents of toxic substances. *Surfactants and Colloids in the Environment*, 61–72.

Massiot, D., Fayon, F., Capron, M., King, I., Le Calvé, S., Alonso, B., Durand, J.-O., Bujoli, B., Gan, Z., & Hoatson, G. (2002). Modelling one-and two-dimensional solid-state NMR spectra. *Magnetic Resonance in Chemistry, 40*(1), 70–76.

Meier, L. P., & Kahr, G. (1999). Determination of the Cation Exchange Capacity (CEC) of Clay Minerals Using the Complexes of Copper (II) Ion with Triethylenetetramine and Tetraethylenepentamine. *Clays and Clay Minerals, 47*(3), 386–388.

Monkhorst, H. J., & Pack, J. D. (1976). Special points for Brillouin-zone integrations. *Physical Review B, 13*(12), 5188.

Moore, D. M., & Reynolds Jr, R. C. (1989). *X-ray Diffraction and the Identification and Analysis of Clay Minerals.* Oxford University Press (OUP).

Olis, A. C., Malla, P. B., & Douglas, L. A. (1990). The rapid estimation of the layer charges of 2: 1 expanding clays from a single alkylammonium ion expansion. *Clay Minerals, 25*(1), 39–50.

Perdew, J. P., Chevary, J. A., Vosko, S. H., Jackson, K. A., Pederson, M. R., Singh, D. J., & Fiolhais, C. (1992). Atoms, molecules, solids, and surfaces: Applications of the generalized gradient approximation for exchange and correlation. *Physical Review B, 46*(11), 6671.

Perdew, J. P., Burke, K., & Ernzerhof, M. (1996). Generalized gradient approximation made simple. *Physical Review Letters, 77*(18), 3865.

Plaschke, M., Schäfer, T., Bundschuh, T., Ngo Manh, T., Knopp, R., Geckeis, H., & Kim, J. I. (2001). Size characterization of bentonite colloids by different methods. *Analytical Chemistry, 73*(17), 4338–4347.

Schafhäutl, K. F. E. (1845). Gelehrte Anzeigen Bayer. *Akad, 20,* 557–561.

Steudel, A., & Emmerich, K. (2013). Strategies for the successful preparation of homoionic smectites. *Applied Clay Science, 75,* 13–21.

Tsipursky, S. I., & Drits, V. A. (1984). The distribution of octahedral cations in the 2: 1 layers of dioctahedral smectites studied by oblique-texture electron diffraction. *Clay Minerals, 19*(2), 177–193.

3 Synthesis of Low Charge Trioctahedral and Dioctahedral Smectites

3.1 Introduction

The potential uses of smectite have discussed for a period of time. The potential application of the smectite material are not only the field of medicine, catalysis, biochemistry, and polymer-inorganic nanocomposites, but also on the research area of various quantum technologies (Karnland et al., 2006; Eisenhour & Brown, 2009; Jasmund & Lagaly, 2013). The quality requirement of smectite material have arisen research for ways to obtain synthetic smectite with specific characteristics, such as layer charge, chemical composition, particle size, and cation exchange capacity (Decarreu et al., 2008; Lantenois et al., 2008; Le Forestier et al., 2010; Golubeva, 2016; Delavernhe et al., 2018). While prior research extensively explored hydrothermal synthesis of smectite, there was a still definition gap regarding the synthesis and determination of low layer charge smectite in existing literature. Closing this gap in understanding low layer charge smectite becomes important, necessitating the synthesis of both dioctahedral and trioctahedral smectites with a layer charge $\xi < 0.2$. This pursuit holds the key to investigating properties associated with low layer charge and serves as a crucial prerequisite for refining layer charge measurement methodologies.

The experimental conditions outlined in literature emphasizes the requirement for high temperatures with autogenous pressure, and precise reaction durations to attain increased purity and crystallinity within a reasonable timeframe when synthesizing synthetic smectite. Additionally, the adding order, selection and nature of the initial reagents within the reaction medium significantly influence the synthesis process (Jaber & Miehé-Brendlé, 2005, 2008; de Oliveira et al., 2021). To generate low layer charge smectite, the synthesis methodology involved utilizing mixed hydrogels with specific compositions as initial reagents. These hydrogels were created using Si source chemicals (Na_2SiO_3, SiO_2), various metal salts (Na, Mg, Al), and mineralizers (HF or NaF) dissolved in deionized water. The hydrogel compositions were structured based on the theoretical formulation of smectite:

Saponite (trioctahedral structure): $M^{n+}_{x/n}\,[Mg_3(Si_{4-x}\,Al_x)O_{10}(OH, F)_2]\cdot nH_2O$

Montmorillonite (dioctahedral structure): $M^{n+}_{x/n}\,[(Al_{2-x}\,Mg_x)Si_4O_{10}(OH, F)_2]\cdot nH_2O$

where M indicates the interlayer cation. The parameter x/n was adjusted within the range of 0.1, 0.125, and 0.18 per formula unit, showcasing distinct degrees of isomorphous substitution within the octahedral or tetrahedral sheets.

The objectives of this study encompass the synthesis of dioctahedral and trioctahedral low layer charged smectites, aiming for specific layer charge values $\xi = 0.1$, 0.125, and 0.18, adjustable through variations in the starting material compositions. This experimental investigation aims to ascertain the influence of synthesis parameters on critical characteristics, including crystallinity, particle size, surface area, cation exchange capacity, and aims to contribute to the advancement of techniques for measuring layer charge in future studies.

3.2 Materials and Methodology

3.2.1 Chemicals

For the synthesis of dioctahedral smectite, the selection of starting materials is limited based on previous studies (Reinholdt et al., 2001, 2005). It includes silicon oxide (Aerosil 130, 99.8%, Evonik Industries, Germany), sodium acetate anhydrous (p.a., Sigma-Aldrich, Germany), magnesium acetate tetrahydrate (p.a., Sigma-Aldrich, Ger-many), aluminium oxide hydroxide (98%, Pural SB-1, Sasol, Germany), hydrofluoric acid (40%, Sigma-Aldrich, Germany). The synthesis of trioctahedral smectite using sodium silicate (p.a., Sigma-Aldrich, Germany), sodium hydroxide (1M, Carl Roth GmbH, Germany), magnesium acetate tetrahydrate (p.a., Sigma-Aldrich, Germany), aluminum acetate (99%, Alfra Aesar, Germany), hydrochloric Acid (1M, Sigma-Aldrich, Germany) as the starting materials and all chemicals were used without any previous purification.

3.2.2 Starting Material Pre-treatment

In the synthesis of trioctahedral smectite, prior to mixing the starting materials, it is crucial to remove excess Na originating from sodium silicate (p.a., Sigma-Aldrich, Germany), which involving the use of sodium silicate and hydrochloric acid (1M, Sigma-Aldrich, Germany), without requiring additional purification steps (Figure 3.1). The direct mixing technique was employed to facilitate a simple and efficient process suitable for large-scale production. (Joni et al. 2020) Sodium silicate was mixed with approximately 100 mL of deionized water and stirred for 3 h. Subsequently, hydrochloric acid was added at room temperature until a gel-like silicon dioxide solution, referred to as the "gel type," was obtained. To eliminate excess chloride ions, the samples were subjected to repeated washing (12 - 13 times) using centrifugation (Heraeus Thermo Multifuge 3S-R) at 4500 rpm for 10 min with deionized water. The absence of chloride ions was confirmed by testing the product with silver nitrate (0.1 M, Sigma-Aldrich, Germany) solution.

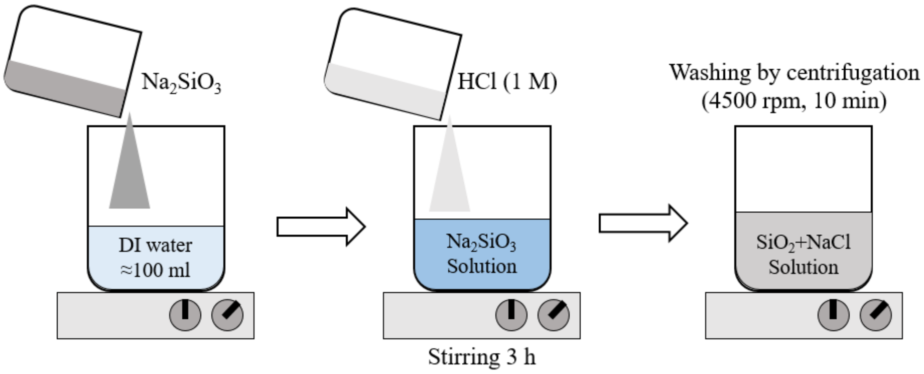

Figure 3.1 The process of the synthesis of silica particles by precipitation method.

3.2.3 Hydrothermal Synthesis

The general procedure and brief development of hydrothermal synthesis are mentioned in chapter 2.1.1. The synthesis process involved the utilization of mixed hydrogels with compositions modified to match the theoretical formulae of saponite and montmorillonite, specifically targeting layer charge $\xi = 0.18$, 0.125, and 0.1 in the synthetic products. The synthesis of dioctahedral and trioctahedral smectite involves the calculation of the starting hydrogel compositions based on the theoretical formula of montmorillonite and saponite. The formula for montmorillonite is $Na_x[(Al_2Mg_{2-x})Si_4O_{10}(OH)_2]\cdot nH_2O$, while the formula for saponite is $Na_x[Mg_3(Si_{4-x}Al_x)O_{10}(OH)_2]\cdot nH_2O$, where x ranges from 0.18, 0.125, and 0.1, representing the value of layer charge (Table 3.1).

Table 3.1 List of synthetic smectites and theoretical formulas.

Sample Name*	**Layer Charge ξ**	**Theoretical Formula**
S0.1	0.1	$Na_{0.1}[Mg_3(Si_{3.9}Al_{0.1})O_{10}(OH)_2]\cdot nH_2O$
S0.125	0.125	$Na_{0.125}[Mg_3(Si_{3.875}Al_{0.125})O_{10}(OH)_2]\cdot nH_2O$
S0.18	0.18	$Na_{0.18}[Mg_3(Si_{3.82}Al_{0.18})O_{10}(OH)_2]\cdot nH_2O$
M0.1	0.1	$Na_{0.1}[(Al_{1.9}Mg_{0.1})Si_4O_{10}(OH)_2]\cdot nH_2O$
M0.125	0.125	$Na_{0.125}[(Al_{1.875}Mg_{0.125})Si_4O_{10}(OH)_2]\cdot nH_2O$
M0.18	0.18	$Na_{0.18}[(Al_{1.82}Mg_{0.18})Si_4O_{10}(OH)_2]\cdot nH_2O$

*) S: Synthetic Saponite, M: Synthetic Montmorillonite

For the hydrothermal synthesis of trioctahedral and dioctahedral smectite, different synthesis conditions and Si- or metal-source chemicals as starting materials are recorded (Table 3.2). In the case of trioctahedral smectite synthesis, the procedure began with the preparation of hydrogels by mixing all starting materials with deionized water, maintaining constant stirring to avoid any precipitation. The fully mixed hydrogel was aged for 2 h at room temperature, with an initial pH range close to neutral (5 - 7). Subsequently, hydrothermal treatment was conducted at 200 ℃ for 72 h under autogenous water pressure in Teflon-lined stainless steel autoclaves. Following crystallization, the resulting products were separated and thoroughly washed via centrifugation with deionized water, then dried at 60 ℃ for 12 h. The dried synthetic samples were further ground into fine powder and subjected to controlled humidity conditions.

The synthesis of dioctahedral smectite required more restrictive conditions, following the procedure described previously (Reinholdt et al., 2001, 2005). The synthesis medium was acidic, with the presence of fluoride, as the crystallization of pure montmorillonite necessitated small amounts of F (acting as a mineralizer). Specific types of chemicals were chosen, and the content of hydrofluoric acid and silicon oxide was kept constant ($F/SiO_2 = 0.05$), with a weak acidic initial pH value of 4.5 - 5.5 after the aging process. The starting materials were mixed with constant stirring in the following order: deionized water, hydrofluoric acid, sodium acetate, magnesium acetate, boehmite, and silicon dioxide. The subsequent procedure for hydrothermal synthesis and sample treatment followed the same conditions as for the trioctahedral smectite synthesis, except that the synthesis temperature was increased to 220 ℃, and two different synthesis durations were added: 120 and 168 h.

Table 3.2 Chemical list for preparing the starting hydrogels.

Synthesis of Trioctahedral Smectite					
Time/℃: 72 h/200 ℃, **Ideal Mole:** 0.02 mole **DI Water:** 140 mL, **Fill Rate of Container:** 70%					
Sample Name	**Si source**	**Na source**	**Mg source**	**Al source**	**Mineralizer**
	Na_2SiO_3* (g)	1M NaOH (mL)	$Mg(CH_3COO)_2 \cdot 4H_2O$ (g)	$Al(CH_3COO)_2OH$ (g)	X
S0.1	9.52	1.98	12.87	0.32	
S0.125	9.46	2.50	12.87	0.40	
S0.18	9.32	3.58	12.87	0.58	
Synthesis of Dioctahedral Smectite					
Time/℃: 72, 120, 196 h/220 ℃, **Ideal Mole:** 0.01 mole **DI Water:** 140 mL**, Fill Rate of Container:** 70%					
Sample Name	**Si source**	**Na source**	**Mg source**	**Al source**	**Mineralizer**
	Aerosil 130 SiO_2 (g)	$NaCH_3COO$ (g)	$Mg(CH_3COO)_2 \cdot 4H_2O$ (g)	Pural SB1 Al(OH)O (g)	40% HF (mL)
M0.1	2.40	0.08	0.21	1.14	0.1
M0.125	2.40	0.10	0.27	1.13	0.1
M0.18	2.40	0.14	0.38	1.09	0.1

*) Pretreat with 1M hydrochloric acid before mixing as mentioned in chapter 3.2.2

3.3 Analytical and Characterization Method

3.3.1 X-Ray Diffraction Analysis (XRD)

The mineralogical characterization of all samples was determined by XRD on powder sample and textured samples in room humidity. XRD patterns were recorded on a Bruker D8 Advance A25 diffractometer (Bruker Corporation, USA). Quantification of samples was performed using the Rietveld program Profex (version 5.2.9 via www.profex-xrd.org; Doebelin & Kleeberg, 2015). For quantifying the amorphous content within the powder samples, zinc oxide (>99.6%, Merck, Germany) served as an internal standard and was weighed and mixed with powder samples at a weight percentage of 10%.

3.3.2 X-Ray Fluorescence Analysis (XRF)

XRF analysis was employed to investigate the chemical composition of the synthetic samples, a crucial aspect for estimating the layer charge. The analyses were performed on Phillips Axios spectrometer (Malvern Panalytical, Netherlands) equipped with a rhodium X-ray tube (2.4 kW) using powdered samples fused with lithium tetraborate (1:14 mixing ratio). The loss of ignition was determined separately by storing a sample in an oven at 1000 °C for 2 h.

3.3.3 Scanning Electron Microscopy (SEM)

The morphology of synthetic trioctahedral smectite was examined using an environmental scanning electron microscope Philips XL 30 (Thermo Fisher Scientific Inc., USA), operated at 15 - 20 kV in low-vacuum mode with a secondary electron detector. Synthetic samples were compared to natural smectites from the 2:1 smectite group. Laponite® served as standards for synthetic trioctahedral smectite, respectively, chosen due to their structural and morphological similarity. For the morphology of synthetic dioctahedral smectite was analyzed with scanning electron microscopy Zeiss Auriga 60 (Carl Zeiss AG, Germany), operated at 5 - 10 kV with In-lens imaging detector. The combined EDAX EDX detector was also used to identify the elemental composition of specific areas of synthetic samples.

3.3.4 Atomic Force Microscopy (AFM)

Atomic force microscopy (AFM), utilizing a Bruker dimension 3100 instrument equipped with a Nanoscope IV controller (Bruker Corporation, USA), was employed to assess the morphological characteristics of fundamental particles. AFM was used to determine particle size as well as specific edge and basal surface areas (Delavernhe et al., 2015). Powder samples were dispersed in ethanol (99.9%) by 15 min of ultrasonication (37 kHz) to obtain 50 mg/L suspensions, which were then deposited onto freshly cleaned silicon wafers by spin coating to ensure homogeneous dispersion on the surface.

3.3.5 Solid-State Nuclear Magnetic Resonance Spectroscopy (NMR)

The ^{27}Al and ^{19}F MAS NMR spectra were recorded with a Bruker Avance II 400 MHz spectrometer (Bruker Corporation, USA) operating at B_0 = 9.4 Tesla (^{27}Al Larmor frequency of 104.23 MHz), equipped with a Bruker 2.5 mm double channels probe. All ^{27}Al experiments were carried out at room temperature with a $\pi/12$ radio frequency pulse length of 0.5 μs, a recycle delay of 1 s, at a spinning frequency of 30 kHz. The chemical shifts were referred to external $[Al(H_2O)_6]^{3+}$ in $AlCl_3$ aqueous solution. The decompositions of the spectra were performed using the DMFit software (Massiot et al., 2002). For ^{19}F MAS NMR, typical acquisition parameters included 4 μs corresponding to a flip angle of $\pi/2$ pulse and 30 s recycle delay. The chemical shifts were referred to $CFCl_3$ standard reference.

3.3.6 Layer Charge Measurement

The mean value and density of the layer charge in smectite can determine its various properties, which can influence different applications. Nowadays there are several methods for determining the layer charge of smectites. Alkylammonium method (Lagaly, 1981), in which alkylammonium ions with different alkyl chain lengths (n_c = 4 - 12) are used to exchange the smectite interlayer cations and intercalate into the smectite layer, so the interlayer spacing will expand with increasing chain length of the alkylammonium ion. The shift of the d001 due to the expanding of the basal spacing can be observed by XRD analysis.

3.3.7 Cation Exchange Capacity Measurement

The cation exchange capacity (CEC) determination for synthetic samples followed the copper triethylenetetramine (Cu-trien) method (Meier & Kahr, 1999). 50 mg of synthetic and natural samples (Volclay, Calcigel, and Laponite® RD as standard with known CEC values of 85, 63, 79 cmol(+)/kg, respectively) were combined with 10 mL of deionized water and 5 mL of 0.01 M Cu-trien solution within a 15 mL centrifuge tube. Measurement of supernatant absorbance at 580 nm wavelength was conducted using a Genesys 10 UV-Vis Spectrophotometer (Thermo Fischer Scientific Inc., USA) employing disposable polystyrene microcuvettes (1 cm path length; Lab Logistics Groups GmbH, Germany). The CEC (cmol(+)/kg) was determined by quantifying color fade in the supernatant resulting from the exchange of interlayer cations via the Cu-trien solution.

3.3.8 Inductively Coupled Plasma-Optical Emission Spectroscopy (ICP-OES)

ICP-OES Optima 8300DV (PerkinElmer, USA) was utilized to measure the concentrations of exchanged cations in the supernatant. Solution samples obtained from cation exchange experiments were acidified with 1 M HNO_3 to keep the elements of interest in solution, and then diluted with deionized water to fit within the specific measuring range, depending on the element concentrations. The process involves nebulizing the solution into an aerosol and introducing it into an argon plasma, where temperatures reach up to 7000 K. Under these high temperatures, the elements become ionized and subsequently excited, emitting characteristic wavelengths of light that can be precisely measured for quantitative analysis.

3.4 Results and Discussion

3.4.1 Analysis of Synthetic Trioctahedral Smectite

The diffraction patterns of synthetic trioctahedral smectite samples with layer charge settings $\xi = 0.18, 0.125, 0.1$, and Laponite® RD were analyzed by XRD. The 001 peak of all synthetic samples exhibits a broad profile, with reflections at 6.23 - 6.09° (2θ), corresponding to d001 values ranging from 14 - 15 Å . These observations of the 001 peak broadening are possibly affected by a reduction in the size of coherent scattering domains perpendicular to the layer plane (Reinholdt et al., 2013). This reduction in domain size results in broader peaks, which can be estimated using the Scherrer equation. Additionally, the observed phenomena are linked to a loss of periodicity along the c axis (Prieto & Vicente, 1999; Bisio et al., 2008), emphasizing irregularities in the packing of layers, the presence of small particles, and a low degree of crystallinity in all synthetic samples. These combined influences contribute to the altered diffraction pattern, indicating variations in the structural characteristics and organization of the material. Compare to the XRD pattern of Laponite® RD, all the peaks at 2θ = 19°, 34°, 53.03°, and 60.60° were identified and indexed to peaks 110 (4.56 Å), 201 (2.57 Å), and 210 (1.72 Å), respectively. The trioctahedral structure of the synthetic samples can be distinguished based on the position of peak 060 (1.52 Å).

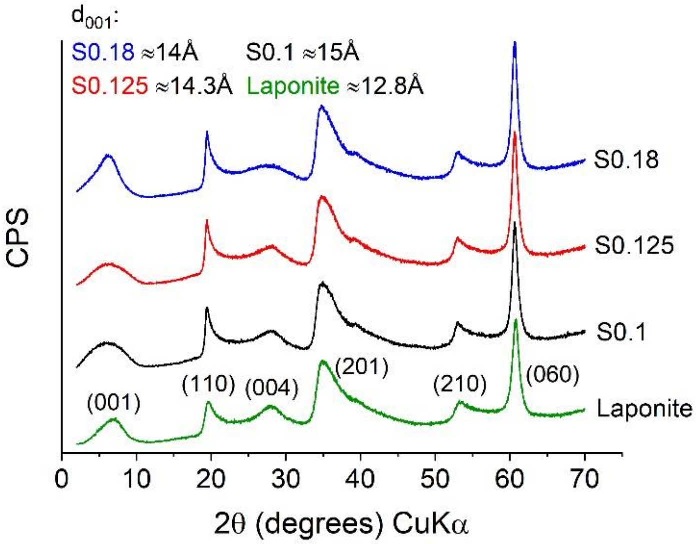

Figure 3.2 Diffraction patterns of standard Laponite® RD and synthetic saponites of different layer charge setting, synthesized for 72 h at 200 °C.

SEM analysis was employed to observe the morphology of the synthetic trioctahedral smectite and it showed the presence of a lamellar structure. The SEM images of both the synthetic smectite and Laponite® RD exhibited a distinctive flake-like structure, consistent with the characteristic morphology observed in saponite materials. It is notable that all synthetic samples exhibit similar layered morphologies, emphasizing the consistency of their structural characteristics. The consistency of morphology between samples provides additional evidence of the effectiveness of the synthesis process in producing trioctahedral smectite materials with comparable characteristics, further supporting the reliability of the synthesis method.

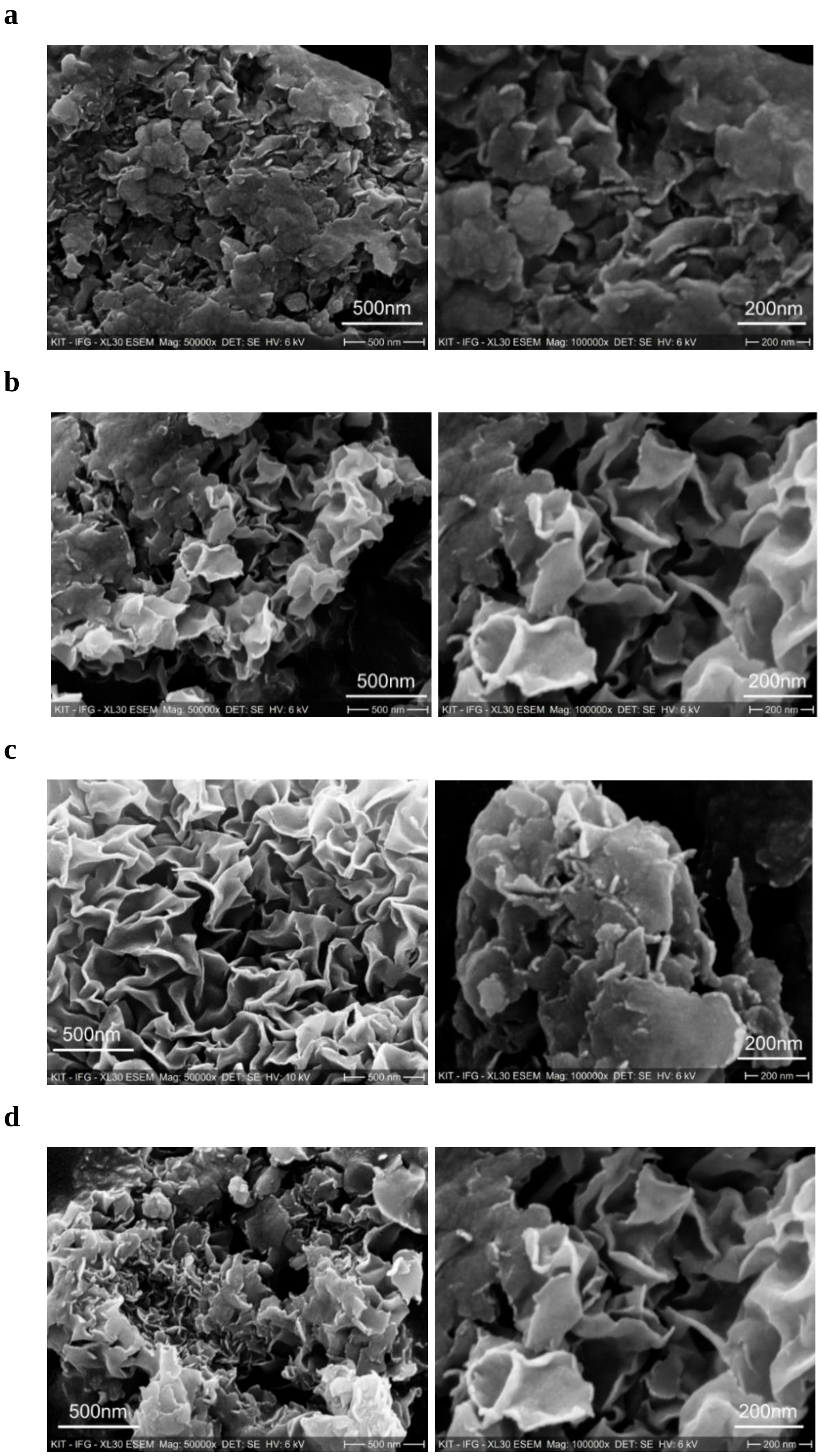

Figure 3.3 SEM images of Laponite® RD and synthetic samples, a: Laponite® RD; b: S0.18; c: S0.125; d: S0.1.

AFM analysis facilitated the straightforward identification of individual particles, allowing for the direct measurement of parameters such as perimeters and basal areas of single particles. Statistical estimation of thickness, perimeter, and basal area was conducted based on a restricted number of particles (approximately 40 or more), which was deemed sufficient for obtaining a representative overview. The thickness of the single layers closely aligned with the expected value of 1.2 - 1.4 nm measured for standard and synthetic smectites under ambient conditions, accounting for one water layer between the particle and the substrate. Despite this, a reference thickness of 0.96 nm for dehydrated smectite was employed in calculations.

The mean weighted perimeter/basal area ratio ($\overline{R}_{P/A}$) was previously measured and range between 0.054 nm^{-1} for Volclay which its total specific surface area of dispersed particles was close to 769 m^2/g with a low $a_{s,edge}$ contribution of about 2.6%. To be a comparison, Laponite® RD is known for small particle size and high edge surface area compare to Volclay. The $\overline{R}_{P/A}$ of Laponite® RD ranged between 0.143 nm^{-1} and for three synthetic samples is 0.109 - 0.118 nm^{-1}. The $a_{s,edge}$ of Laponite® RD was calculated to be around 53 m^2/g, which was close to the range of the synthetic samples (40, 41, 60 m^2/g for S0.18, S0.125 and S0.1). Therefore, the synthetic samples have a similar morphology to the Laponite, which could affect the properties like cation exchange capacity (Table 3.3).

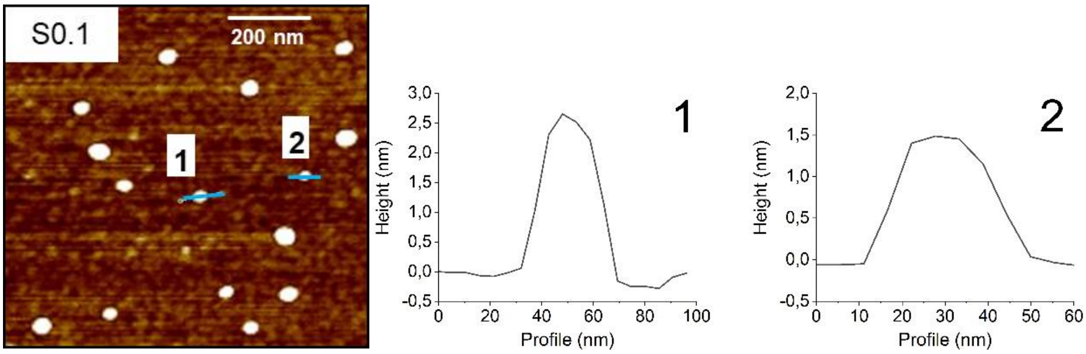

Figure 3.4 AFM images of S0.1: Deflection images and two particle profiles.

Table 3.3 Morphologic parameters of single layer distribution from AFM images and edge surface area estimation.

Samples	Thickness (nm)	$\overline{d}$ (nm)	$\overline{R}_{P/A}$ (nm^{-1})	a_s (m^2/g)	$a_{s,edge}$	
					(m^2/g)	(%)
Volclay	1.25	118	0.054	769	20	2.6
Laponite® RD	1.2	28	0.143	768	53	6.9
S0.18	1.4	38	0.109	773	41	5.3
S0.125	1.5	39	0.106	784	40	5.1
S0.1	1.4	37	0.118	779	60	7.7

To determine the structural composition and cation substitution in synthetic samples, the structural formula (SFM) can be calculated using the chemical composition data obtained from XRF and ICP-OES analyses. The chemical analysis results showed the calculated structural formula that all the synthetic samples with varied degrees of Al substitution for Mg in the octahedral sheets, which can be identified as a typical saponite structure, and only S0.18 also has substitutions in the octahedral sheets. Additionally, XRF analysis revealed the presence of Mg in both the octahedral sheets and interlayer after the synthesis. After that, the determination of the number of interlayer Mg ions necessitates calculation subsequent to the cation exchange process, followed by quantification via ICP-OES (Table 3.4). The calculation procedure of structural formula followed the research of Stevens, 1946 (Stevens, 1946). Previous research mentioned that the layer charges calculated from structural formula tend to be overestimated and is higher than the measured layer charge values by AAM method (Köster, 1977; Kaufhold, 2006; Wolters et al., 2009). It can be the first indirect evidence that all three synthetic saponite have possible lower layer charge $\xi \leq 0.2$.

Table 3.4 Results of chemical analysis of the synthetic samples.

Chemical Composition by XRF & ICP-OES					
Samples	**SiO_2 (%)**	**Al_2O_3 (%)**	**Structural MgO (%)**	**Interlayer MgO (%)**	**Na_2O (%)**
S0.18	52.51	5.62	25.42	0.99	0
S0.125	57.23	2.34	25.19	0.88	0
S0.1	58.14	2.04	24.42	0.83	0

Structural Formula by Stevens, 1946							
Samples	**$^{IV}Si^{4+}$**	**$^{IV}Al^{3+}$**	**$^{VI}Al^{3+}$**	**$^{VI}Mg^{2+}$**	**Interlayer Mg^{2+}**	**Layer Charge (ξ)**	**Molar Mass (g/mol)**
S0.18	3.74	0.26	0.22	2.70	0.10	0.21	380.08
S0.125	4.00	0	0.19	2.62	0.09	0.18	377.50
S0.1	4.00	0	0.25	2.54	0.08	0.17	376.46

The cation exchange capacity (CEC) of synthetic samples was measured using the Cu-trien method, revealing that the measured CEC values exceeded the calculated ones. This difference suggests a potential contribution from higher charge density at the edges of the particles. The influence of charge at edge surfaces, strongly correlated with particle size distribution, is often underestimated in discussions. Delavernhe et al.'s research highlighted the significant impact of the larger edge-specific surface area on the observed increase in CEC (Delavernhe et al., 2015). Even after optimizing the CEC value using edge surface area to compare with the measured CEC, the overestimation of measured CEC still exists for all synthetic sample, which indicate the difficulty using the measured CEC to calculate or predict the layer charge value. Therefore, further investigation into edge charge density is one of the inevitable points for future research of synthetic low charge smectite (Table 3.5).

Table 3.5 The cation exchange capacity analysis results of air-dried synthetic samples (CEC$_{edge}$ was calculated by using $\mathbf{a}_{s,edge}$ from particle size distribution).

Samples	Ideal ξ	SFM ξ	Calc. CEC (from SFM ξ)	Calc. CEC + CEC$_{edge}$*	Measured CEC	Water Content (%)
S0.18	0.18	0.21	55	59	75	9.5
S0.125	0.125	0.18	48	51	53	7.6
S0.1	0.1	0.17	45	49	50	8.6

The layer charge of synthetic smectite was measured using the alkylammonium method (Lagaly, 1981). In this method, the lowest measurement limit of the layer charge value is around 0.2 (using octadecylammonium ion, n_c = 18, according to Chapter 2). Volclay, with layer charge ξ ≈ 0.27, can be determined using the alkylammonium method, where alkylammonium ions with chain lengths of n_c = 16 and 18 form a bilayer structure within the interlayer which can be confirmed through XRD. However, in all three synthetic samples, it was observed that alkylammonium ions with longer chain lengths only formed a specific mixed monolayer/bilayer structure within the interlayer, resulting in a basal spacing of less than 17.7 Å , thereby the synthetic samples have a layer charge distribution around or lower than the measurable limit of the alkylammonium method (Figure 3.5). This observation indirectly supports the possibility that the synthetic samples possess a low layer charge.

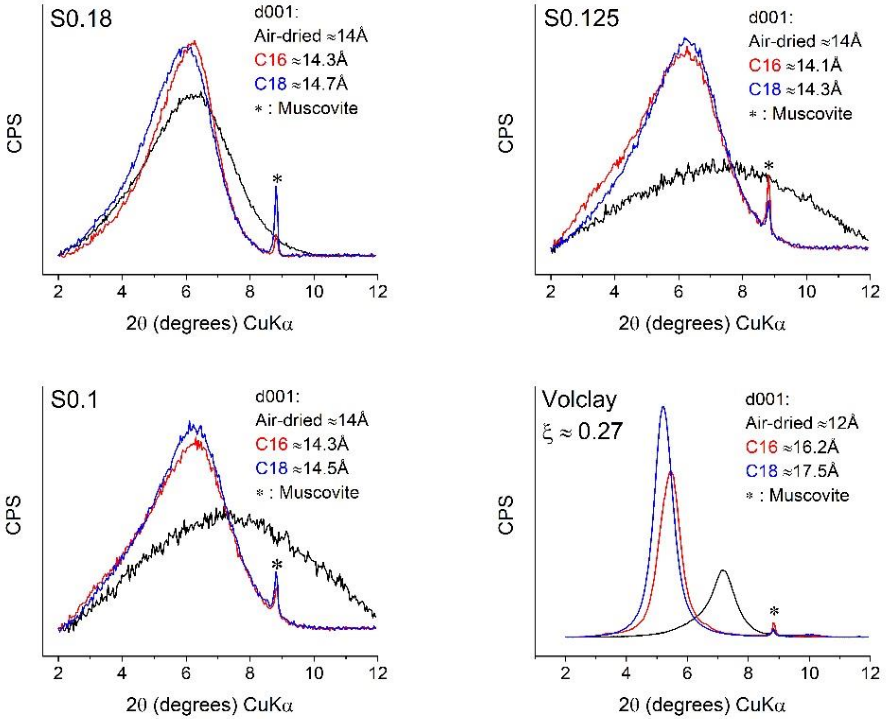

Figure 3.5 Diffraction patterns of synthetic samples and Volclay of air-dried powder and after intercalating the long-chain alkylammonium ions (n_c = 16, 18).

3.4.2 Analysis of Synthetic Dioctahedral Smectite

The diffraction patterns of synthetic montmorillonite samples with varying layer charges $\xi = 0.18, 0.125, 0.1$ p.f.u. synthesized for 72 h at 220℃ under autogenous pressure (Figure 3.6 Left). The reflections of 001 peak is at 6.2 - 6.3° (2θ), corresponding to d001 values ranging from 14 to 14.3 Å . For M0.1 exhibiting a lower degree of Mg^{2+} substitution for Al^{3+}, the peak of montmorillonite and the reflection of d001 at lower angle are weak, and the higher intensity characteristic peak of montmorillonite observed only in samples M0.18 and M0.125. Single-phase montmorillonite was not obtained, accompanied instead by impurities such as kaolinite, boehmite, and small amount of sellaite (MgF_2), as confirmed by the diffraction patterns (Figure 3.6 Right). Most of the synthetic samples contain sellaite and boehmite due to the presence of the mineralizer and unreacted starting material. An increase in kaolinite formation with increasing Al^{3+} amount in the starting material can be seen in all three samples.

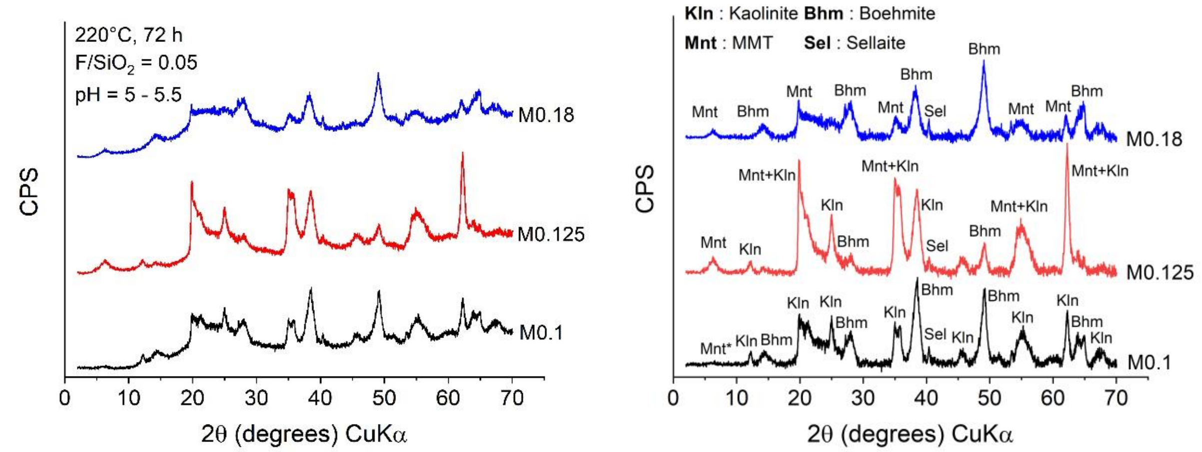

Figure 3.6 Left: Diffraction patterns of synthetic montmorillonite of different layer charge setting; Right: Background subtracted diffraction patterns of synthetic montmorillonite (*: weak reflection of 001 peak).

The duration of synthesis impacts the crystallinity of mineral phase and might influences the reduction of impurities in the final products. For M0.18, a synthesis time of 72 h predominantly yields synthetic products comprising montmorillonite and boehmite. This suggests that the duration of 72 h may not be sufficient for complete reaction, allowing unreacted boehmite to remain detectable in the synthetic product. Beyond 120 h, the samples exhibit a mixture of 2:1 and 1:1 phyllosilicate which are montmorillonite (d001 = 14.3 Å) and kaolinite (d001 = 7.0 Å), indicating partial crystallization of the 2:1 structure due to the presence of kaolinite (Goodyear & Duffin, 1961). Montmorillonite becomes the main phase after 168 h of synthesis, accompanied by a small amount of kaolinite. The lower angle d001 corresponds to the obtaining of swelling smectites, while all samples display the 060 reflection of dioctahedral phyllosilicates (d060 = 1.49 Å). In the case of M0.125, a synthesis duration of 72 h yields montmorillonite; however, the presence of a small amount of kaolinite and boehmite is also observed. Subsequent to 120 h, kaolinite begins to dominate as the primary phase in the synthetic product. Even with a synthesis duration of 168 hours, the increase in the crystallinity of both montmorillonite and kaolinite is observed. The lowest layer charge setting, M0.1, is synthesized only during two durations: 72 and 168 h. Owing to the high Al content in the starting materials, the gradual formation of kaolinite with small amount of montmorillonite is detectable, and sellaite is obtained in nearly every synthesized product. The tendency of sellaite formation in most synthetic samples results in a reduction of Mg^{2+} available for montmorillonite formation. With lower Mg^{2+} concentrations and higher amounts of Al^{3+} available for reaction at the early stage of synthesis, it appears that Si and Al^{3+} preferentially form kaolinite instead of montmorillonite.

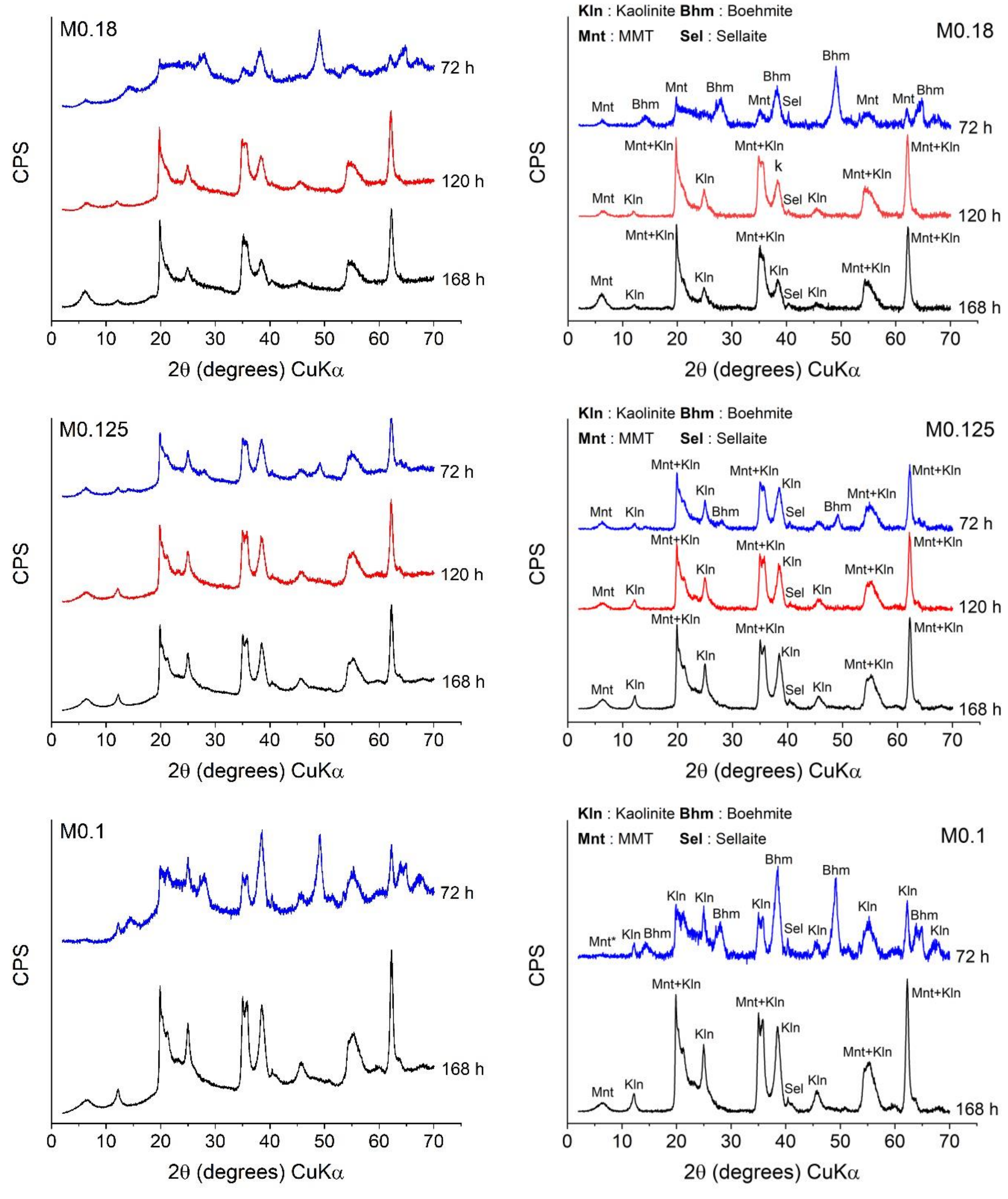

Figure 3.7 Diffraction patterns of synthetic montmorillonite M0.18, M0.125 and M0.1 with the different crystallization time. Left: original diffraction patterns; Right: background subtracted diffraction patterns.

As indicated by the diffraction patterns, impurities were present in all samples (Table 3.6). The synthesis of M0.18 exhibited the best crystallinity of montmorillonite and lower intensity of peaks characteristic of kaolinite after longer-term synthesis. However, the syntheses of M0.125 and M0.1 showed higher intensities of kaolinite characteristic peaks under all synthesis conditions. This highlights that while the duration of synthesis is significant, but it is not the only factor influencing the formation of single-phase montmorillonite or reducing the impurities such as kaolinite. Factors such as avoiding the partial reactions between only two of the starting materials and adjusting and finding the reasonable degree of Mg^{2+} to Al^{3+} substitution should also be considered. These adjustments play a crucial role in optimizing the synthesis process and achieving the desired purity and phase composition in the final product.

Table 3.6 The synthesis condition and products of synthetic samples M0.18, M0.125 and M0.1 at 220 ℃.

Samples	Time	pH	MMT	Impurties
M0.18	3 d	5	V	Bohmite, Sellaite
	5 d	5 - 5.5	V	Kaolinite, Sellaite
	7 d	5 - 5.5	V	Kaolinite, Sellaite
M0.125	3 d	5	V	Kaolinite, Bohmite, Sellaite
	5 d	4.5 - 5	V	Kaolinite, Sellaite
	7 d	5 - 5.5	V	Kaolinite, Sellaite
M0.1	3 d	4.5 - 5	V	Kaolinite, Bohmite, Sellaite
	7 d	5 - 5.5	V	Kaolinite, Sellaite

Due to the nature of the small particles in synthetic samples, single particles are hard to observe, as most of them form aggregates. SEM images revealed a flake structure similar to the morphology of montmorillonite, with dust-like small particle aggregates covering or surrounding it. (Figure 3.8). After the extension of synthesis duration, synthetic samples showed a clearer flake structure and the reduction of dust-like particles could be observed. The qualitative EDS analysis indicates that flake structures is likely a mixture of montmorillonite and kaolinite based on the Si/Al elemental weight and chemical composition results, while the presence of dust-like aggregates could be mainly unreacted SiO_2 or an amorphous silicate phase (Figure 3.9). However, distinguishing between montmorillonite and kaolinite from their characteristic structures when both phases are present in the synthetic samples is challenging.

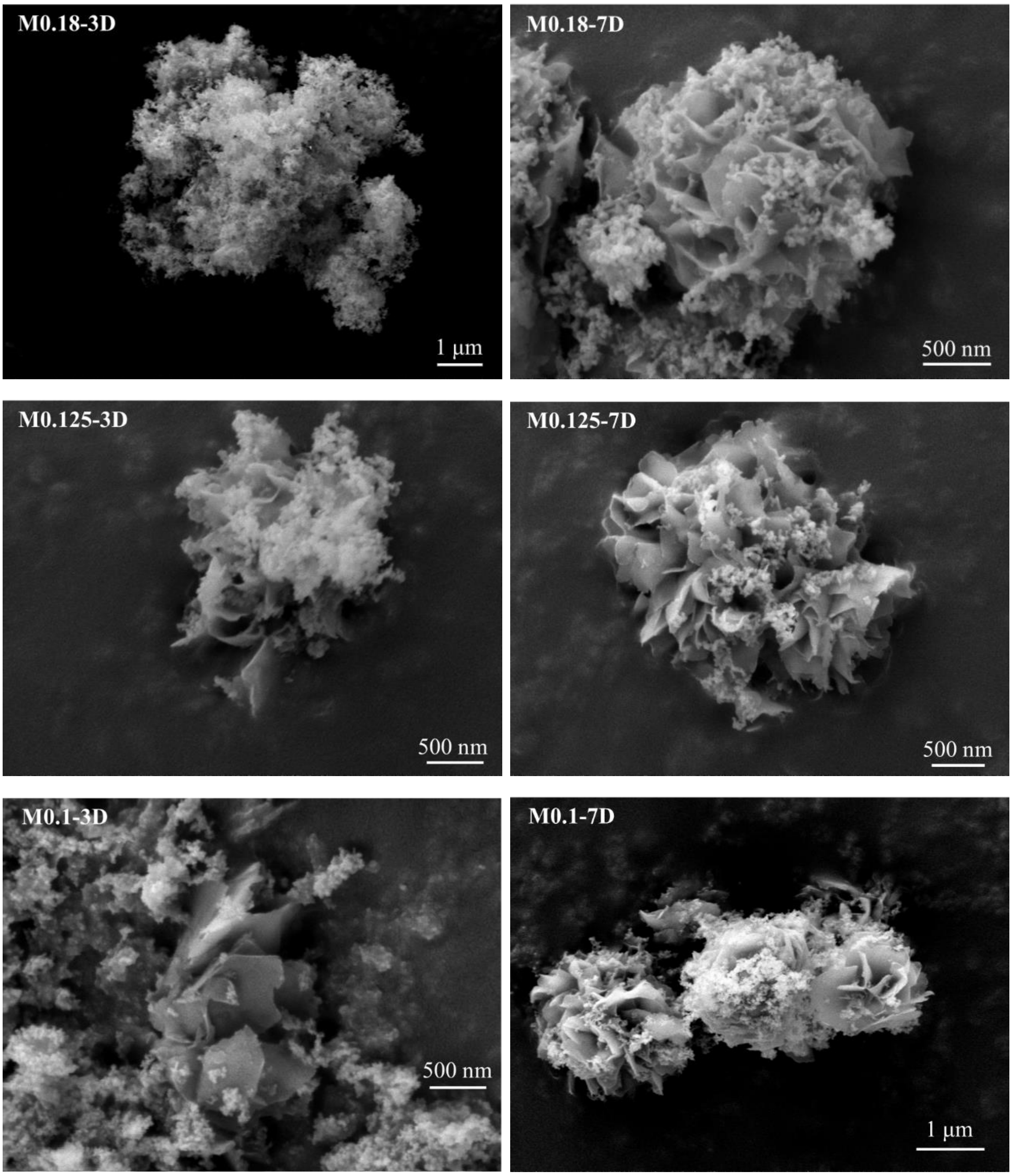

Figure 3.8 SEM images of synthetic samples M0.18, M0.125 and M0.1

Figure 3.9 EDS analysis of synthetic samples.

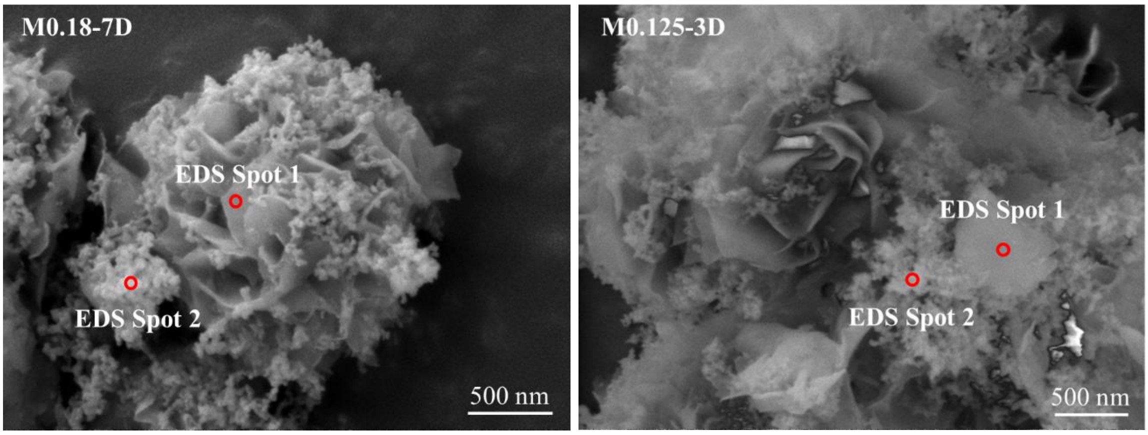

Table 3.7 Element weight and chemical composition of synthetic samples by EDS analysis.

Element Weight (%)		**Si**	**Al**	**Mg***	**Na***	**F***	**O**
M0.18-7D	**Spot 1**	21.8	13.1	0.6	0.2	1.2	63.1
	Spot 2	30.9	2.1	0	0	0	67
M0.125-3D	**Spot 1**	22.5	13.5	0.6	0.1	1.2	62
	Spot 2	27.4	4.9	0	0	0	67.7

Chemical Composition (%)		**SiO_2**	**Al_2O_3**	**MgO**	**Na_2O**	**F**
M0.18-7D	**Spot 1**	63.15	33.52	1.35	0.37	1.62
	Spot 2	94.34	5.66	0	0	0
M0.125-3D	**Spot 1**	63.36	33.58	1.31	0.18	1.58
	Spot 2	86.36	27.72	0	0	0

*) The analysis error for Mg, Na, and F is high due to the insufficient scanning time; therefore, the values have low accuracy in describing the element weight (%).

Solid-State NMR Spectroscopy were used to provide information of chemical composition including the substitution of Al^{3+} in the octahedral or tetrahedral sheet, as well as the substitution of F ions for hydroxy groups or any impurities containing fluoride within the structure. ^{27}Al MAS NMR spectroscopy indicates that all synthetic samples contain both peaks of Al^{VI} ($\delta = 2 - 5$ ppm) and Al^{IV} ($\delta = 64 - 69$ ppm), and proof the Al^{3+} locates in both the tetrahedral and octahedral sheet, this result showed that the layer charge of synthetic montmorillonite should be contributed by both Al^{3+} substitution at octahedral and tetrahedral sheet. The distortions of the phyllosilicate structure can be observed by the secondary peak of Al^{IV} appears around 50 - 56 ppm (Goodman & Stucki 1984, Sanz & Serratosa, 1984, Plee et al., 1985). After extend the synthesis duration, the absent of secondary Al^{IV} peak indicates the reduction of distorted tetrahedral Al environments.

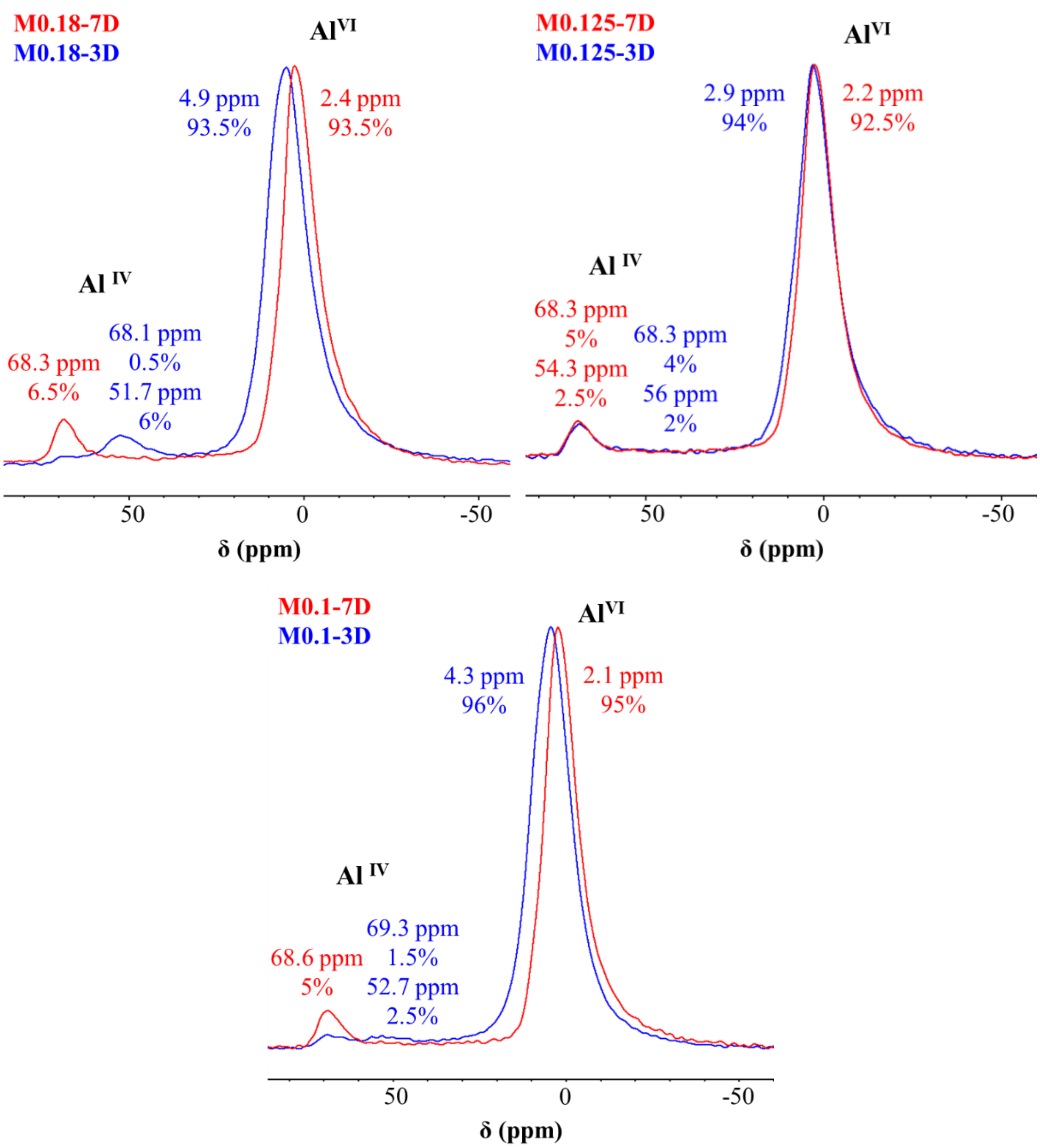

Figure 3.10 ^{27}Al MAS NMR spectra of synthetic samples M0.18, M0.125 and M0.1.

^{19}F MAS NMR spectroscopy showed several peaks with chemical shifts corresponding to various fluorine environments. The peak of Si-F fluorine environment ($\delta = -140$ ppm) indicated the F substitution for hydroxy groups in the tetrahedral sheet. Another peak of MgF_2 fluorine environments ($\delta = -198$ ppm) showed the presence of sellaite in almost every synthetic sample. The peak intensity decreased with increased synthesis duration, which could indicate that sellaite is an intermediate phase during the synthesis. Additionally, the peaks of Mg-Al-□ ($\delta = -153$ ppm) and Al-Al-□ ($\delta = -134$ ppm) fluorine environments, where □ indicates a vacancy in the octahedral sheet, were influenced by environment in the octahedral sheets, including the substitution of Mg^{2+} for Al^{3+} (Huve et al. 1992). For the synthetic samples, these peaks could be affected by whether the main phase of is montmorillonite or kaolinite.

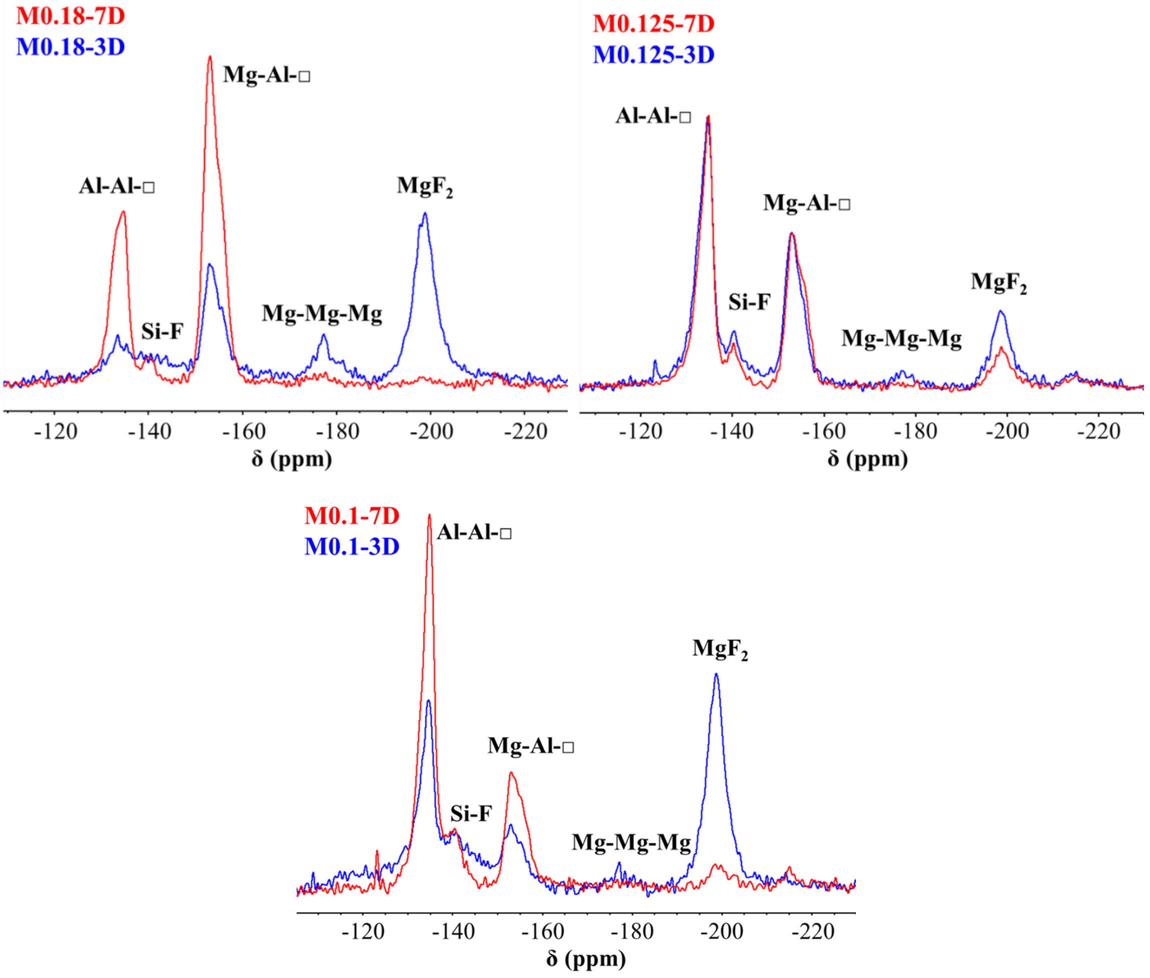

Figure 3.11 ^{19}F MAS NMR spectra of synthetic samples M0.18, M0.125 and M0.1.

Building upon the previous XRD pattern and analysis results, the structural formula calculation necessitates a comprehensive analysis involving both the powder samples and the supernatant after washing the synthetic product to account for impurities and amorphous phase. If the single-phase product can be obtained, chemical composition data obtained from XRF analyses and quantification of synthetic powder samples by the Rietveld program Profex can be utilized to predict the synthetic montmorillonite's structural formula. This approach enables the prediction of the layer charge range of the synthetic montmorillonite, providing valuable insights into its structural composition and potential improvement for future synthesis.

Based on the analysis results from Profex, when the synthesis duration is extended, the mineral phases of synthetic samples begin to change from containing multiple impurities to consisting phases only of montmorillonite and kaolinite. As the percentage of Al^{3+} in the starting hydrogel increases, the content of montmorillonite decreases from 62% to 56%, while the content of kaolinite increases, which can be also observed based on XRD patterns. The formation of sellaite can be observed in most synthetic samples by XRD, and its percentage decreases in all samples synthesized for longer durations, which is supported by the analysis results of ^{19}F MAS NMR. However, its low percentage makes it difficult to accurately quantify its amount in some synthetic samples using the Profex analysis (Table 3.8).

Table 3.8 Phase quantification analysis of synthetic samples M0.18, M0.125 and M0.1.

Phase Quantification of Synthetic Samples by Profex						
Samples Name	**Duration (d)**	**MMT (%)**	**Kaolinite (%)**	**Sellaite (%)**	**Boehmite (%)**	**Amorphous (%)**
M0.18	3	33	0	1.4	26	39.6
	7	62.4	15.4	0*	0	22.2
M0.125	3	56.1	17.7	0*	4.1	22.1
	7	56.8	25.8	0*	0	17.4
M0.1	3	13.7	44.2	1	17.6	23.5
	7	56.8	31	0*	0	12.2

The chemical composition and total composition weight of each component in the synthetic samples and supernatant were analyzed by XRF and ICP-OES, respectively, providing detailed information about the synthetic montmorillonite. For the SiO_2 percentage of the synthetic samples, a slightly lower amount compared to the starting material was observed. The percentage of Al_2O_3 in synthetic samples is also slightly higher than in the starting hydrogel, likely due to the presence of kaolinite and boehmite impurities in the synthetic samples. Conversely, the percentage of Na_2O in the synthetic samples is lower than the expected value for the ideal starting material, which could be affected by the presence of different exchangeable cations (Mg^{2+}, Na^{+}) in the synthetic montmorillonite structure. This can cause part of the percentage of Mg represent not only the substitution of Mg^{2+} in octahedral sheets but also in the interlayer. The low percentage of Na_2O in the synthetic samples can be confirmed by supernatant analysis, showing that 50% or more of the Na^+ did not enter the interlayer of montmorillonite and was washed out after synthesis (Table 3.9). The total composition weight of SiO_2 measured by XRF and ICP-OES is close to the amount added in the starting hydrogel. However, for the other components, Al_2O_3, MgO, and Na_2O, there are still over- or underestimations, leading to uncertainty and decreasing the accuracy in describing the chemical composition of synthetic montmorillonite (Table 3.10).

To calculate and predict the structural formula and layer charge of the montmorillonite phase accurately, the composition of impurities and the amorphous phase must be precisely analyzed. The phase quantification and chemical composition of synthetic samples can be analyzed using Profex, XRF, and ICP-OES. However, the unknown composition of amorphous phases and other uncertainties during the composition analysis make it challenging to separate the amorphous phase and determine the actual chemical composition of synthetic montmorillonite. Future synthesis strategies should focus on increasing the percentage and crystallinity of the montmorillonite phase and reducing the amount of the amorphous phase.

Table 3.9 Chemical composition of starting hydrogel and synthetic samples M0.18, M0.125 and M0.1.

Ideal Chemical Composition of Starting Material					
Samples		**SiO_2 (%)**	**Al_2O_3 (%)**	**MgO (%)**	**Na_2O (%)**
M0.18		69.47	26.82	2.10	1.61
M0.125		69.70	27.72	1.46	1.12
M0.1		69.80	28.13	1.17	0.90
Chemical Composition of Synthetic Samples by XRF					
Samples	**Duration (d)**	**SiO_2 (%)**	**Al_2O_3 (%)**	**MgO (%)**	**Na_2O (%)**
M0.18	3	68.46	29.09	2.25	0.20
	7	68.63	28.62	2.43	0.33
M0.125	3	65.11	33.00	1.78	0.11
	7	69.09	29.13	1.61	0.17
M0.1	3	68.00	30.66	1.21	0.13
	7	67.98	30.58	1.30	0.14

Table 3.10 Total chemical weight analysis of the starting hydrogel and synthetic samples M0.18, M0.125 and M0.1.

Chemical Weight Analysis of Synthetic Samples by XRF & ICP-OES						
Samples	**Duration (d)**	**Types of samples**	**SiO_2 (g)**	**Al_2O_3 (g)**	**MgO (g)**	**Na_2O (g)**
M0.18	3	**Starting hydrogel**	**2.404**	**1.856**	**0.073**	**0.112**
		Synthetic powder (XRF)	1.862	0.972	0.073	0.007
		Supernatant (ICP-OES)	0.299	0.019	0.016	0.147
		Sum	**2.161**	**0.991**	**0.089**	**0.154**
	7	**Starting hydrogel**	**2.404**	**1.856**	**0.073**	**0.112**
		Synthetic powder (XRF)	1.907	0.956	0.081	0.011
		Supernatant (ICP-OES)	0.294	0.004	0.001	0.064
		Sum	**2.201**	**0.960**	**0.082**	**0.057**
M0.125	3	**Starting hydrogel**	**2.404**	**1.912**	**0.050**	**0.077**
		Synthetic powder (XRF)	1.690	1.513	0.036	0.003
		Supernatant (ICP-OES)	0.223	0.015	0.004	0.049
		Sum	**1.913**	**1.528**	**0.040**	**0.053**
	7	**Starting hydrogel**	**2.404**	**1.912**	**0.050**	**0.077**
		Synthetic powder (XRF)	1.788	1.331	0.032	0.005
		Supernatant (ICP-OES)	0.363	0.007	0.001	0.043
		Sum	**2.151**	**1.339**	**0.033**	**0.048**
M0.1	3	**Starting hydrogel**	**2.404**	**1.937**	**0.040**	**0.062**
		Synthetic powder (XRF)	1.782	1.420	0.025	0.004
		Supernatant (ICP-OES)	0.204	0.018	0.004	0.039
		Sum	**1.986**	**1.438**	**0.028**	**0.043**
	7	**Starting hydrogel**	**2.404**	**1.937**	**0.040**	**0.062**
		Synthetic powder (XRF)	1.793	1.425	0.027	0.005
		Supernatant (ICP-OES)	0.347	0.008	0.000	0.035
		Sum	**2.139**	**1.433**	**0.027**	**0.040**

3.5 Summary and Future Outlook

This research focused on the synthesis of low charge trioctahedral and dioctahedral smectites with layer charge ξ = 0.18, 0.125 and 0.1. The XRD analysis revealing the successful synthesis of single-phase trioctahedral smectite with interlayer Mg^{2+}. The broadening of the 001 peak are possibly affected by a reduction in the size of coherent scattering domains perpendicular to the layer plane (Reinholdt et al., 2013), which can be estimated using the Scherrer equation. The morphology of the synthetic trioctahedral smectite showed the presence of a lamellar structure similar to the Laponite® RD and natural saponite by SEM. The measured CEC values exceeded the calculated CEC. This suggests a potential contribution from higher charge density at the edges of the particles also proved by the AFM analysis, in this case the layer charge is difficult to obtain from CEC value. Therefore, the layer charge can only be estimated by structural formula or traditional layer charge measurement by Alkylammonium method. The structural formula calculated from chemical composition from XRF and ICP-OES analyses revealing a possible low charge with ξ = 0.17 - 0.21, and for all three synthetic samples, it was observed even alkylammonium ions with longer chain lengths (n_c = 16, 18) only formed a monolayer structure in the interlayer, confirming that the synthetic samples have a layer charge lower than the measurable limit of the alkylammonium method. These can be the indirect evidences to support the possibility that the synthetic trioctahedral smectites possess a low layer charge.

Even though the successful synthesis of trioctahedral smectite has been achieved, the synthesis of low charge montmorillonite remains questionable. The synthetic samples do not yield a single-phase montmorillonite but are accompanied by several impurities, including kaolinite, boehmite, and sellaite, as confirmed by XRD analysis. Extending the synthesis duration increased the crystallinity of the montmorillonite phase, but removing the formation of impurities such as kaolinite proved challenging. SEM images showed a distinctive flake structure similar to the morphology of montmorillonite, with dust-like small particle aggregates covering or surrounding them. Qualitative EDS analysis indicates that the flake structures have a chemical composition similar to montmorillonite, while the dust-like aggregates could be unreacted SiO_2 or an amorphous phase. Results from ^{27}Al MAS NMR spectroscopy showed that Al^{3+} locates in both the tetrahedral and octahedral sheet of synthetic montmorillonite. Additionally, ^{19}F MAS NMR spectroscopy indicated the substitution of F for hydroxy groups in the tetrahedral sheet, and also suggesting that the amount of sellaite can be decreased by increasing the synthesis duration. Based on the quantitative phase analysis by Rietveld program Profex, when the synthesis duration is extended, the mineral phases of the synthetic samples begin to change from containing multiple impurities to having only montmorillonite and kaolinite, with the percentage of synthetic montmorillonite around 56 - 62%. However, the amorphous phase still exists in all synthetic samples. XRF and ICP-OES analysis of the synthetic samples indicates the possibility of various exchangeable cations (Mg^{2+}, Na^{+}) in the synthetic montmorillonite structure. In conclusion, the analysis of synthetic montmorillonite reveals several challenges in accurately determining their actual chemical composition and structural formula due to impurities, the presence of an amorphous phase, and variability in chemical composition analysis.

In planning future synthesis procedures for low charge montmorillonite, the primary objective should be enhancing its percentage and crystallinity of montmorillonite phase and reducing the percentage of amorphous phase in synthetic samples through systematic optimization of experimental parameters. One effective approach is the application of design of experiments such as the Taguchi method, a statistical methodology for efficient experimentation and process control aimed at improving product quality. By applying design of experiments, we can assess the impact of each experimental parameter on the quality improvement of the synthetic samples, thereby avoiding or reducing the need for trial synthesis experiments. The flexibility and limitations of adjusting all synthesis parameters, such as heating temperature, synthesis duration, pressure and concentration of hydrogel, should be increased. In this study, synthesis temperatures were set at 200 ℃ for trioctahedral smectite and 220 ℃ for dioctahedral smectite due to safety limits of commercial stainless-steel autoclaves with PTFE containers. Selecting different types of autoclaves or other synthesis equipment could provide more parameter combinations to enhance the synthesis efficiency and quality of low charge montmorillonite. Furthermore, the relationship between the fill rate and pressure of the inner container in the autoclave should be considered. In traditional synthesis methods, the pressure inside the container can only be controlled by the temperature and the fill rate of the container (Rabenau, 1985; Walton, 2002). The trial experiments in this study revealed that a fill rate around 60 - 66% can still yield montmorillonite. Therefore, the fill rate could be a parameter for improving future synthesis experiments. Pressure during the synthesis has always been mentioned as an important factor, along with temperature and duration. Several studies have obtained single-phase montmorillonite under high pressure conditions (Lantenois et al., 2008; Le Forestier et al., 2010; Golubeva, 2016). Adjustments in these experimental parameters, guided by systematic experimentation and analysis, hold promise for enhancing the quality and characteristics of synthesized montmorillonite.

Other than the experimental conditions related to the equipment, the selection of chemicals and how to control the starting material during the reaction are factors that can be adjusted. For example, in most successful synthesis cases of montmorillonite with autogenous water pressure, it has been noted that without fluoride ions in the synthesis process, the crystallization of montmorillonite cannot be achieved (Reinholdt et al., 2001, 2005; Golubeva, 2018, de Oliveira et al., 2021). The presence of fluoride in small amounts is crucial for obtaining single-phase montmorillonite. Therefore, alternative sources of fluoride can be considered as potential replacements for HF such as sodium fluoride or ammonium fluoride in future synthesis. The formation of sellaite leads to a decrease in the concentration of Mg^{2+} at the early stage of synthesis, and decrease its amount for some of the synthetic samples with longer synthesis duration. If the reduction in Mg^{2+} concentration can be precisely quantified, elemental compensation by adding an excess amount of Mg^{2+} to the starting hydrogel might increase the possibility of obtaining low charge montmorillonite and could be a new experimental parameter to consider in future experimental designs. Altering the addition order of starting materials offers another avenue for optimization. When all synthetic samples in this research contain impurties, which can interrupt the ideal design chemical composition of synthetic montmorillonite. Comparing to the addition sequence of starting material in this study: deionized water $\rightarrow$ F $\rightarrow$ Na^{+} $\rightarrow$ Mg^{2+} $\rightarrow$ Al^{3+} $\rightarrow$ Si (Reinholdt et al., 2001, 2005), different combination of starting materials was mixed separately without aging. For example, chemicals with Al + Na and Mg + Si were mixed first with deionized water, then was added together with the mineralizer with F as the last step in order to avoid the formation of any possible compound right before hydrothermal synthesis. This assumption could be one of the subjects to be tested in future experimental designs, along with investigating the impact of aging time on the final product.

References

Bisio, C., Gatti, G., Boccaleri, E., Marchese, L., Superti, G. B., Pastore, H. O., & Thommes, M. (2008). Understanding physico–chemical properties of saponite synthetic clays. *Microporous and Mesoporous Materials*, *107*(1–2), 90–101.

Decarreau, A., Petit, S., Martin, F., Farges, F., Vieillard, P., & Joussein, E. (2008). Hydrothermal synthesis, between 75 and 150°C, of high-charge, ferric nontronites. *Clays and Clay Minerals*, *56*(3), 322–337.

Delavernhe, L., Steudel, A., Darbha, G. K., Schäfer, T., Schuhmann, R., Wöll, C., Geckeis, H., & Emmerich, K. (2015). Influence of mineralogical and morphological properties on the cation exchange behavior of dioctahedral smectites. *Colloids and Surfaces A: Physicochemical and Engineering Aspects*, *481*, 591–599.

Delavernhe, L., Pilavtepe, M., & Emmerich, K. (2018). Cation exchange capacity of natural and synthetic hectorite. *Applied Clay Science*, *151*, 175–180.

de Oliveira, L. H., Trigueiro, P., Rigaud, B., da Silva-Filho, E. C., Osajima, J. A., Fonseca, M. G., Lambert, J.-F., Georgelin, T., & Jaber, M. (2021). When RNA meets montmorillonite: Influence of the pH and divalent cations. *Applied Clay Science*, *214,* 106234.

Doebelin, N., & Kleeberg, R. (2015). Profex: A graphical user interface for the Rietveld refinement program BGMN. *Journal of Applied Crystallography*, *48*(5), 1573–1580.

Eisenhour, D. D., & Brown, R. K. (2009). Bentonite and its impact on modern life. *Elements, 5*(2), 83–88.

Goodman, B. A., & Stucki, J. W. (1984). The use of nuclear magnetic resonance (NMR) for the determination of tetrahedral aluminium in montmorillonite. *Clay Minerals*, *19*(4), 663–667.

Goodyear, J., & Duffin, W. J. (1961). An X-ray examination of an exceptionally well crystallized kaolinite. *Mineralogical Magazine and Journal of the Mineralogical Society*, *32*(254), 902–907.

Golubeva, O. Y. (2016). Effect of synthesis conditions on hydrothermal crystallization, textural characteristics and morphology of aluminum-magnesium montmorillonite. *Microporous and Mesoporous Materials*, *224*, 271–276.

Huve, L., Delmotte, L., Martin, P., Le Dred, R., Baron, J., & Saehr, D. (1992). 19F MAS-NMR study of structural fluorine in some natural and synthetic 2: 1 layer silicates. *Clays and Clay Minerals*, *40*(2), 186–191.

Jaber, M., & Miéhé-Brendlé, J. (2005). Influence du milieu de synthèse sur la cristallisation de saponite: Proposition de mécanisme réactionnel en milieux acide et basique. *Comptes Rendus Chimie*, *8*(2), 229–234.

Jaber, M., & Miehé-Brendlé, J. (2008). Synthesis, characterization and applications of 2: 1 phyllosilicates and organophyllosilicates: Contribution of fluoride to study the octahedral sheet. *Microporous and Mesoporous Materials, 107*(1–2), 121–127.

Jasmund, K., & Lagaly, G. (2013). *Tonminerale und Tone: Struktur, Eigenschaften, Anwendungen und Einsatz in Industrie und Umwelt*. Springer-Verlag.

Joni, I. M., Rukiah, & Panatarani, C. (2020). *Synthesis of silica particles by precipitation method of sodium silicate: Effect of temperature, pH and mixing technique*. *2219*, 080018.

Karnland, O., Olsson, S., & Nilsson, U. (2006). *Mineralogy and sealing properties of various bentonites and smectite-rich clay materials*. Swedish Nuclear Fuel and Waste Management Co.

Kaufhold, S. (2006). Comparison of methods for the determination of the layer charge density (LCD) of montmorillonites. *Applied Clay Science, 34*(1–4), 14–21.

Köster, H. M. (1977). Die Berechnung kristallchemischer Strukturformeln von 2: 1-Schichtsilikaten unter Berücksichtigung der gemessenen Zwischenschichtladungen und Kationenumtauschkapazitäten, sowie die Darstellung der Ladungsverteilung in der Struktur mittels Dreieckskoordinaten. *Clay Minerals, 12*(1), 45–54.

Lagaly, G. (1981). Characterization of clays by organic compounds. *Clay Minerals, 16*(1), 1–21.

Lantenois, S., Champallier, R., Bény, J.-M., & Muller, F. (2008). Hydrothermal synthesis and characterization of dioctahedral smectites: A montmorillonites series. *Applied Clay Science, 38*(3–4), 165–178.

Le Forestier, L., Muller, F., Villieras, F., & Pelletier, M. (2010). Textural and hydration properties of a synthetic montmorillonite compared with a natural Na-exchanged clay analogue. *Applied Clay Science, 48*(1–2), 18–25.

Massiot, D., Fayon, F., Capron, M., King, I., Le Calvé, S., Alonso, B., Durand, J.-O., Bujoli, B., Gan, Z., & Hoatson, G. (2002). Modelling one-and two-dimensional solid-state NMR spectra. *Magnetic Resonance in Chemistry, 40*(1), 70–76.

Meier, L. P., & Kahr, G. (1999). Determination of the Cation Exchange Capacity (CEC) of Clay Minerals Using the Complexes of Copper (II) Ion with Triethylenetetramine and Tetraethylenepentamine. *Clays and Clay Minerals, 47*(3), 386–388.

Plee, D., Borg, F., Gatineau, L., & Fripiat, J. J. (1985). High-resolution solid-state aluminum-27 and silicon-29 nuclear magnetic resonance study of pillared clays. *Journal of the American Chemical Society, 107*(8), 2362–2369.

Prieto, O., Vicente, M. A., & Bañares-Muñoz, M. A. (1999). Study of the porous solids obtained by acid treatment of a high surface area saponite. *Journal of Porous Materials, 6*, 335–344.

Rabenau, A. (1985). The role of hydrothermal synthesis in preparative chemistry. *Angewandte Chemie International Edition in English*, *24*(12), 1026–1040.

Reinholdt, M., Miehé-Brendlé, J., Delmotte, L., Tuilier, M.-H., le Dred, R., Cortès, R., & Flank, A.-M. (2001). Fluorine route synthesis of montmorillonites containing Mg or Zn and characterization by XRD, thermal analysis, MAS NMR, and EXAFS spectroscopy. *European Journal of Inorganic Chemistry*, *2001*(11), 2831–2841.

Reinholdt, M., Miehé-Brendlé, J., Delmotte, L., Le Dred, R., & Tuilier, M.-H. (2005). Synthesis and characterization of montmorillonite-type phyllosilicates in a fluoride medium. *Clay Minerals*, *40*(2), 177–190.

Reinholdt, M. X., Miehé-Brendlé, J., Tuilier, M.-H., Kaliaguine, S., & Ambroise, E. (2013). Hydrothermal synthesis and characterization of Ni-Al montmorillonite-like phyllosilicates. *Nanomaterials*, *3*(1), 48–69.

Sanz, J., & Serratosa, J. M. (1984). Silicon-29 and aluminum-27 high-resolution MAS-NMR spectra of phyllosilicates. *Journal of the American Chemical Society*, *106*(17), 4790–4793.

Stevens, R. E. (1946). A system for calculating analyses of micas and related minerals to end members. *US Geol. Surv. Bull*, *950*, 101–119.

Walton, R. I. (2002). Subcritical solvothermal synthesis of condensed inorganic materials. *Chemical Society Reviews*, *31*(4), 230–238.

4 DFT Simulation of Hydration of Trans-vacant and Cis-vacant Low Charge Dioctahedral Smectite

4.1 Introduction

Swellable clay minerals, particularly smectites, play a crucial role in diverse geotechnical and industrial applications. Their exceptional swelling capacity is important for constructing reliable hydraulic barriers of bentonite sealing systems in underground waste disposal systems, internationally acknowledged as a secure approach. On the other hand, modern technological developments have led to the conversations concerning the latest advancements in 2D layered materials, particularly their role in advancing coherent quantum photonic devices and quantum emitters, their current state of development, and the strategies employed to address existing challenges. Also owing to their biocompatible attributes, distinctive morphology, high surface-to-volume ratio, and charge properties. Clay materials have received wide attention in various biomedical applications. This includes their interactions with various biological elements such as cells, proteins and polymers. Nevertheless, challenges persist in understanding the variability of swelling patterns and accurately predicting stable hydration states, true water content, and saturation levels. These aspects are paramount for effectively modeling the clay's behavior over the long term (Wolters et al., 2009; Sellin & Leupin, 2013; Delavernhe et al., 2015; Kuligiewicz & Derkowski, 2017; Gaharwar et al., 2019; Turunen et al., 2022).

Smectites are comprised of 2:1 layer constructed from an octahedral sheet located between two tetrahedral sheets. The primary tetrahedral cation is Si^{4+}. In dioctahedral 2:1 layer, Al^{3+} and other trivalent cations serve as common octahedral cations. Isomorphic substitutions in both the tetrahedral and octahedral sheets generate a negative layer charge, which is balanced by interlayer cations. The layer charge $\xi = 0.2 - 0.6$ per formula unit (p.f.u.), corresponding to $M^{n+}_{x/n}$ $(Si_{4-y}\ Al_y)$ $[(Al, Fe^{3+})_{2-z}\ (Mg, Fe^{2+})_z]$ O_{10} $(OH)_2$, where $x/n = \xi$ with $x = y+z$ (p.f.u.), and M^{n+} symbolize the interlayer cation. The hydration and swelling of smectites are determined not only by the characteristics of interlayer cations but also by the layer charge density and location of substitutions. In dioctahedral smectite, the octahedral sheet has two symmetrically cis-octahedrons divided by hydroxyl groups and one trans-octahedron, which can be described as two cis-sites and one trans-site. One out of three octahedron is not occupied by cations, forming a vacant site. The disposition between vacant site at the octahedral sheet and hydroxyl groups determine two different crystal forms, when the hydroxyl groups are on the same side (cis-vacant, CV) or on opposite sides (trans-vacant, TV) of the vacant site. This connection is especially significant since the montmorillonite series has multiple structural variations, such changes may lead to the change of properties such as exchange capacity, swelling behavior, and adsorption characteristics (Méring & Oberlin, 1971; Guggenheim et al., 2006; Emmerich et al., 2009).

One of the important aspects of this study is the swelling behavior of low charge montmorillonite. Smectite's significant swelling behavior arises from the movement of water molecules into and out of its interlayer. This crystalline swelling involves a gradual expansion of the basal spacing (d) as water activity rises. Various hydration states emerge, including monohydrated (1W, d = 9.6 - 10.7 Å), bihydrated (2W, d = 11.8 - 12.9 Å), and trihydrated (3W, d = 14.5 - 15.8 Å) configurations, alongside a dehydrated state (0W) (Ferrage et al., 2016). On the other hand, different types of hydration models to study the hydrated smectites with the planar arrangement of water molecules in the interlayer have been found in previous calculations (Bérend et al., 1995; Berghout et al., 2010; Emmerich et al., 2015; Fonseca et al., 2017; Emmerich et al., 2018). The results of this study will be compared in order to better understand the relationship between the hydration states defined by the arrangement of water molecules in the layers (1W to 3W) and the hydration states based on the calculated hydration models (1H to 3H) during the hydration of low charge montmorillonite.

Several investigations have employed Quantum Mechanics (QM) with ab initio thermodynamic calculations using density functional theory (DFT) to assess a restricted range of smectite structures. In the previous research, some suggest that QM serves as a proper tool to investigate smaller and restricted systems compared to Molecular Dynamics (MD). For decades, thorough investigations into montmorillonite swelling using molecular modeling have persisted. The differences among structures have been recognized as pivotal factors capable of exerting significant influence on the observed swelling properties. The choice between two calculations allows for the exploration of diverse research subjects and smectite systems. (Ferrage et al., 2005, 2007, 2010; Boek, 2014; Teich-McGoldrick et al., 2015; Tajeddine et al., 2015; Seppälä et al., 2016). DFT calculations in these studies have concentrated on a limited range of smectite structures, with a primary focus on understanding the impact of exchangeable monovalent and divalent cations on the swelling behavior of dioctahedral smectite. Subsequent research has divided into various aspects, including the hydration processes, discrete water behavior at the microscopic level, crystalline swelling, and thermodynamic investigation of different montmorillonite structures. (Chatterjee et al., 2004; Berghout et al., 2010; Fonseca et al., 2017; Ulian et al., 2021)

During the hydration process, van der Waals interactions, which are weak attraction forces between adjacent layers, play a role in the structure, stability, and properties of smectite systems. Some research has indicated that the PBE & PW91 functional tends to overestimate the basal spacing of hydrated smectite without considering van der Waals interactions. Therefore, to improve the prediction accuracy of DFT calculations, Fonseca's DFT calculations employed various exchange-correlation functionals, resulting in divergent simulated basal spacing results. The functional that incorporates van der Waals interactions provided the closest match to experimental basal spacing values. Among the evaluated functionals, DFT-D2 offered the most accurate representation of the basal spacing compared to experimental data (Fonseca et al., 2017). In this study, DFT-D3 is implemented as a more advanced method, extending the DFT-D2 method by incorporating the improved damping functions and three-body dispersion corrections to account for higher-order dispersion interactions. These additional terms improve the accuracy of the dispersion correction for those with more complex molecular arrangements (Grimme et al., 2010, 2011).

Recent simulation studies primarily predict basal spacing changes in smectite models with layer charge values $\xi > 0.2$. However, there remains a definition gap for 2:1 layer silicates with layer charges $\xi = 0 - 0.2$, and no experimental data can verify the existence or properties of low charge montmorillonite. Previous DFT calculations have indicated that montmorillonite with a layer charge $\xi = 0.125$ exhibits swelling properties, offering insight into the definition of montmorillonite (Laird, 2006; Emmerich et al., 2018). The primary focus of this research revolves around understanding the unknown hydration process of trans-vacant and cis-vacant low layer charge montmorillonite with a layer charge $\xi = 0.125$. using a more advanced DFT functional. DFT-D3 method, employed alongside a standard exchange-correlation PBE functional, accounts for long-range dispersion forces that are not, enabling exploration of the interaction between swelling behavior, water content, and relative humidity (rH). The primary objective is to assess stable hydration states, interlayer expansion characterized by changes in basal distance, and water content concerning varying relative humidity conditions for low-charge montmorillonite.

4.2 Methods

4.2.1 Models of Low Charge Montmorillonite

In general montmorillonite structure, with a 2:1 layer structure composed of two tetrahedral sheets with octahedral sheet in between. The montmorillonite models use simplified composition only with one Mg to Al substitution in the octahedral sheet and lattice parameters were set to a_0 = 5.18 Å and b_0 = 8.98 Å , all angles are set to 90°. The change of the supercell volume during the hydration will be related to the change in the c-axis. Therefore, c_0 was allowed to adjust depend on the hydration state of the structures. For all structures, cis-vacant and trans-vacant octahedral sheets with a C2 and C2/m symmetry were chosen respectively. One of the important aspects of the structural and crystal chemical heterogeneity in dioctahedral smectite involves the distribution of octahedral cations between trans- and cis-sites. The tetrahedral sheets are always bonded to octahedral sheets through oxygen atoms. The octahedral sheet has unshared oxygen atoms forming hydroxyl groups. Typically, the octahedral sheet comprises two symmetrically cis-octahedrons divided by hydroxyl groups and one trans-octahedron, which can be described as two cis-sites and one trans-site. One out of three octahedron is not occupied by cations, forming a vacant site. The disposition between vacant sites in the octahedral sheet and hydroxyl groups determines two different structures: when the hydroxyl groups separate the two occupied sites (trans-vacant, tv) or when they do not separate the two occupied sites (cis-vacant, cv) in the octahedral sheets. Also, the cis-vacant structure includes two different variations, which can be described by the different positions occupied by Mg in the octahedral sheet (Mg locates in cis-site: CV1 and locates in trans-site: CV2) (Figure 4.1).

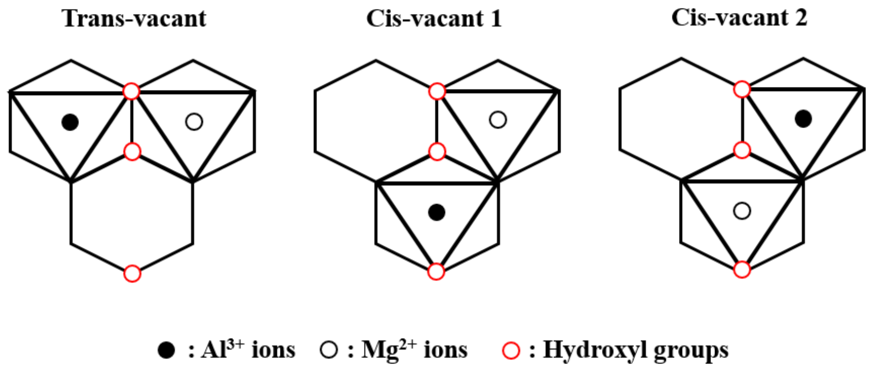

Figure 4.1 Distribution of Al^{3+} and Mg^{2+} ions in octahedral sheets with two cis- and one trans-vacant structural variation. (according to Emmerich & Kahr, 2001).

The low charge montmorillonite model's stoichiometric formulae of supercells (SCs) are represented by $Na_1Si_{32}(Al_{15}Mg_1)O_{80}(OH)_{16} \cdot nH_2O$ (n is the number of water molecules per Na^+ ion, so-call H_2O/Na^+). This model is designed to possess a layer charge of $\xi = 0.125$, which is in the existing definition gap between pyrophyllite ($\xi = 0$) and smectites ($0.2 \leq \xi \leq 0.6$). The calculations were carried out using supercells comprising 4 unit cells (UCs) with substitutions only in the octahedral sheets.

4.2.2 Computational Chemistry and Ab Initio Thermodynamics

In this study, total energy calculations and ground-state structure analyses were conducted utilizing Density Functional Theory (DFT) implemented in the Vienna ab initio simulation program (Kresse & Furthmüller, 1996). The electron-ion interaction was addressed using the projector augmented wave method (Kresse & Joubert, 1999), while the expansion of valence electron wave functions into plane waves extended up to a kinetic energy cutoff of 360 eV. This cutoff ensured the convergence of structural parameters for bulk calculations. Brillouin zone sampling was achieved using k points with a 1 × 1 × 1 mesh Monkhorst - Pack (Monkhorst & Pack, 1976). The generalized gradient approximation of Perdew–Burke–Ernzerhof (PBE) form was applied for the electronic exchange-correlation functional (Perdew et al., 1996). The DFT-D3 method was selected for its reliability in describing structural and energetic aspects, particularly concerning hydrogen-bonded water molecules and van der Waals force interactions. The research of Fonseca et al indicated the DFT-D2 method offered the most accurate representation of the basal spacing in comparison to experimental data (Fonseca et al., 2017). In this research, DFT-D3 method is a more advanced method, also developed by Grimme et al, which extends the DFT-D2 method by including additional terms to account for higher-order dispersion interactions (Grimme et al., 2010, 2011). These additional terms improve the accuracy of the dispersion correction, particularly for larger systems or those with more complex molecular arrangements.

The thickness of montmorillonite layer and the water films in the structure can decide the convergence in calculation of montmorillonite model. A series of calculations with various layer thicknesses was executed for each combination of montmorillonite with different water content. The Birch-Murnaghan equation of state was used to calculate the minimum of thermodynamic, offering insights into the system's stable equilibrium configuration. In this study, we investigate the stable hydration states, interlayer expansion, and water content in low layer charge Na saturated montmorillonite as a function of relative humidity (rH), building upon the groundwork laid by previous research conducted by Emmerich et al., which are described below (Emmerich et al., 2018).

Assessing the stability of a particular structure solely based on the energy is insufficient. To make sure the stability and compare interfaces with distinct stoichiometries energetically, consideration of the chemical potentials $\mu(A_i)$ of the constituents A_i is crucial. The determination of the thermodynamic ground state at the interface involves identifying the minimum of the grand canonical potential, which accounts for the interplay between energy and chemical potentials, offering a comprehensive view of the system's stability concerning different compositions. The interface free energy (F) is approximated using the interface total energy (E) at zero temperature, assuming comparable entropy contributions (S) across various adsorption configurations.

$$\Omega = F - \sum_{i} \mu(A_i) \times n_i$$

$$F = E - TS$$

Notably, differences in vibrational free energy and electronic entropy are often considerably smaller, by several orders of magnitude, compared to the calculated adsorption energies in this context. Therefore, the focus remains primarily on the adsorption energies due to their significantly larger impact, while variations in vibrational free energy and electronic entropy play relatively minor roles in this assessment.

The grand canonical potential affected by the quantity and chemical potential of water molecules, when water molecules intercalated one by one into Na saturated montmorillonite structure. In phase diagrams, two significant values are represented by vertical lines. $\mu\mathrm{H_2O}$ solid indicates the extremely water-rich conditions by the simulation of ice structure. Another vertical line, $\mu\mathrm{H_2O}$ gas, represents the simulation of gas-phase water molecules at zero-temperature. The chemical potential can be directly linked to experimental conditions. The water's chemical potential at interfaces in equilibrium with liquid water is approximated using the value of water ice. Meanwhile, adjustments in the pressure- and temperature-dependent gas-phase water chemical potential are estimated within the framework of a polyatomic ideal gas approximation. Here, various parameters can be present by the symbols: the Boltzmann constant (k_B), pressure (p), temperature (T), corresponds to the de Broglie thermal wavelength of the water molecule (λ) and the molecular mass (m). The rotational and vibrational degrees of freedom to the rotational and vibrational part of the energy are present by the rotational and vibrational partition functions as shown below. For the calculation, the experimental moment of inertia (I) and vibrational frequency (ω) of the water molecule was considered. The geometrical parameter σ = 2 considers the symmetry of the water molecule.

$$\lambda = \sqrt{\frac{2\pi\hbar^2}{mk_BT}}$$

$$Z_{rot} = \frac{(2k_BT)^{3/2}(\pi I_1 I_2 I_3)^{1/2}}{\sigma\hbar^3}$$

$$Z_{vib} = \prod_{a} \left[1 - exp\left(-\frac{\hbar\omega_\alpha}{k_BT}\right)\right]^{-1}$$

$$\Delta\mu\mathrm{H_2O}(p,T) = k_BT\left[\ln\left(\frac{p\lambda^3}{k_BT}\right) - \ln Z_{rot} - \ln Z_{vib}\right]$$

The swelling behavior of the montmorillonite model can be approved by reaching the 1W hydration state under ambient conditions. Therefore, the room humidity (rH) must be taken into account and calculated according to the Magnus formula with the water vapor saturation pressure (P_s) and the partial pressure of H_2O (P_w) (Alduchov & Eskridge, 1996).

$$P_s = 611.2 \times e^{(17.62 \times T/243.12+T)}$$

$$P_w = rH[\%] \times P_s$$

To better understand the relation between the position change of interlayer cation and its interaction with the surface of montmorillonite model during the hydration, it's important to consider the distances of Na^+ ion to the oxygen atoms of the tetrahedral sheet and enthalpy change ($\Delta H_{Surface}$). The cations in the smectite interlayer tends to follow their free form in aqueous solution and to bond according its coordination geometry. These bonds are mainly of electrostatic character similar to the water molecules bind to metal ions (Persson, 2010; Mohammadi Hafshejani et al., 2019). Thus, with the help of the following formula, where Z represents the charge of the Na^+ ion and d_{Na-O} represents the Na–O bond distance (Å) of the Na^+ ion interacting with the surface of the tetrahedral sheet.

$$\Delta H_{Surface} = -10.0948 \frac{Z^2}{d_{Na-O}} \text{ (eV)}$$

4.3 Results and Discussion

4.3.1 Swelling

Prior to calculating the hydrated models, to conduct the calculations to assess the orientation and positioning of Na^+ ion, water molecules, and the smectite surface. The arrangement of water molecules and the energy change of models with 1 to 3 and 6 H_2O/Na^+ were considered. The reasons are to provide more information about the issues regarding the repulsive tendency of CV1 and CV2 models encountered during the early stages of hydration, as well as the possible coordination geometry of interlayer cations and water molecules in the TV model with 6 H_2O/Na^+. The results from 1 H_2O/Na^+ revealed two distinct orientations of water molecules: R1 (water molecule parallel to the smectite surface) and R2 (perpendicular to the smectite surface). The energy associated with these two orientations showed no significant difference. The initial positions of the first 3 water molecules and Na^+ ion in CV1 and CV2 models arrange in a symmetric position and following the simulated results. The energy difference between random and symmetric arrangements of Na^+ ion and water molecules are approximately 1 to 0.5eV. However, this difference is not expected to significantly affect the overall hydration behavior of the montmorillonite model when analyzed further or depicted in various diagrams. Base on this, the other hydrated models first arrange the water molecules symmetrically and calculate the energy of structure (supplementary material).

For the comparison of the structural coordination difference of the TV model with 6 H_2O/Na^+, two possible starting arrangements of water molecules were considered, including a six-coordination (octahedron) and a planar arrangement. Initially, Na^+ ions are coordinated with 4 water molecules, with the remaining 2 water molecules surrounding it through hydrogen bonds. The other two coordination sites interact with the oxygen atoms of the tetrahedral sheet instead of other water molecules through van der Waals interactions. This hydration behavior aligns with the description provided in previous research. (Berghout et al., 2010; Cadars et al., 2012; Fonseca et al., 2016; Seppälä et al., 2016). The energy calculations between the two different structures showed almost no difference, and the calculated structures exhibited similar interlayer coordination between Na^+ ion and water molecules. Therefore, considering only the relationship between the energy difference and the interlayer properties, the arrangement of Na^+ ions and water molecules will not significantly affect the structural stability of the low-charge montmorillonite model as long as it is placed symmetrically (supplementary material).

Smectites exhibit layered structures with weak van der Waals interactions between adjacent layers. The overestimation of basal spacing by standard DFT methods has been discussed in several research studies. However, compared to DFT-D3, PBE and PW91 functionals lack an explicit treatment of dispersion forces, leading to the neglect of these interlayer interactions and their tendency to overestimate the basal spacing of hydrated smectite. Using the TV montmorillonite model with the same structural parameters and layer charge $\xi = 0.125$, a comparison of the calculated results by PW91 and PBE functional indeed reveals the of overestimation of basal spacing around 6.5% for water-free model and 11 - 13% for hydrated model with 3, 6, and 9 H_2O/Na^+ (Figure 4.2). The overestimation percentage of water-free model's basal spacing follows a good agreement value from the previous research (Voora et al., 2011; Fonseca et al., 2017).

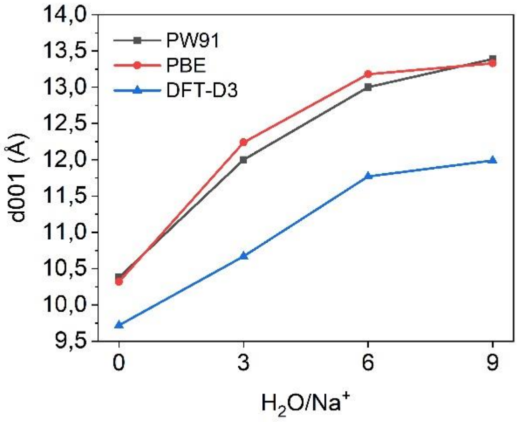

Figure 4.2 Diagram of basal spacing change of trans-vacant montmorillonite model with ξ = 0.125 as a function of H_2O/Na^+ by different DFT functional.

In the nature, the water molecules enter the interlayer of montmorillonites and the hydration of interlayer cations gradually lead to an expansion of the basal spacing. Initially, the potential energy of hydrated montmorillonite models with 1 to 3 H_2O/Na^+ showed unstable tendency. However, after the models contain 4 H_2O/Na^+, the potential energy associated with the addition of each subsequent water molecule stabilized, suggesting a more consistent stepwise hydration behavior and more stable hydrated model with increasing water content. The CV2 model exhibit an unusual strong repulsive tendency when 3 water molecules are entering the structure and the water molecules did not surround the Na^+ ion but stay at the edge of supercell. The same repulsive tendency at early hydration state happened also on the TV and CV1 models. As more water molecules are added, all three models become more stable, resulting in a gradual decrease in potential energy. This trend highlights that an increase in the number of water molecules leads to a more stable decreasing of potential energy, reflecting the heightened stability of the hydrated montmorillonite models (Figure 4.3 Left).

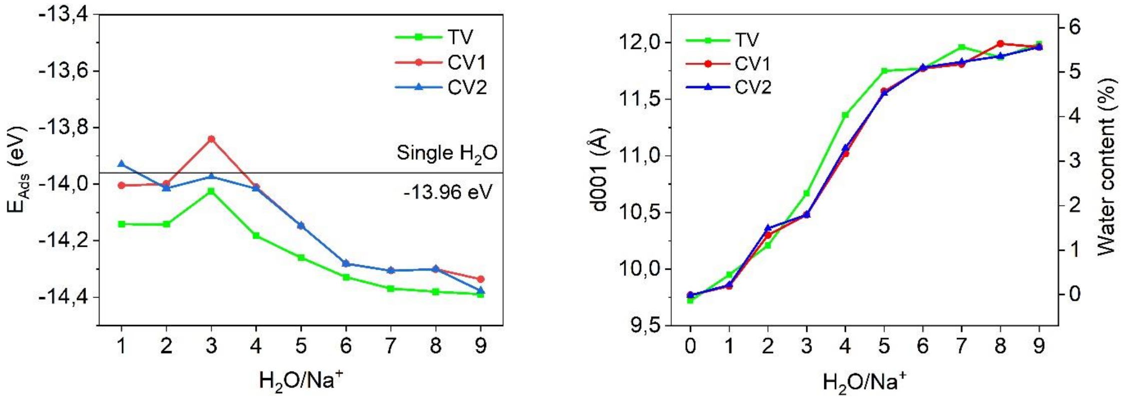

Figure 4.3 Left: diagram of energy change as a function of adding each water molecules; Right: basal spacings and water content of TV, CV1 and CV2 with ξ = 0.125 as a function of H_2O/Na^+.

For the water-free montmorillonite models TV, CV1, and CV2, the basal spacing remains relatively consistent, ranging from approximately 9.72 to 9.77 Å. Experimental data for dry Na saturated montmorillonite consistently determine basal spacing values ranging from 9.5 to 9.8 Å (Cases et al., 1997; Ferrage et al., 2005). Starting from 1 H_2O/Na^+, the interlayer of montmorillonite models gradually opens. As the number of H_2O/Na^+ increases to 9, the basal space expands to around 12 Å, approaching the monohydrated state (1W, d = 11.8 - 12.9 Å). The swelling curve of all three models exhibits a similar tendency. Changes in basal spacing in hydration states across different water contents and the swelling behavior can be observed in the simulation results (Figure 4.3 Right). In addition, as the number of H_2O/Na^+ increases, the position of the interlayer Na^+ ions continues to change, starting from close to the surface and moving to the middle of the interlayer space. This can be explained by the increase in the hydration energy of Na^+ ion during the hydration process, while the hydration shielding around the Na^+ ions results in a reduction in the attraction between the ions and the layer surface (Laird, 2006). The behavior can also be observed through the previous repulsive tendency when adding 1 to 3 water molecules. Na^+ ion of CV1 and CV2 models start to move toward the middle of the interlayer at a higher water content compared to the TV model. This suggests that at the beginning of hydration, the main interaction in the interlayer is the attraction of Na^+ ion to the surface for all models. As more water molecules enter the interlayer and start to hydrate with the Na^+ ion, then the position of Na^+ ion reach an equilibrium state. In addition, the calculation of the enthalpy change ($-\Delta H_{Surface}$) between the bonding of Na^+ ion and the nearest oxygen atom on the surface of the tetrahedral sheet was compared, showing the weaken of the interaction between Na^+ ion and the surface during the hydration (Figure 4.4).

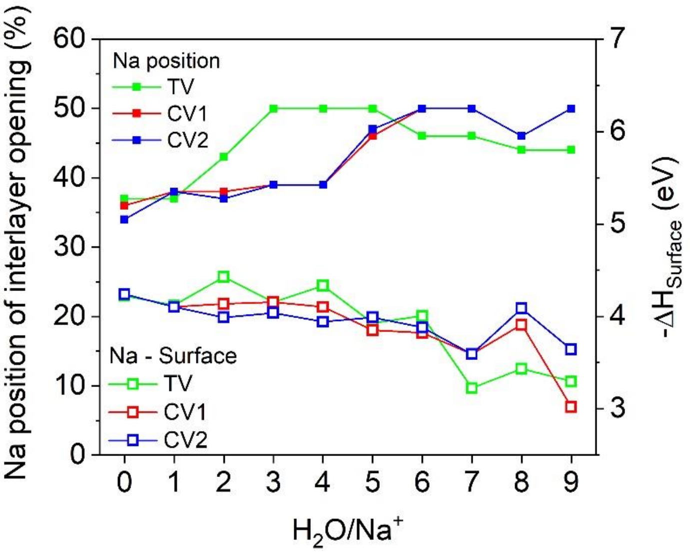

Figure 4.4 Diagram of interlayer Na^+ ion position changes and the enthalpy change between the Na^+ ion and the surface as a function of H_2O/Na^+.

Throughout hydration, water molecules initially arrange randomLy before surrounding the Na^+ ion and aligning themselves in a single plane parallel to the surface of all montmorillonite models. The structural change during the hydration can be observed, the changes in the octahedral sheet occur only in the tilt of the hydroxyl groups between the two occupation cations. From the above view of the montmorillonite model, the hexagon arrangement of O atoms of silicas on the surface of tetrahedral sheet can be seen. Every six O atoms and six Si atoms constitute a cyclic structure, with the O atoms forming a hexagonal ring on the surface. This structure binds with the Na^+ ion with net negative charge on the surface. Several studies have noted this hexagonal ring structure, wherein three of the six O atoms shift outward while the other three shifts inward (Shi et al., 2013, 2015; Peng et al., 2016). Additionally, the Na^+ ion shifts within the hexagonal ring from one side to the middle during hydration, resulting in a more stable structure and equilibrium state for the hydration of the Na^+ ion and attraction to the surface. For CV1 and CV2 models, different phenomena were observed, the equilibrium position of the Na^+ ion still remains located in the middle of the interlayer, but it tends to be closer to the Mg substitution position in the octahedral sheet compared to the TV model. (Relevant figure and parameters are in the supplementary material).

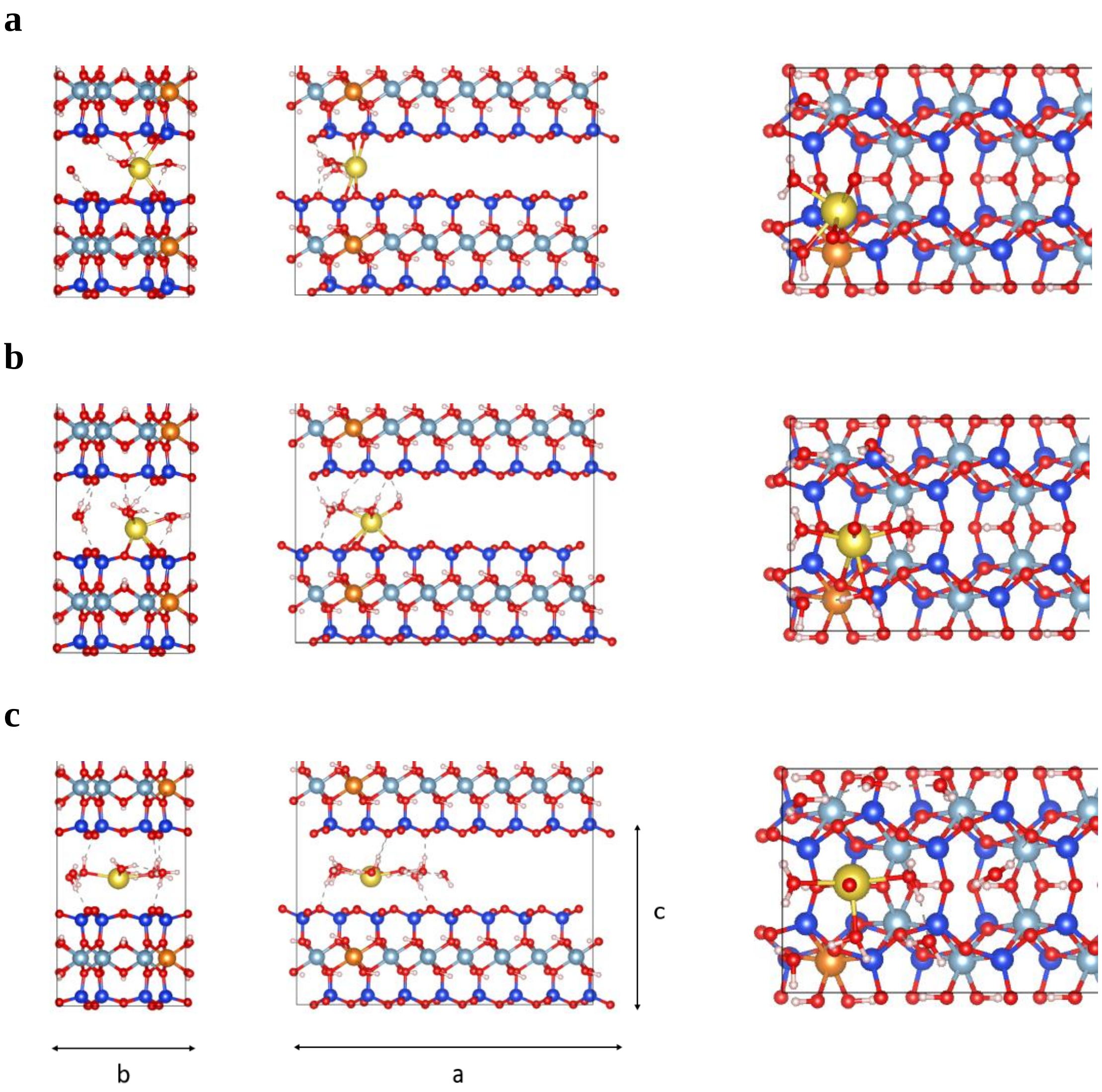

Figure 4.5 Trans-vacant hydrated montmorillonite supercell, from a to c represent 3, 6 and 9 H_2O/Na^+ (simulated CV1 and CV2 models are attached in supplementary material). Blue spheres as Si. Light blue spheres as Al. Orange sphere as Mg. Green sphere as Na. White spheres as H. Red spheres as O.

4.3.2 Stable Hydration States

Considering the montmorillonite models during hydration steps, the grand canonical potential primarily depends on the number of water molecules and, consequently, the chemical potential of water. This theoretical assumption provides a microscopic explanation for hydration states based on structural disparities and the low layer charge of montmorillonites. To visualize the simulation results, phase diagrams as a function of water chemical potential can be transformed into pressure-temperature phase diagrams (Figure 4.6).

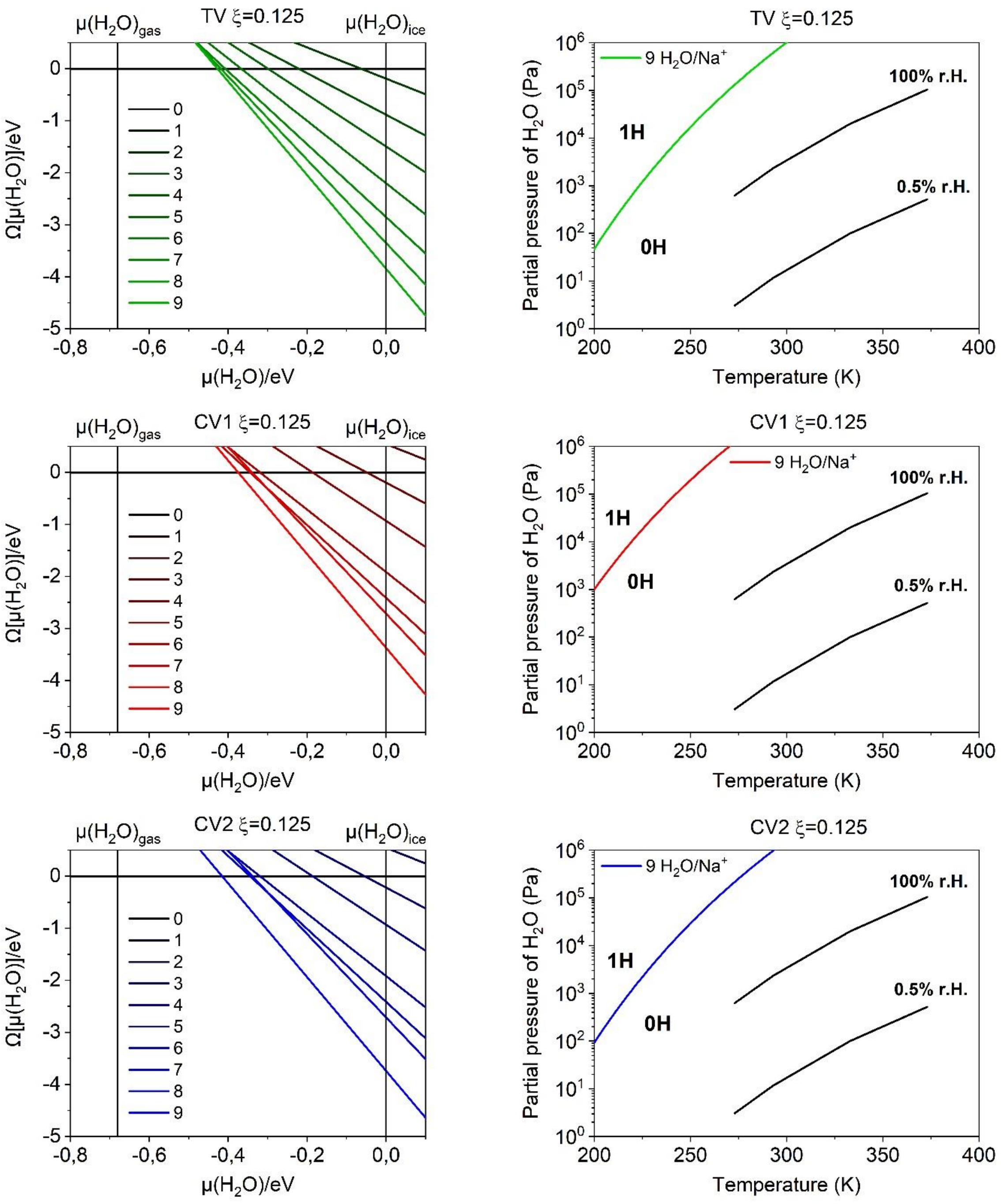

Figure 4.6 Left: Calculated phase diagram as a function of chemical potential of water. The number of water molecules per SC is indicated; Right: p, T-phase diagram with rH curves for montmorillonites.

Starting with the water-free montmorillonite models, the p, T-phase diagrams for both trans-vacant and cis-vacant montmorillonite models incorporated all 9 H_2O/Na^+ (equivalent to a water content of 5.3%) indicated that the hydration state remained in the transition state of 0H to 1H state at ambient conditions up to an rH of 100%. These results can also be compared by observing the basal spacing change of hydrated montmorillonite models from simulation results. Regarding the tendency of the phase diagram as a function of water chemical potential, as the number of water molecules continues to increase beyond 9 H_2O/Na^+, there is a high possibility for the potential energy of the 1H hydration boundary to decrease and alter the p, T-phase diagram. Therefore, the following results indicate that for the TV montmorillonite model with 12 and 21 H_2O/Na^+ which the water content are 7.4 and 13%, the boundary between the 0H and 1H hydration states in p, T-phase diagram begins to shift to the ambient condition. The 1H hydration state reached when the TV model with 21 H_2O/Na^+ at 273-293 K and rH of 50-100% (Figure 4.7). In summary, when using the DFT-D3 functional to simulate the swelling behavior of the low charge montmorillonite model with layer charge $\xi = 0.125$, it is possible to reach the 1H hydration state with a higher water content and to reveal its swellability under ambient conditions. This can be the key point of future planning to broaden the understanding of the hydration behavior of low charge montmorillonite.

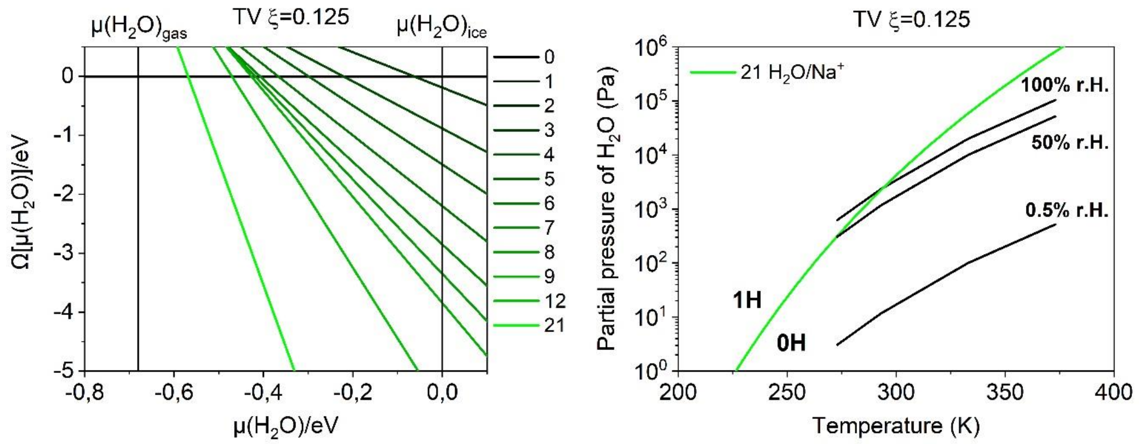

Figure 4.7 Left: Calculated phase diagram as a function of chemical potential of water; Right: p, T-phase diagram with rH curves for montmorillonites with 21 H_2O/Na^+.

Previous simulation results using the PW91 functional have shown that montmorillonite models with layer charge $\xi = 0.125$ are swellable (Emmerich et al., 2018). However, significant differences between two research in basal spacing and swelling behavior prediction were observed upon the incorporation of van der Waals interactions. The possibility of including a higher number of H_2O/Na^+ for the montmorillonite model can be seen on the p, T-phase diagram. It is reasonable to consider that the development of DFT functionals may yield different results, potentially influencing the prediction of potential energy and basal spacing during the hydration of montmorillonite. When considering the equivalent area and water content of the montmorillonite model in this study, the possibility of reaching the 1H or even 2H hydration state remains high. However, due to the high computational demand for the calculation and the lack of natural or synthetic samples, the results of this research could not achieve the aim of fully predicting the swelling behavior of low charge montmorillonite.

4.4 Summary and Future Outlook

The simulation of the hydration behavior and swellability of trans-vacant and two cis-vacant low charge montmorillonite models using DFT-D3 functional, is studied in this research. However, due to the lack of natural or synthetic low charge montmorillonite samples, there is no sufficient experimental data to validate or refine the simulated results. Nevertheless, based on numerous studies employing DFT calculations in recent years, this method still possesses the capability to offer supportive information for predicting the properties of smectite models.

The basal spacing of water-free trans-vacant and two cis-vacant montmorillonite models are approximately 9.7 Å, which aligns well with experimental values ranging between 9.5 - 9.8 Å. All three hydrated montmorillonite models exhibit similar swelling curves, with the basal spacing expanding to about 12 Å as the number of H_2O/Na^+ reaches 9. During hydration, after the first 4 coordination sites of the Na^+ ion all bond to water molecules, the other 2 coordination sites tend to interact with the oxygen atom of the tetrahedral sheet instead of bonding to water molecules. Therefore, the subsequent water molecules can only surround them in a planar structure parallel to the tetrahedral sheet. The position of the interlayer Na^+ ion starts to move toward the middle of the interlayer space as the number of H_2O/Na^+ increases, while the weakening of the interaction between Na^+ ion and the surface can be observed through the calculation of enthalpy change.

Additionally, the discussion addresses the tendency of standard DFT methods, particularly PBE and PW91 functionals, to overestimate basal spacing in various research studies. This discrepancy arises from the absence of explicit treatment of dispersion forces, unlike DFT-D3. Smectite minerals, characterized by layered structures with weak van der Waals interactions, are particularly susceptible to this overestimation. Using the trans-vacant montmorillonite model with same structural parameters and layer charge, the study highlights the observed overestimation of basal spacing in montmorillonite models with 0, 3, 6, and 9 H_2O/Na^+ when employing PW91 and PBE functionals.

P, T-phase diagrams revealed that all models with 1 to 9 H_2O/Na^+ the hydration state remained at 0H to 1H up to an rH of 100%. Based on the tendency shown on the p, T-phase diagram and as the water content keeps increasing, the TV montmorillonite model with 21 H_2O/Na^+, where the water content is 13%, reaches the 1H hydration state at 273-293 K and rH of 50-100%. Therefore, there is a potential possibility of low charge montmorillonite showing swelling behavior under ambient conditions. Previous simulation results using the PW91 functional indicated that montmorillonite models with a layer charge of 0.125 are swellable. However, the differences in basal spacing prediction were observed when van der Waals interactions were incorporated. The possibility of including a higher number of H_2O/Na^+ for the montmorillonite model can be seen on the p, T-phase diagram. However, due to several experimental limits, this research could not fully predict the swelling behavior of low charge montmorillonite.

In optimizing future simulations of the hydration state of low charge montmorillonite model, it is crucial to consider more experimental parameters such as increasing the number of

H_2O/Na^+ by the equivalent area (a_0b_0) of the low charge montmorillonite model, the optimization of initial configuration or of water molecules in the interlayer, and considering the forces and interactions at the interface of Na saturated montmorillonite and water molecules. Last but not least, Using Molecular Dynamics (MD) calculations to compare with DFT calculations of smectite hydration provides complementary insights into the system's behavior. The following highlight key points for improving the future experiment:

1. The structural parameters of the low charge montmorillonite model such as a_0, b_0, substitution position and cation location should be optimized. Initially, a water-free model with an initial basal spacing is calculated to determine the most stable structures. The number of water molecules and basal spacing are gradually increased once stable structures are obtained. The structures are then optimized again before adding more water molecules or increasing the basal spacing.

2. Visualizing the energy difference of each possible structure helps to identify the best position or arrangement of the water molecules and Na^+ ion in the interlayer. This involves an energy mapping of the energy distribution at the interlayer surface, which aids in determining the most stable positions for the hydration path of the water molecules during hydration.

3. Based on previous research by Emmerich et al., the forces and interactions at the interface of Na saturated montmorillonite and water molecules can be separated into various factors, including the hydration energy of Na^+ ions, interactions between water molecules, and interactions between water molecules and the surface. These factors can fully interpret the energy of the simulated structure (Emmerich et al., 2015).

4. MD calculations can be a supportive tool for simulating low charge montmorillonite models, allowing for simulations under diverse conditions to mimic montmorillonite behavior across different environments and compare it with DFT calculations. A two-step approach is commonly adopted: first, the DFT method optimizes the unit cell size parameter to attain the most stable structure; subsequently, MD calculation is employed to simulate hydration of the optimized structure, thereby capturing its structural behavior in ambient conditions.

References

Alduchov, O. A., & Eskridge, R. E. (1996). Improved Magnus form approximation of saturation vapor pressure. *Journal of Applied Meteorology and Climatology*, *35*(4), 601–609.

Bérend, I., Cases, J.-M., François, M., Uriot, J.-P., Michot, L., Masion, A., & Thomas, F. (1995). Mechanism of adsorption and desorption of water vapor by homoionic montmorillonites: 2. The Li+, Na+, K+, Rb+ and Cs+-exchanged forms. *Clays and Clay Minerals*, *43*(3), 324–336.

Berghout, A., Tunega, D., & Zaoui, A. (2010). Density functional theory (DFT) study of the hydration steps of Na+/Mg2+/Ca2+/Sr2+/Ba2+-exchanged montmorillonites. *Clays and Clay Minerals*, *58*(2), 174–187.

Boek, E. S. (2014). Molecular dynamics simulations of interlayer structure and mobility in hydrated Li-, Na-and K-montmorillonite clays. *Molecular Physics*, *112*(9–10), 1472–1483.

Cases, J. M., Bérend, I., François, M., Uriot, J. P., Michot, L. J., & Thomas, F. (1997). Mechanism of adsorption and desorption of water vapor by homoionic montmorillonite: 3. The Mg2+, Ca2+, Sr2+ and Ba2+ exchanged forms. *Clays and Clay Minerals*, *45*(1), 8–22.

Chatterjee, A., Ebina, T., Onodera, Y., & Mizukami, F. (2004). Effect of exchangeable cation on the swelling property of 2: 1 dioctahedral smectite—A periodic first principle study. *The Journal of Chemical Physics*, *120*(7), 3414–3424.

Delavernhe, L., Steudel, A., Darbha, G. K., Schäfer, T., Schuhmann, R., Wöll, C., Geckeis, H., & Emmerich, K. (2015). Influence of mineralogical and morphological properties on the cation exchange behavior of dioctahedral smectites. *Colloids and Surfaces A: Physicochemical and Engineering Aspects*, *481*, 591–599.

Emmerich, K., Wolters, F., Kahr, G., & Lagaly, G. (2009). Clay profiling: The classification of montmorillonites. *Clays and Clay Minerals*, *57*(1), 104–114.

Emmerich, K., Koeniger, F., Kaden, H., & Thissen, P. (2015). Microscopic structure and properties of discrete water layer in Na-exchanged montmorillonite. *Journal of Colloid and Interface Science*, *448*, 24–31..

Emmerich, K., Giraudo, N., Schuhmann, R., Schnetzer, F., Kaden, H., & Thissen, P. (2018). On the prediction of water contents in Na-saturated dioctahedral smectites. *The Journal of Physical Chemistry C*, *122*(13), 7484–7493.

Ferrage, E., Lanson, B., Sakharov, B. A., & Drits, V. A. (2005). Investigation of smectite hydration properties by modeling experimental X-ray diffraction patterns: Part I. Montmorillonite hydration properties. *AMERICAN MINERALOGIST*, *90*(8–9), 1358–1374.

Ferrage, E., Lanson, B., Sakharov, B. A., Geoffroy, N., Jacquot, E., & Drits, V. A. (2007). Investigation of dioctahedral smectite hydration properties by modeling of X-ray diffraction profiles: Influence of layer charge and charge location. *American Mineralogist*, *92*(10), 1731–1743.

Ferrage, E., Lanson, B., Michot, L. J., & Robert, J.-L. (2010). Hydration properties and interlayer organization of water and ions in synthetic Na-smectite with tetrahedral layer charge. Part 1. Results from X-ray diffraction profile modeling. *The Journal of Physical Chemistry C*, *114*(10), 4515–4526.

Ferrage, E. (2016). Investigation of the interlayer organization of water and ions in smectite from the combined use of diffraction experiments and molecular simulations. A review of methodology, applications, and perspectives. *Clays and Clay Minerals*, *64*(4), 348–373.

Fonseca, C. G., Vaiss, V. S., Wypych, F., Diniz, R., & Leitao, A. A. (2017). Structural and thermodynamic investigation of the hydration-dehydration process of Na+-Montmorillonite using DFT calculations. *Applied Clay Science*, *143*, 212–219.

Gaharwar, A. K., Cross, L. M., Peak, C. W., Gold, K., Carrow, J. K., Brokesh, A., & Singh, K. A. (2019). 2D nanoclay for biomedical applications: Regenerative medicine, therapeutic delivery, and additive manufacturing. *Advanced Materials*, *31*(23), 1900332.

Grimme, S., Antony, J., Ehrlich, S., & Krieg, H. (2010). A consistent and accurate ab initio parametrization of density functional dispersion correction (DFT-D) for the 94 elements H-Pu. *The Journal of Chemical Physics*, *132*(15).

Grimme, S., Ehrlich, S., & Goerigk, L. (2011). Effect of the damping function in dispersion corrected density functional theory. *Journal of Computational Chemistry*, *32*(7), 1456–1465.

Guggenheim, S., Adams, J. M., Bain, D. C., Bergaya, F., Brigatti, M. F., Drits, V. A., Formoso, M. L., Galán, E., Kogure, T., & Stanjek, H. (2006). Summary of recommendations of nomenclature committees relevant to clay mineralogy: Report of the Association Internationale pour l'Etude des Argiles (AIPEA) Nomenclature Committee for 2006. *Clays and Clay Minerals*, *54*(6), 761–772.

Kresse, G., & Furthmüller, J. (1996). Efficiency of ab-initio total energy calculations for metals and semiconductors using a plane-wave basis set. *Computational Materials Science*, *6*(1), 15–50.

Kresse, G., & Joubert, D. (1999). From ultrasoft pseudopotentials to the projector augmented-wave method. *Physical Review b*, *59*(3), 1758.

Laird, D. A. (2006). Influence of layer charge on swelling of smectites. *Applied Clay Science*, *34*(1–4), 74–87.

Mering, J., & Oberlin, A. (1971). The Smectites. In J. A. Gard (Ed.), *The Electron-Optical Investigation of Clays* (Vol. 3, p. 0). Mineralogical Society of Great Britain and Ireland.

Mohammadi Hafshejani, T., Hohmann, S., Nefedov, A., Schwotzer, M., Brenner-Weiss, G., Izadifar, M., & Thissen, P. (2019). Formation and Stability of Nontoxic Perovskite Precursor. *Langmuir*, *35*(49), 16217–16225.

Monkhorst, H. J., & Pack, J. D. (1976). Special points for Brillouin-zone integrations. *Physical Review B*, *13*(12), 5188.

Perdew, J. P., Chevary, J. A., Vosko, S. H., Jackson, K. A., Pederson, M. R., Singh, D. J., & Fiolhais, C. (1992). Atoms, molecules, solids, and surfaces: Applications of the generalized gradient approximation for exchange and correlation. *Physical Review B*, *46*(11), 6671.

Perdew, J. P., Burke, K., & Ernzerhof, M. (1996). Generalized gradient approximation made simple. *Physical Review Letters*, *77*(18), 3865.

Persson, I. (2010). Hydrated metal ions in aqueous solution: How regular are their structures? *Pure and Applied Chemistry*, *82*(10), 1901–1917.

Peng, C., Min, F., Liu, L., & Chen, J. (2016). A periodic DFT study of adsorption of water on sodium-montmorillonite (001) basal and (010) edge surface. *Applied Surface Science*, *387*, 308–316.

Sellin, P., & Leupin, O. X. (2013). The use of clay as an engineered barrier in radioactive-waste management–a review. *Clays and Clay Minerals*, *61*(6), 477–498.

Seppälä, A., Puhakka, E., & Olin, M. (2016). Effect of layer charge on the crystalline swelling of Na+, K+ and Ca2+ montmorillonites: DFT and molecular dynamics studies. *Clay Minerals*, *51*(2), 197–211.

Shi, J., Liu, H., Meng, Y., Lou, Z., Zeng, Q., & Yang, M. (2013). First-principles study of ammonium ions and their hydration in montmorillonites. *Journal of Molecular Modeling*, *19*, 1875–1881.

Tajeddine, L., Gailhanou, H., Blanc, P., Lassin, A., Gaboreau, S., & Vieillard, P. (2015). Hydration–dehydration behavior and thermodynamics of MX-80 montmorillonite studied using thermal analysis. *Thermochimica Acta*, *604*, 83–93.

Teich-McGoldrick, S. L., Greathouse, J. A., Jove-Colon, C. F., & Cygan, R. T. (2015). Swelling properties of montmorillonite and beidellite clay minerals from molecular simulation: Comparison of temperature, interlayer cation, and charge location effects. *The Journal of Physical Chemistry C*, *119*(36), 20880–20891.

Turunen, M., Brotons-Gisbert, M., Dai, Y., Wang, Y., Scerri, E., Bonato, C., Jöns, K. D., Sun, Z., & Gerardot, B. D. (2022). Quantum photonics with layered 2D materials. *Nature Reviews Physics*, *4*(4), 219–236.

Ulian, G., Moro, D., & Valdrè, G. (2021). Dft simulation of the water molecule interaction with the (00l) surface of montmorillonite. *Minerals*, *11*(5), 501.

Voora, V. K., Al-Saidi, W. A., & Jordan, K. D. (2011). Density functional theory study of pyrophyllite and M-montmorillonites (M= Li, Na, K, Mg, and Ca): Role of dispersion interactions. *The Journal of Physical Chemistry A*, *115*(34), 9695–9703.

Kuligiewicz, A., & Derkowski, A. (2017). Tightly bound water in smectites. *American Mineralogist*, *102*(5), 1073–1090.

Wolters, F., Lagaly, G., Kahr, G., Nueeshch, R., & Emmerich, K. (2009). A comprehensive characterization of dioctahedral smectites. *Clays and Clay Minerals*, *57*(1), 115–133.

Acknowledgements

None of this work would have been possible without the abundant support and assistance I received. Looking back on my PhD journey, countless challenges repeatedly reminded me to remain cautious, humble, and diligent on the academic path. I am grateful to have completed this journey and believe it has fostered significant personal growth.

First, I am deeply thankful to my supervisor, Prof. Dr. Katja Emmerich. From teaching me scientific research methods to helping me in any aspect of life where I needed support, you have always offered your full guidance without hesitation. Even in moments of self-doubt, you reassured me that no effort is ever wasted. You have been my most significant mentor throughout this doctoral journey and an invaluable guide during this chapter of my life.

I am also thankful to my co-supervisor PD Dr. Peter Thissen, whose expertise in computational methods and simulations provided invaluable guidance. Your insights and thoughtful feedback, especially during the revision of my dissertation, have been indispensable.

To my colleague Dr. Nadja Werling, thank you for your kindness and patience in answering my questions and helping me overcome all the challenges in the early stages of my lab work. Your support allowed me to adapt quickly to the environment at KIT and to feel not alone within the research group.

Special thanks to my colleague Dr. Eleanor Bakker for your professional guidance and insightful advice during my experiments and analyses. Your hard-working attitude always inspired me and helped us establish a solid experimental framework and a well-organized lab environment. I am equally grateful for your warm invitations, which enriched my daily life and made my experience here all the more memorable.

To all my colleagues at the Competence Center for Material Moisture (CMM), Dr.-Ing. Rainer Schuhmann, Dr. Ali Assad, Irwan Nugraha, Silke Schönauer, Anke Ehbrecht, Franz Königer, and Rosemarie Bender. I owe a heartfelt thanks for all the support, companionship and encouragement you have provided at every stage of this journey. Each of you has contributed to my success, and without you, completing this task would not have been possible. I am truly honored to be part of CMM team.

I am also deeply grateful to my family, my girlfriend, and my friends from the Asian NewBees basketball team. Your companionship and love were my refuge and motivation through every trial. No matter the difficulties I faced, knowing that you will always be there for me gave me the strength to continue. I cherish and love you all deeply.

Finally, I dedicate all my accomplishment during this journey to my father. Thank you for the kindness and strength you have imparted to me. You are the most honest, compassionate, and gentle person I have ever known. I will strive to carry forward your values and, in time, hope to become a person as admirable as you.

Supplementary Material

Table S1. The energy, bond length and angle of Na^+ + H_2O hydrated models.

Name	**O-Na (Å)**	**O-H (Å)**	**O-H-O (°)**	**H_2O-Na-H_2O (°)**
Ideal H_2O	-	0.95	104.52	-
Simulated H_2O	-	0.98	103.65	-
Na^+ + 1 H_2O	2.27	0.98	105.16	-
Na^+ + 2 H_2O	2.25	0.98	104.30	180
Na^+ + 3 H_2O	2.27	0.98	104.38	112, 136

Table S2. The energy, bond length and angle of CV1 and CV2 hydrated model with 1-3 H_2O/Na^+ in different arrangement of water molecules and Na^+ ion.

CV1 Na-MMT + 1-3 H_2O/Na^+						
Structure Name	**E (eV)**	**Na-O (Å)**			**O-H (Å)**	**H-O-H (°)**
CV1-1H_2O-MMT	-1196.836	3.86			0.99	107.3
CV1-1H_2O-MMT-P1	-1196.901	3.46			0.99	107.5
CV1-1H_2O-MMT-P2	-1197.356	3.91			0.98	104.7
CV1-1H_2O-MMT-P3	-1197.500	2.23			0.98	103.7
CV1-2H_2O-MMT	-1211.206	4.70	6.15		0.98	105.9
CV1-2H_2O-MMT-P1	-1210.420	3.37	3.39		0.99	108.3
CV1-2H_2O-MMT-P2	-1211.494	2.15	3.76		0.98	104.7
CV1-3H_2O-MMT	-1224.909	4.47	5.02	5.93	1.07	105.5
CV1-3H_2O-MMT-P1	-1224.321	2.17	2.67	3.26	0.98	106.2
CV1-3H_2O-MMT-P2	-1223.823	2.26	2.26	3.21	0.99	103.4
CV1-3H_2O-MMT-P3	-1224.608	4.47	4.99	6.63	0.99	104.2
CV2 Na-MMT + 1-3 H_2O/Na^+						
Structure Name	**E (eV)**	**Na-O (Å)**			**O-H (Å)**	**H-O-H (°)**
CV2-1H_2O-MMT	-1197.072	3.88			0.99	107.1
CV2-1H_2O-MMT-P1	-1196.817	2.98			1.01	107.7
CV2-1H_2O-MMT-P2	-1197.380	3.81			0.98	104.6
CV2-1H_2O-MMT-P3	-1197.425	2.17			0.98	104.4
CV2-2H_2O-MMT	-1210.538	4.09	4.62		0.99	104.5
CV2-2H_2O-MMT-P1	-1210.301	3.00	3.87		1.00	108.2
CV2-2H_2O-MMT-P2	-1211.525	2.16	3.63		0.98	105.7
CV2-3H_2O-MMT	-1224.313	3.69	3.06	5.50	1.00	105.6
CV2-3H_2O-MMT-P1	-1225.129	2.52	2.17	3.60	0.98	104.5
CV2-3H_2O-MMT-P2	-1224.830	2.25	2.19	3.94	0.99	104.5
CV2-3H_2O-MMT-P3	-1225.417	2.17	3.63	5.13	0.98	104.3

Table S3. The energy TV hydrated model with 6 H_2O/Na^+ in different coordination of water molecules and Na^+ ion.

TV Na-MMT + 6 H_2O/Na^+		
Structure Name	**H_2O/Na+ Arrangement**	**E (eV)**
TV-6H_2O-MMT	Planar	-1268,882
TV-6H_2O-MMT-W6C	Hexahedron	-1268.912

TV-6H_2O-MMT

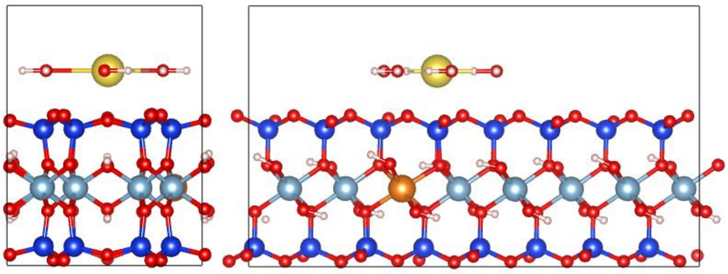

TV-6H_2O-MMT (Calculated structure)

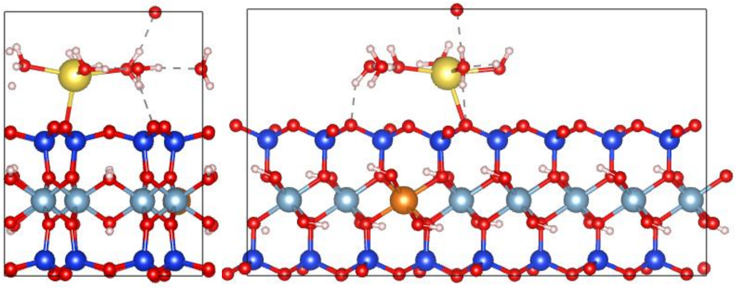

TV-6H_2O-MMT-W6C

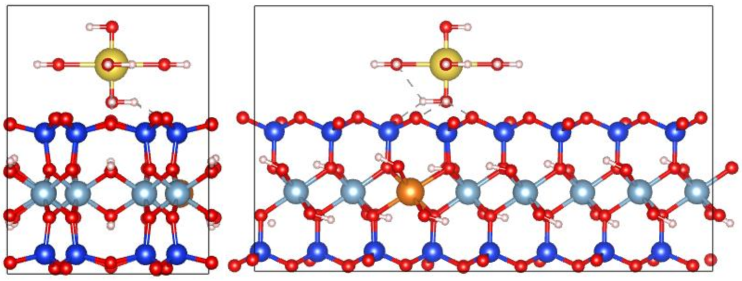

TV-6H_2O-MMT-W6C (Calculated structure)

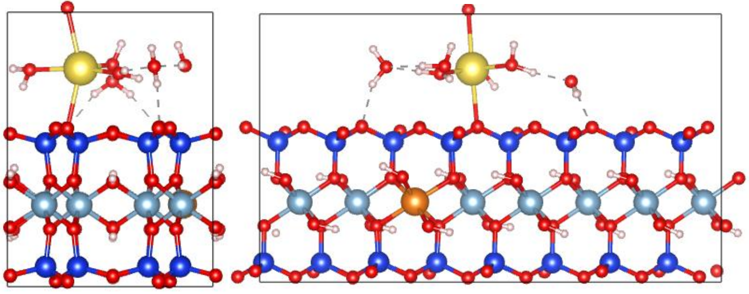

Figure S1. Trans-vacant hydrated montmorillonite supercell with 6 H_2O/Na^+. Blue spheres as Si. Light blue spheres as Al. Orange sphere as Mg. Green sphere as Na. White spheres as H. Red spheres as O.

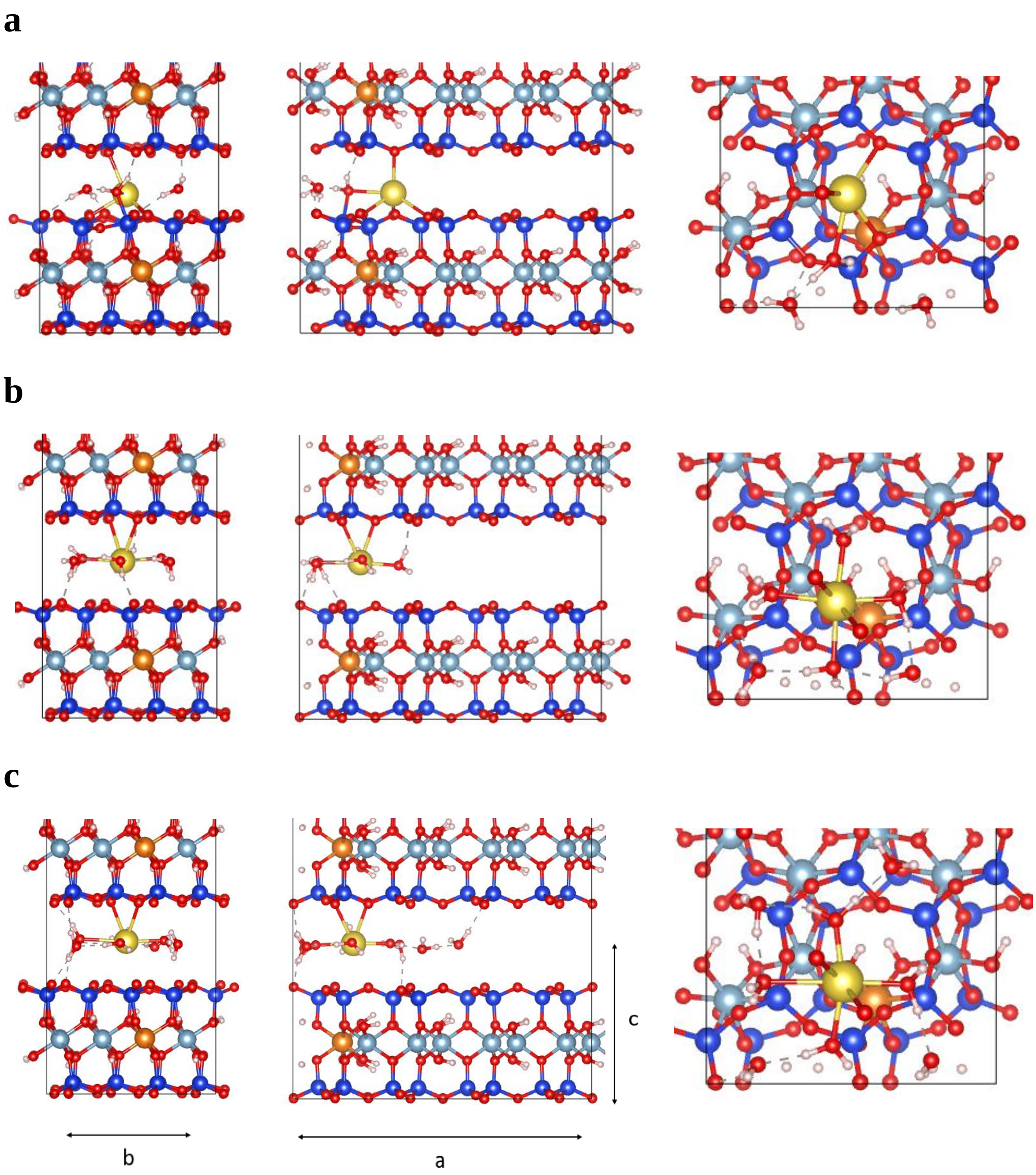

Figure S2. Cis-vacant 1 hydrated montmorillonite supercell, from a to c represent 3, 6 and 9 H_2O/Na^+. Blue spheres as Si. Light blue spheres as Al. Orange sphere as Mg. Green sphere as Na. White spheres as H. Red spheres as O.

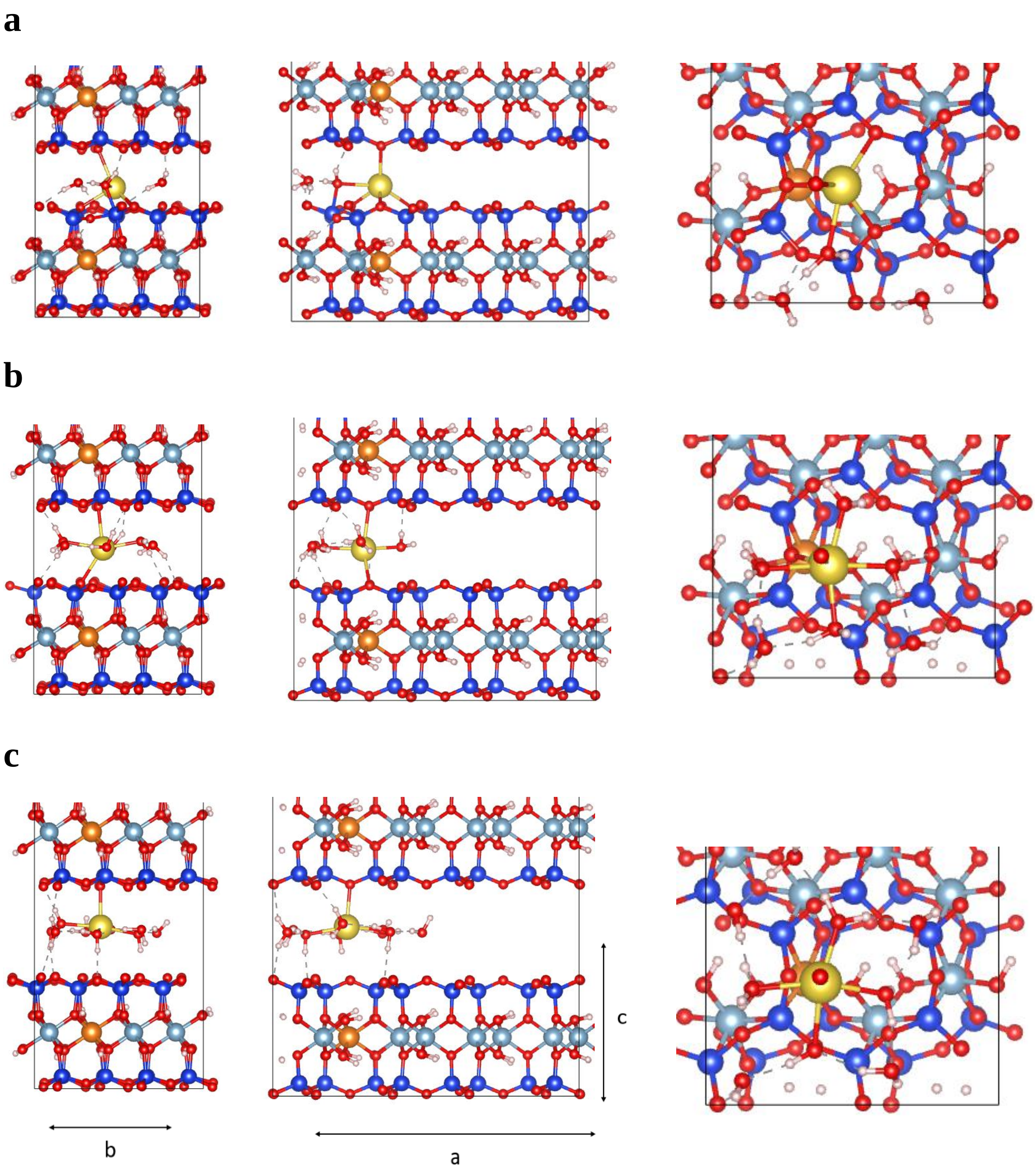

Figure S3. Cis-vacant 2 hydrated montmorillonite supercell, from a to c represent 3, 6 and 9 H_2O/Na^+. Blue spheres as Si. Light blue spheres as Al. Orange sphere as Mg. Green sphere as Na. White spheres as H. Red spheres as O.